DEFORMATION EFFECTS ON THE DEVELOPMENT OF GRAIN BOUNDARY CHROMIUM DEPLETION (SENSITIZATION) IN TYPE 316 AUSTENITIC STAINLESS STEELS

Ashok H. Advani
B.Tech., Indian Institute of Technology (Bombay), 1985

A dissertation submitted to the faculty of the

Oregon Graduate Institute
of
Science and Technology

in partial fulfillment of the
requirements for the degree
Doctor of Philosophy
in
Materials Science and Engineering

March, 1990

The dissertation **Deformation Effects on the Development of Grain Boundary Chromium Depletion (Sensitization) in Type 316 Austenitic Stainless Steels** by Ashok H. Advani has been examined and approved by the following Examination Committee:

David G. Atteridge, Thesis Advisor
Associate Professor,
Oregon Graduate Institute, Oregon

Stephen M. Bruemmer
Staff Scientist,
Battelle Northwest Laboratories, Washington

Lawrence E. Murr
Professor and Department Chairman,
University of Texas at El Paso, Texas

William E. Wood
Professor and Department Chairman,
Oregon Graduate Institute, Oregon

Jack H. Devletian
Professor,
Oregon Graduate Institute, Oregon

This thesis is dedicated to my parents and wife.

ACKNOWLEDGEMENTS

First and foremost, I would like to express my deep appreciation to Dr. David Atteridge for his encouragement, enthusiasm and support throughout the development of my work. Special thanks are also due to Drs. Stephen Bruemmer and Lawrence Murr for their guidance at various stages of the research, and Drs. William Wood and Jack Devletian for their time and effort in evaluating the thesis. I would also like to express my gratitude to the "members of the DOE research group" John Simmons, Dr. Ward Stevens, C.V. Ramachandran, Larry Venne and Cesar Cedeno, friends Dr. U. Sudarsan, V. Dixit, R. Devanathan, R. Parthasarathy, Sin-Jang Chen, Dr. Daniel Danks, Tyrus Monson, staff Bob Turpin, Jessie Atteridge, Nancy Biskey, Ken Burns, Dale Christensen and other faculty for their thoughts and advice. Last, and certainly not the least, I would like to thank my wife Monu for her patience, encouragement and support during the difficult times of writing this manuscript.

Funding for this research was provided by the U.S. Department of Energy under contract no. DE-37963.

TABLE OF CONTENTS

ACKNOWLEDGEMENTS iv

FIGURE CAPTIONS x

LIST OF TABLES xix

ABSTRACT xx

CHAPTER 1.INTRODUCTION 1

OVERVIEW 2

RESEARCH OBJECTIVE 4

BACKGROUND 6

GRAIN BOUNDARY CHROMIUM DEPLETION IN STAINLESS STEELS 7

PLASTIC DEFORMATION OF AUSTENITIC STAINLESS STEELS 11

Macroscopic Deformation of Austenitic SS 11

Microstructural Effects of Strain . . . 13

DEFORMATION EFFECTS ON ISOTHERMAL GRAIN BOUNDARY CHROMIUM DEPLETION IN STAINLESS STEELS 21

Concepts 21

Literature Observations 26

MODELING DEFORMATION EFFECTS ON GRAIN BOUNDARY CHROMIUM DEPLETION 32

Grain Boundary Chromium Depletion Modeling 32

Deformation Effects Modeling 36

Deformation Effects on Sensitization Modeling 43

CHAPTER 2.EXPERIMENTAL TECHNIQUES 45

EXPERIMENTAL METHOD 46

AMBIENT TEMPERATURE DEFORMATION 47

ISOTHERMAL HEAT TREATMENT 52

MEASUREMENT OF GRAIN BOUNDARY CHROMIUM DEPLETION 54

EPR MEASUREMENTS OF GBCD 55

TEM EXAMINATION OF CARBIDE PRECIPITATION . . 59

EXAMINATION OF DEFORMATION MICROSTRUCTURE 60

MATRIX DISLOCATION DENSITY MEASUREMENT . . . 60

ANALYSIS OF DISLOCATION DENSITIES AROUND TWIN BOUNDARIES 62

GRAIN SIZE MEASUREMENT IN SS 63

CHAPTER 3.MATERIAL ANNEAL CONDITION EFFECTS ON GRAIN BOUNDARY CHROMIUM DEPLETION 64

TASK ANALYSIS 65

STAINLESS STEEL COMPOSITION 66

MATERIAL ANNEAL CONDITIONS 67

MICROSTRUCTURAL CHARACTERIZATION OF MATERIAL CONDITIONS 68

MILL PROCESSED MATERIAL MICROSTRUCTURE . . . 68

SOLUTION ANNEALING EFFECTS ON MICROSTRUCTURAL DEVELOPMENT 72

ISOTHERMAL GRAIN BOUNDARY CHROMIUM DEPLETION DEVELOPMENT 82

MILL PROCESSED MATERIAL SENSITIZATION DEVELOPMENT 82

SOLUTION ANNEALING EFFECTS ON SENSITIZATION . 86

EVALUATION OF MATERIAL ANNEAL CONDITION EFFECTS . 94

ANNEALING EFFECTS ON MICROSTRUCTURAL DEVELOPMENT 97
Mill Processed Material Microstructure . 97

Solution Annealed Material Microstructure 97

ISOTHERMAL GRAIN BOUNDARY CHROMIUM DEPLETION DEVELOPMENT 100
Mill Processed Material 100
Solution Annealed Materials 101

MATERIAL SELECTION 104

CHAPTER4. DEFORMATION EFFECTS ON GRAIN BOUNDARY CHROMIUM DEPLETION 105

TASK ANALYSIS 106

MICROSTRUCTURAL CHARACTERIZATION OF DEFORMATION SPECIMENS 107

SOLUTION ANNEALED 1100°C-1HR MATERIAL 107

DEFORMATION EFFECTS ON MICROSTRUCTURAL DEVELOPMENT 108
Matrix Deformation 108
Twin Boundary Deformation 115

DEFORMATION EFFECTS ON ISOTHERMAL GRAIN BOUNDARY CHROMIUM DEPLETION DEVELOPMENT 117

TEST MATRIX 117

SOLUTION ANNEALED 1100°C-1HR SENSITIZATION DEVELOPMENT 119

LOW STRAIN (< 20%) EFFECTS ON SENSITIZATION AT 625°C 121

HIGH STRAIN EFFECTS ON SENSITIZATION AT 625°C 132

TEMPERATURE EFFECTS ON LOW STRAIN INDUCED SENSITIZATION 137

TEMPERATURE EFFECTS ON HIGH STRAIN INDUCED SENSITIZATION 153

CHAPTER 5. FUNDAMENTAL EVALUATION AND MODELING OF DEFORMATION EFFECTS ON GRAIN BOUNDARY CHROMIUM DEPLETION . 158

TASK ANALYSIS 159

ANALYTICAL METHODS FOR THERMODYNAMICS AND KINETIC EVALUATION OF GRAIN BOUNDARY CHROMIUM DEPLETION 161

GBCD KINETICS EVALUATION METHOD 161

GBCD THERMODYNAMICS EVALUATION METHOD 164

THERMODYNAMIC AND KINETIC EVALUATION OF DEFORMATION EFFECTS ON GRAIN BOUNDARY CHROMIUM DEPLETION . 168

STRAIN EFFECTS ON GBCD KINETICS 168

STRAIN EFFECTS ON GBCD THERMODYNAMICS 182

CORRELATION OF THERMODYNAMIC AND KINETIC EFFECTS OF STRAIN WITH AMBIENT DEFORMATION STRUCTURE . . 192

MICROSTRUCTURAL EFFECTS ON GBCD KINETICS . . 195

MICROSTRUCTURAL EFFECTS ON THERMODYNAMICS OF IG CARBIDE PRECIPITATION 199

MICROSTRUCTURAL EFFECTS ON INTRA-GRAIN CARBIDE PRECIPITATION AND TG EPR TEST ATTACK . . 202

MODELING DEFORMATION EFFECTS ON GRAIN BOUNDARY CHROMIUM DEPLETION 205

CHAPTER 6.SUMMARY AND CONCLUSIONS 214

QUANTITATIVE ASSESSMENT OF STRAIN EFFECTS ON GBCD 215

DEFORMATION EFFECTS ON THERMODYNAMICS AND KINETICS OF GBCD 216

CORRELATION OF AMBIENT TEMPERATURE DEFORMATION MICROSTRUCTURE WITH THERMODYNAMIC AND KINETIC EFFECTS OF STRAIN ON GBCD 217

GRAIN BOUNDARY CHROMIUM DEPLETION MODELING 218

MATERIAL ANNEAL CONDITION EFFECTS ON GRAIN BOUNDARY CHROMIUM DEPLETION 219

REFERENCES 220

APPENDIX 1A. SOFTWARE FOR DETERMINING CHROMIUM DIFFUSIVITY 230

APPENDIX 1B. SOFTWARE FOR STRAIN-THERMODYNAMICS COMPUTATIONS 242

APPENDIX 1C. EQUATIONS USED FOR SSDOS MODEL SUBROUTINES 249

APPENDIX 2A. EPRDOS VALUES FOR STRAINED-SENSITIZED SAMPLES 251

APPENDIX 2B. EPRDOS VALUES FOR ANNEALED-SENSITIZED SAMPLES 257

APPENDIX 3. LEGEND 260

VITA 262

FIGURE CAPTIONS

1. Schematic picture of grain boundary chromium depletion in stainless steels illustrating precipitation of chromium-rich carbides on the grain interface (a) and a typical chromium depletion profile developed at a location between two carbides (b). 8

2. Schematic indicating variation of grain boundary chromium depletion with heat treatment, illustrating a thermodynamic chromium minimum Cr_{min} at time t = t_0, and an increase in width of depletion W_{cr} and Cr_{min} values with increasing heat treatment time to t_1 to t_2. 10

3. Uniaxial, static tensile test stress-strain diagram for Type 304 austenitic stainless steels[2]. . . . 12

4. Schematic (a) and experimental (b) demonstration of dislocation emission from grain boundaries at low strains of 0.09% in Type 304 austenitic stainless steels[12,14]. 15

5. Bright-field transmission electron micrographs showing grain boundary ledge structure changes with increasing strain at 0.05% (a), 0.8% (b), 1.5% (c) and 2% (d) strain levels[13]. 16

6. Illustration of strain effects on dislocation densities during cold rolling (a) and tensile straining (b) of Type 304 stainless steel[12,20]. . . 18

7. Transmission electron micrographs documenting the formation of planar twin-faulted regions and their intersections (a) which leads to the formation of ϵ' martensite and α' martensite (b) in Type 304 stainless steels at higher strains[12,24]. 19

8. Evolution of fraction recrystallized (Xv%) with strain, annealing temperature and annealing time for a 0.07%C Type 316 stainless steel[32]. 22

9. Precipitation of chromium carbides on grain boundary ledges in Type 316 austenitic stainless steels[39]. 25

10. Deformation effects on sensitization in Types 304 and 316 austenitic stainless steels. Lines through the graphs show time-temperature required to develop sensitization and produce desensitization for unstrained and strained 304 SS (b) and unstrained and strained 316 SS (b)[46]. 28

11. Documentation of increases in dislocation density in strained Type 316 SS samples after 100 hrs of aging at 625°C[53]. 30

12. Strain effects on sensitization, as indicated by time-temperature-sensitization diagrams for unstrained and strained 18Cr9Ni Stainless Steels containing 0.022%C (1,1'), 0.08%C (2,2') and 17Cr11Ni2Mo stainless steels containing 0.053%C (3,3') and 0.073%C (4,4')[55]. Curves followed by ' represent strained specimens while un-dashed curves represent unstrained specimens. 31

13. Schematic illustration of an edge dislocation showing location of the dislocation pipe at the core of the dislocation line[68]. 37

14. Shape and shape factor (K_j) values for nucleation of simplest precipitate shape on grain boundary[77]. . 42

15. Comparison of deformation effects on sensitization as measured (a) and predicted (b) by Bruemmer[56]. . 44

16. Specimen configurations of variable strain (a) and constant strain tensile specimens (b) used during deformation testing of SS. 48

17. Photograph showing details of 50 kg-f Instron universal testing machine used for deformation testing. 49

18. Plot of variation of strain along gage length for variable strain tensile specimens D2 and D3. . . . 51

19. Photographic illustration of Lucifer box furnace used for sample isothermal treatments. 53

20. Electrochemical Potentiokinetic Reactivation test set up illustrating sample configuration (a), Corrosion Cell (b), model ISI Model WC-5 Potentiostat (c), typical chart record (d) and overall set up (e) for sensitization testing. . . 56

21. Optical micrographs illustrating the uniform, fine grain size on the mill processed material for samples obtained on the outer surface (a) and through thickness (b) of the pipe section. Microstructures were obtained through electroetching of polished stainless steel surfaces with 60% Nitric acid at 1.2V. 69

22. Transmission electron micrographs documenting the dislocation density levels in the matrix (a), twin boundary (b) and grain boundary (c). Also noted is the absence of carbides on the twin and grain interfaces and presence of an extremely small grain in the material(d). 70

23. Solution annealing heat treatment effects on grain size development in Type 316 stainless steel. . . 73

24. Optical micrographs depicting grain size distribution in specimens solution annealed at 1000°C for 1 hr (a), 1050°C for 0.5 hr (b), 1 hr (c) and 4 hrs (d) and 1100°C for 1 hr (e). 74

25. Transmission electron microscope micrographs documenting low deformation levels in the matrix (a,b) and around twin boundaries (c,d) in materials solution annealed for 1 hour at 1000°C and 1100°C respectively. 76

26. Transmission electron micrographs documenting continuous distribution of carbides on selected grain boundaries seen in the bright field (a) and dark field (b), and blocky, irregular carbide precipitation on triple points (c). 78

27. Bright field micrograph (a) and diffraction patterns (b) documenting formation of a massive carbide precipitate and unresolved second phase particles on grain boundaries in the 1050°C -0.5 hour treated specimen. 79

28. Transmission electron micrographs documenting the presence of precipitate-free grain boundaries in samples annealed at 1050°C -1 hour and 1100°C - 1hr. 81

29. Isothermal sensitization behavior of mill processed Type 316 stainless steel portraying three patterns

of behavior corresponding to low (550°C), intermediate (625°C, 670°C) and high (780°C, 850°C) temperatures. 83

30. Optical micrographs illustrating increase in grain boundary attack for mill processed materials treated for 8 - 10 hrs (a) and 26 hours (b) at 625°C. . . 85

31. Sensitization development in the 1100°C - 1hr sample for treatments varying from 550°C to 800°C. . . . 87

32. Comparison of EPRDOS values obtained during heat treatment of the mill processed and 1100°C - 1 hr solution annealed materials at 625°C and 670°C. The data indicates EPRDOS values of the two samples to be similar. 88

33. Comparison of sensitization development of solution annealed material conditions illustrating accelerated sensitization development in 1000°C-1hr,1050°C-0.5,1hr samples over mill processed and 1100°C-1hr samples. 89

34. Comparison of optical micrographs obtained on EPR attack surfaces of 1000°C-1 hr (a), 1050°C-0.5hr (b), 1050°C-1hr (c) and 1100°C-1hr (d) specimens after heat treating at 625°C for 26 hours. 91

35. Illustration of favored EPR test attack on small grains of the dual grain size 1050°C-1hr treated samples after heat treating at 625°C for 10 hrs. . 92

36. Transmission electron micrographs comparing carbide densities in mill processed (a,b), 1000°C-1hr (c,d) and 1100°C-1hr (e,f) materials after heat treating at 625°C for 10 hrs and 26 hrs. 93

37. Time-temperature-sensitization diagram for mill processed 316 SS showing time and temperature treatments required to produce constant or iso-DOS lines of 5, 25 and 60 C/cm^2. 102

38. Deformation effects on increase in matrix deformation as documented in TEM micrographs of specimens deformed to 2% (a), 6% (b) and 16% (c) and in a comparison plot of dislocation density versus strain (d). 109

39. Transmission electron micrograph documenting the presence of a twin-faulted region (a) and cellular dislocation structure (b) in 16% strained Type 316 stainless steel. 111

40. Transmission electron micrographs showing isolated location of second phase appearing similar to α' martensite in 16% strained sample. 113

41. Transmission electron micrograph documenting high density of deformation bands, which intersect at a significant number of locations in the microstructure. 114

42. Transmission electron microscope observations of deformation in the vicinity of annealing twin boundaries for 2% strained (a) and 16% strained (b) specimens. Micrographs were taken under identical [110] foil orientations for an operating reflection of g = (111). 116

43. Time temperature sensitization diagram for 1100°C-1hr unstrained material. 120

44. Comparison of sensitization development in unstrained and 16% strained specimens at 625°C documenting the presence of higher sensitization response in strained versus unstrained specimens. 122

45. Strain effects on sensitization development at 625°C for short (a) and long (b) heat treatment times at this temperature. Both plots clearly illustrate a continuous increase in EPRDOS values with systematic increase in strain. 123

46. Variation of EPRDOS with strain for 625°C - 10 hr heat treatment demonstrating near-linear relationship between EPRDOS and strain for this particular treatment schedule. 125

47. Optical micrographs of EPR test attack surfaces illustrating increase in extent of intergranular attack with strain for 0% (a), 6% (b) and 12% (c) strain levels after a 625°C-7hr heat treatment. . 126

48. Bright field (a) and dark field (b) transmission electron micrographs illustrating carbide precipitation in 16% strained specimens after 20 hrs at 625°C. 128

49. Optical micrographs of EPR test attack surfaces comparing strain effects on extent of intergranular attack for unstrained (a) and 12% strained (b) samples with identical EPRDOS values of 50 C/cm^2. 129

50. Optical micrograph of EPR attack surface illustrating the presence of transgranular etching in the 16% strain specimen after 20 hrs of heat treatment at 625°C. 131

51. Comparison of charge Q (in coulombs) produced during EPR testing of 0%, 16% and 27% strain samples at 625°C demonstrating increase in Q values with increasing strain. 133

52. Optical micrograph of EPR attack surface for 27% strained sample heat treated for 10 hrs at 625°C. 134

53. Transmission electron micrographs documenting locations at which intragranular carbide precipitation was observed on the 27% strain sample heat treated for 20 hrs at 625°C. The locations observed to show intragranular precipitation include regions of dislocations (a,b) and planar deformation (c). No carbide precipitation was observed on the deformation bands present in this material (d). . 136

54. Strain effects on sensitization at 575°C for short (a) and long (b) times of heat treatment. 138

55. Strain effects on sensitization at 670°C for short (a) and long (b) durations of heat treatment. . . 139

56. Strain effects on sensitization at 725°C for short (a) and long (b) durations of heat treatment. . . 140

57. Strain effects on sensitization at 775°C for short (a) and long (b) durations of heat treatment. . . 141

58. Microstructural comparisons of EPR etched surfaces indicating higher levels of intergranular attack on 6% strained versus unstrained specimens after short times of treatment at 775°C (a,b) and similar levels of grain boundary attack in the same conditions after longer heat treatments at 775°C (c,d). . . . 144

59. Comparisons of EPR test attack in unstrained and 16% strained samples at short and long times at 775°C.

The EPR etched surfaces indicate differences in grain boundary attack between samples at short times (**a**) and similar intergranular attack but higher twin boundary attack in **16%** versus unstrained samples at longer times (**b**). 146

60. Transmission electron microscope comparisons of carbide precipitation in unstrained (a) and 16% strained specimens (b) after 0.6 hrs of heat treatment at 775°C. 147

61. Optical micrograph of EPR etched surface revealing the presence of mixed intergranular and transgranular attack on the 16% strain specimen heat treated at 775°C for 0.6 hrs. 149

62. Bright field and dark field transmission electron micrographs documenting the presence of intragranular carbides at the intersection of deformation bands (a) and annealing twins intersecting deformation bands (b) for the 16%-775°C-0.6hr strained sample. 150

63. Three-dimensional time-temperature-strain sensitization diagram documenting the time, temperature and strain level required to achieve an EPRDOS value of 10 C/cm^2 (a) and the shift of EPRDOS surface from 10 C/cm^2 to 35 C/cm^2 (b). 151

64. Time-temperature-strain effects on the induction of transgranular attack in Type 316 stainless steels. This diagram was developed by careful examination of optical micrographs for each sample to document the first time at which TG attack occurred on each material. 154

65. Optical micrograph documenting extensive transgranular attack seen on the 35% strain sample after 10 hrs of heat treatment at 670°C. 155

66. Transmission electron micrographs showing low (a) and high (b) magnification views of carbide precipitation within a twin faulted region for the 35% strain specimen after heat treatment for 10 hrs at 670°C. 157

67. Variation of EPRDOS versus root time at 625°C for unstrained specimens. 170

68. Strain effects on EPR test slope as a function of temperatures from 575°C to 775°C. 172

69. Chromium diffusivity predictions from EPR test slope data for 0 - 16% strain and 575°C -775°C. 173

70. Arrhenius plot of log diffusivity versus strain for the unstrained 1100°C-1hr solution annealed Type 316 SS. 176

71. Arrhenius plot of log diffusivity versus inverse temperature (Kelvin) for 2% strain (a), 6% strain (b), 10% strain (c) and 16% strain (d) data sets. 178

72. Strain effects on chromium diffusivity as illustrated by comparisons of Arrhenius curves for materials strained to different levels. 180

73. Variation of t_0 versus strain (a) and temperature (b). 183

74. Plot of thermodynamic barrier to nucleation as a function of temperature (a) and strain (b), assuming grain boundary dominated nucleation kinetics. . . 189

75. Plot of nucleation related change in grain boundary energy versus strain (a) and temperature (b). . . 190

76. Comparison of chromium diffusivity values predicted by the Hart dislocation pipe diffusion model with experimental diffusivity data obtained in this work. 198

77. Conceptual view of grain boundary energy distribution in annealed materials (a) and strain effects on grain boundary energy and intergranular carbide precipitation (b). 200

78. Conceptual view of strain effects on intra-grain versus inter-grain carbide precipitation and GBCD development. 204

79. Phenomenological model for deformation effects on grain boundary chromium depletion illustrating effects of increasing strain and heat treatment on microstructural development in the material. . . . 206

80. Comparison of SSDOS predicted versus experimental diffusivities (a) and nucleation times (b) for strained austenitic SS. 208

81. Comparison of SSDOS predicted versus experimental EPRDOS for Type 316 SS at 575°C (a) and 625°C (b). 209

82. Comparison of SSDOS predicted versus experimental EPRDOS values for strain effects on sensitization at 670°C (a) and 725°C (b). 210

83. Comparison of SSDOS predicted and experimental EPRDOS values at 775°C. 211

84. Comparison of (modified) SSDOS predictions versus experimental EPRDOS values in the range of 575°C to 775°C. 213

LIST OF TABLES

1. Electrochemical Potentiokinetic Reactivation test parameters for Type 316 stainless steel 57

2. Chemical Composition of high Carbon 316SS 66

3. Temperature and time conditions employed for solution annealing 316 SS 67

4. Matrix of deformation specimens and heat treatment schedules used for analysis of GBCD in 316 SS. . . 117

5. Variation of times to start sensitization (t_0), experimental slopes and chromium diffusivities as a function of strain and heat treatment 169

6. Comparison of diffusion equations computed for the unstrained and strained materials with available literature 179

7. Conversion of t_0 values to t_n values by subtraction of the effect of t_{depl}. 184

8. Thermodynamic barrier to nucleation ΔG^* computed assuming matrix diffusivity of chromium 186

9. Thermodynamic barrier to nucleation predicted from grain boundary diffusion. 188

ABSTRACT

Deformation Effects on the Development of Grain Boundary Chromium Depletion (Sensitization) in Type 316 Austenitic Stainless Steels

Ashok H. Advani, Ph.D.

Oregon Graduate Institute of Science and Technology, 1990

Supervising Professor: David G. Atteridge

Deformation induces an acceleration in the kinetics and a reduction in the thermodynamic barrier to carbide precipitation and grain boundary chromium depletion (GBCD) development of a high carbon Type 316 stainless steel (SS). This was observed in a study on strain effects on GBCD (or sensitization) development in the range of 575°C to 775°C. Grain boundary chromium depletion behavior of SS was examined using the indirect electrochemical potentiokinetic reactivation (EPR) test and supported by studies on carbide precipitation using transmission electron microscopy (TEM).

The alterations in thermodynamics and kinetics of GBCD development with strain were found to result in a systematic increase in degree of sensitization (DOS) of the material. The acceleration in DOS with strain was, however, more prominent at temperatures between 550 to 700°C than 700 to 800°C.

Strains above 20% also yielded the presence of a time-temperature-strain dependent transgranular (TG) attack during EPR testing. This was induced by precipitation of carbides on the deformation structure of the material.

Analytical methods developed to quantify chromium diffusivity from EPR test data indicated that a decrease in the activation barrier to diffusion, (Q_a)occurred with increasing strain. Quantification of the thermodynamic barrier to nucleation, (ΔG^*) likewise indicated a lowering in the ΔG^* with strain, and was related to an increase in the free energy change of the grain boundary, (ΔG_{gb}) during strain-induced nucleation. The effect of strain on Q_a, ΔG^* and ΔG_{gb} was also measured to decrease with increasing temperature.

Examination of the (ambient temperature) deformation microstructure showed that the GBCD kinetic effects were due to increased dislocation pipe diffusion of chromium with increasing strain. Thermodynamic changes were attributed to a change in the ledge structure, and energetics, of the grain boundary, while TG attack was considered to occur due to creation and increase in energy of intra-grain sites during the straining process.

Comparison of predictions of deformation effects on GBCD using an empirical sensitization model with experimental data obtained in this work indicated the model overpredicted DOS values at all strain and heat treatment schedules. Modifications to the model using the thermodynamic and kinetic data developed in this work resulted in an improvement in the predictive capability of this model.

CHAPTER 1

INTRODUCTION

OVERVIEW

Thermomechanical (TM) processing and fabrication treatments used to produce commercial materials range from simple isothermal annealing treatments to complex multi-pass welding operations. These TM treatments induce thermal and strain cycles in the material, which interact with the existing material condition, resulting in the final microstructure and microchemistry of the product. The achievement of desired properties in the product is critically dependent on an understanding of TM treatment effects on microstructure and microchemistry development. Research on the phenomena is important for improvement of material reliability and performance in service.

Stainless steels (SS) offer a simple system of commercial interest where the effects of TM treatment on microstructure and microchemistry development can be studied. SS are susceptible to the development of grain boundary chromium depletion (GBCD), or sensitization, during TM processing and fabrication operations. The depletion is induced by the precipitation of chromium-rich carbides on the grain interfaces, and is affected by both thermal and strain cycles induced in the material during TM treatment. However, while

thermal treatment effects on sensitization have been studied and modeled by numerous researchers, the effects of deformation on GBCD development are relatively unknown. A fundamental understanding of the phenomena is, likewise, lacking and needs to be developed as a first step towards understanding mechanisms of TM treatment effects on microstructure-microchemistry development in SS and other materials.

Research on deformation effects on GBCD is also useful in understanding intergranular (IG) corrosion and IG stress corrosion cracking (SCC) susceptibility of boiling water reactor (BWR) SS piping during fabrication and/or service life. Earlier work based on simple thermal cycle simulation of TM operations indicated that sensitization of SS piping was the main cause for the SCC related failures observed in these systems. The thermal studies did not refer to the contribution of TM induced strain on sensitization and the mechanism of failures in these systems is, therefore, only partially understood. A more complete picture of the overall phenomena can, however, be developed through fundamental research on deformation effects on sensitization in SS.

RESEARCH OBJECTIVE

The objective of this research was to develop a fundamental understanding of deformation effects on grain boundary chromium depletion phenomena in SS.

Research areas that were investigated in this work include:

* Quantitative assessment of strain effects on GBCD

* Evaluation of strain-induced isothermal GBCD development based on the kinetics and thermodynamics of the carbide precipitation and chromium depletion process.

* Correlation of sensitization thermodynamics and kinetics with the ambient temperature deformation microstructure of SS.

* Extension of the current deformation-sensitization models to encompass the kinetic and thermodynamic effects of strain on GBCD development.

These areas of research were selected to extend the present understanding of strain effects on precipitate nucleation, growth and GBCD development in SS, towards achievement of an understanding of TM treatment effects on microstructure, microchemistry and property development in materials.

A detailed study on

* material anneal condition effects on GBCD

was also carried out. The work resulted in selection of a suitable annealing treatment for the deformation study.

Other related areas of research which are also being investigated in companion studies at Oregon Graduate Institute of Science and Technology and Battelle Pacific Northwest Laboratory. These include studies on deformation effects on continuous cooling sensitization (CCS) development in SS, phosphorous segregation and carbide precipitation effects on IG fracture in SS, and sensitization modeling in SS during TM treatment. The research is intended to further contribute to the basic understanding of TM processing and fabrication effects on material properties, reliability and performance during service.

BACKGROUND

The background information for the thesis work is described in the following sections:

* Development of Grain Boundary Chromium Depletion (Sensitization) in Stainless Steels
* Plastic Deformation of Stainless Steels
* Deformation Effects on Grain Boundary Chromium Depletion Development
* Modeling Deformation Effects on Grain Boundary Chromium Depletion

These sections are essentially a review of the available literature on deformation-induced sensitization development in SS and other concepts useful in the understanding of the phenomena.

GRAIN BOUNDARY CHROMIUM DEPLETION IN STAINLESS STEELS

The corrosion resistance of SS is attributed to the presence of a chromium-rich passive oxide film, which protects the surface of the alloy. Thermomechanical treatments involving isothermal holding in, or slow cooling through 500°C - 800°C, however, induce the precipitation of $M_{23}C_6$ chromium-rich carbides on the grain boundary (Figure 1a), which due to the relatively slow chromium versus carbon diffusivity, causes a substantial volume of chromium to be drawn from the region around the carbide[1]. This leads to the development of GBCD (Figure 1b) and local breakdown of the passive film in the grain boundary region which renders the alloy susceptible to IG corrosion and IGSCC in certain aqueous environments (for eg., high temperature oxygenated water in BWRs).

Grain boundary chromium depletion in SS is dependent on the thermodynamics of carbide precipitation and kinetics of chromium diffusion. The process involves

* Nucleation of carbides after a time t_n, leading to the formation of a depleted zone with a thermodynamic chromium minimum Cr_{min} and negligible width of chromium depletion W_{cr}.

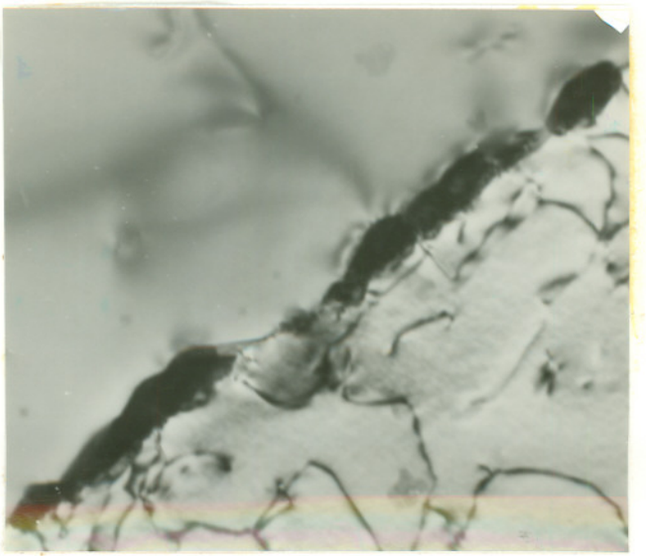

(a) 0.1 μm

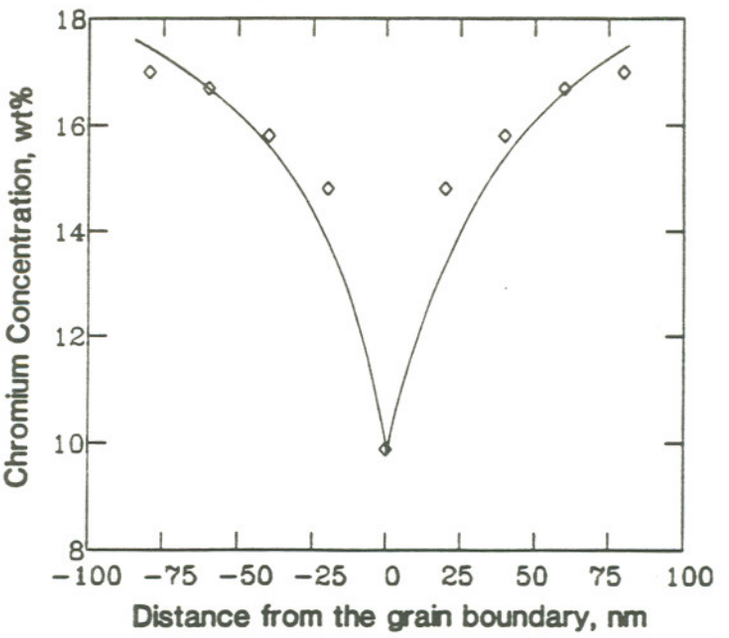

(b)

Figure 1. Schematic picture of grain boundary chromium depletion in stainless steels illustrating precipitation of chromium-rich carbides on the grain interface (a) and a typical chromium depletion profile developed at a location between two carbides (b).

* Diffusion of Chromium from matrix to grain boundary which increases W_{cr} and also eases the concentration gradient between the matrix and the grain interface.

* Increase in Cr_{min} (or desensitization) at the grain interface caused by continuously reducing matrix carbon content during carbide precipitation.

These processes result in changes of GBCD with heat treatment, as summarized in Figure 2.

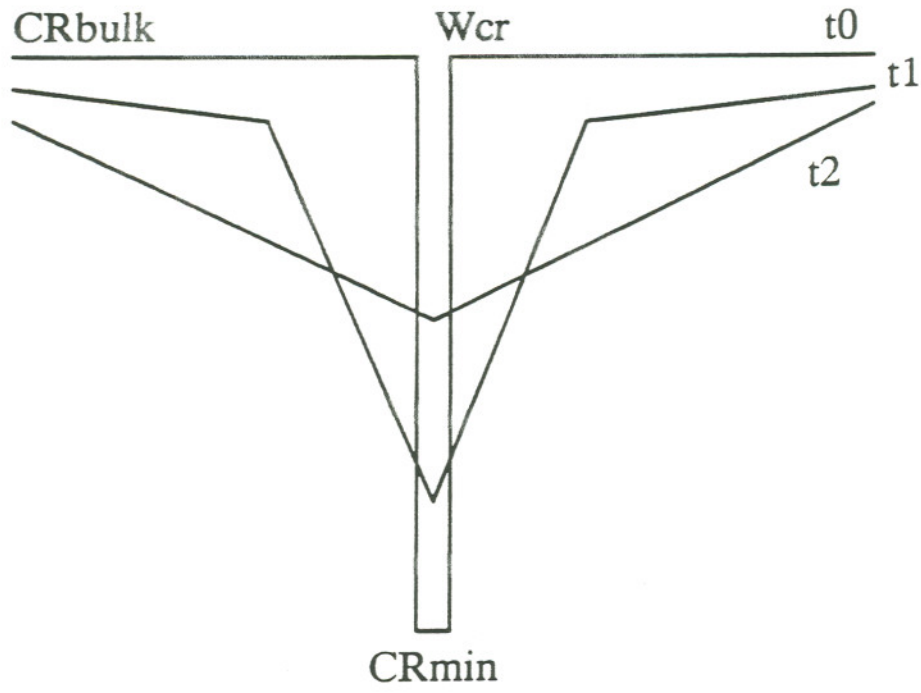

Figure 2. Schematic indicating variation of grain boundary chromium depletion with heat treatment, illustrating a thermodynamic chromium minimum Cr_{min} at time $t = t_0$, and an increase in width of depletion W_{cr} and Cr_{min} values with increasing heat treatment time to t_1 to t_2.

PLASTIC DEFORMATION OF AUSTENITIC STAINLESS STEELS

Plastic deformation refers to the permanent deformation that a material undergoes during a process that produces a stress that exceeds the yield stress of the material. Deformation characteristics of materials are dependent on the stress state (uniaxial, biaxial or triaxial), stress mode (tensile or compressive), strain-rate and temperature of the straining process. The concepts presented here, however, only consider ambient temperature deformation behavior of SS during uniaxial, slow strain-rate tensile straining of the alloy.

Macroscopic Deformation of Austenitic SS

The macroscopic deformation behavior of SS is best characterized using a stress strain diagram, as illustrated typically for Type 304 SS in Figure 3[2]. This diagram indicates that SS undergoes plastic deformation beyond the yield stress (σ_{ys}). The strain during plastic deformation increases non-linearly with stress up to the ultimate tensile stress (σ_{uts}), where plastic instability and failure of the SS is initiated. The σ_{ys}, σ_{uts} and strain to failure for a typical annealed 304 SS are approximately 200 MPa, 600 MPa and 60% respectively. Variations in these parameters amongst different heats of Type 304 SS and other grades of austenitic SS are, however, present.

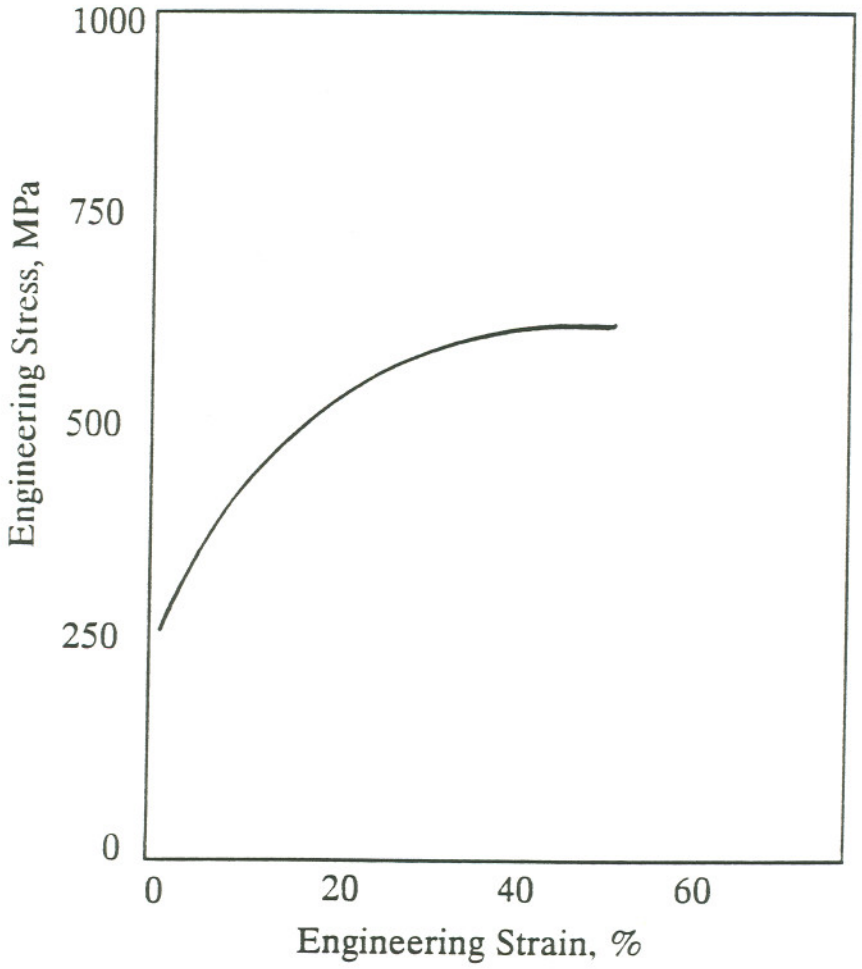

Figure 3. Uniaxial, static tensile test stress-strain diagram for Type 304 austenitic stainless steels[2].

Microstructural Effects of Strain

The macroscopic deformation described by the stress-strain diagram for SS occurs due to microstructural changes induced during tensile straining of the SS. These microstructural effects have been described by outlining the theory of plastic deformation[3,4] in materials, and supporting it with observations made in specific grades of SS.

The earliest change that occurs during plastic deformation is on point defects, which can as a first approximation be considered through deformation effects on vacancy concentration[3]. The concentration of strain-induced vacancies (n) increases proportional to the strain (ϵ) and can be determined by the relationship

$$n/N = (10^{-5} \text{ to } 10^{-6})\epsilon$$

where N = Number of atoms/mole

Details on strain-induced vacancy formation in SS are, however, not well documented.

Grain boundaries also experience plastic deformation during the early stages of straining, and publications documenting their deformation behavior have been presented and reviewed

by many researchers[5-17]. Dislocation movement is initiated in the grain boundary plane even below the bulk yield stress of the material. The glide of these dislocations is often hindered by the presence of grain boundary structural defects (or ledges) and leads to a pile up of dislocations on the ledge. This pile-up exerts a local stress on the ledge which, due to stress concentration, results in grain boundary dislocation emission and higher dislocation densities in the vicinity of the grain interface (Figure 4). Interactions amongst dislocations and between dislocations and ledges on the boundary also occur resulting in the formation of additional ledges in the grain boundary (Figure 5).

Matrix dislocations emitted from the grain boundary possess the ability to multiply easily at heavy deformations, have high mobility and are also capable of oriented movement under the action of external applied stresses[3,4]. Increasing strain results in an increase in the matrix dislocation density (d)[12, 18-20] which may be related to the strain ϵ through the relation[12,18,19]

$$d = d_o + A\epsilon$$

where A = a materials constant
d_o = the initial dislocation density

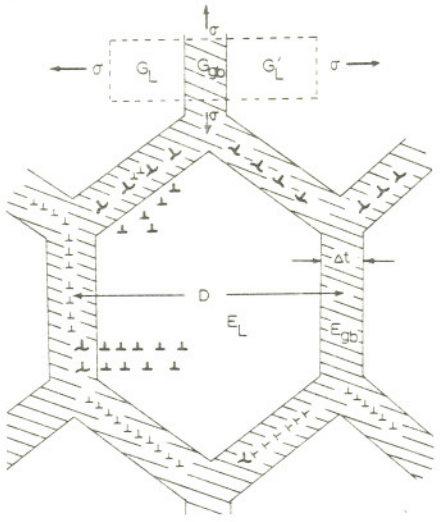

(a)

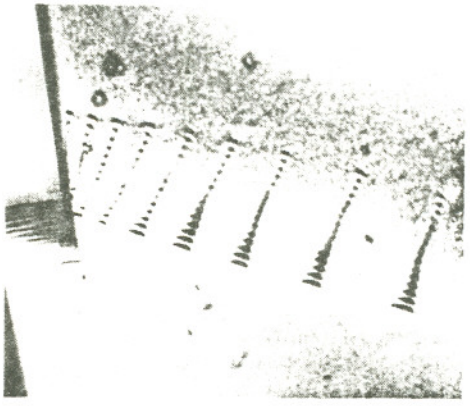

(b)

Figure 4. Schematic (a) and experimental (b) demonstration of dislocation emission from grain boundaries at low strains of 0.09% in Type 304 austenitic stainless steels[12,14].

(Reprinted with permission from Dr. L.E. Murr, University of Texas at El Paso)

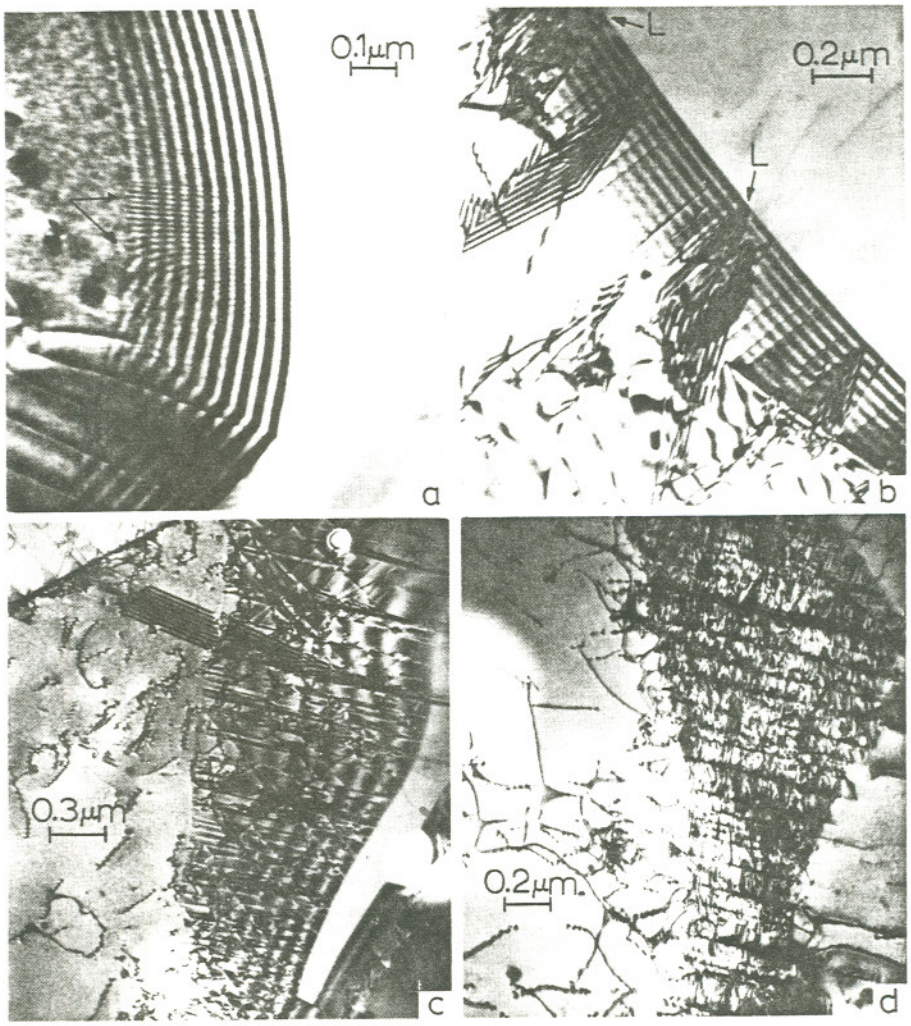

Figure 5. Bright-field transmission electron micrographs showing grain boundary ledge structure changes with increasing strain at 0.05% (a), 0.8% (b), 1.5% (c) and 2% (d) strain levels[13].

(Reprinted with permission from Dr. L.E. Murr, University of Texas at El Paso)

This fact is also alluded to in Figures 6(a) and 6(b) where a near-linear rise in matrix dislocation density with strain is seen during cold rolling or tensile straining of SS. An observation also made in Figure 6(b) is that at low strains the dislocation density in the vicinity of the grain boundary is higher than the matrix, while at higher strains, matrix dislocations swamp the entire microstructure and little differences between bulk and grain boundary dislocation densities are noted.

Dissociation of dislocations into partial dislocations and stacking faults often occurs simultaneous with dislocation density changes in FCC materials[3,4]. This is especially true for austenitic SS, and is attributed to the relatively low stacking fault energy (SFE) of SS which makes it energetically favorable to form (wide) stacking faults (and partial dislocations) rather than create additional dislocations or cross slip[12]. The prevention of cross slip also gives the deformation structure of austenitic SS a planar appearance (Figure 7a), though the extent of planarity depends on the SFE of the specific grade of SS.

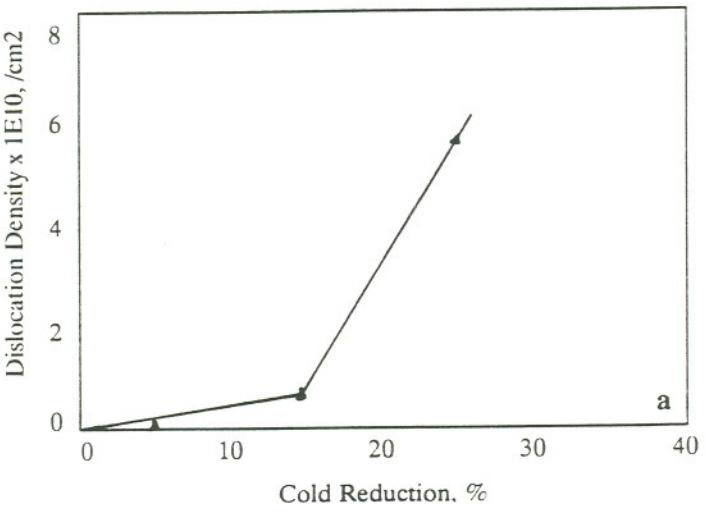

(a)

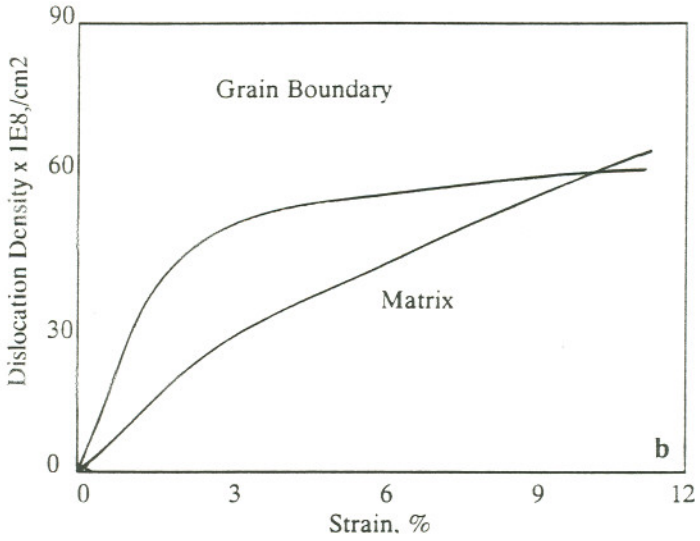

(b)

Figure 6. Illustration of strain effects on dislocation densities during cold rolling (a) and tensile straining (b) of Type 304 stainless steel[12,20].

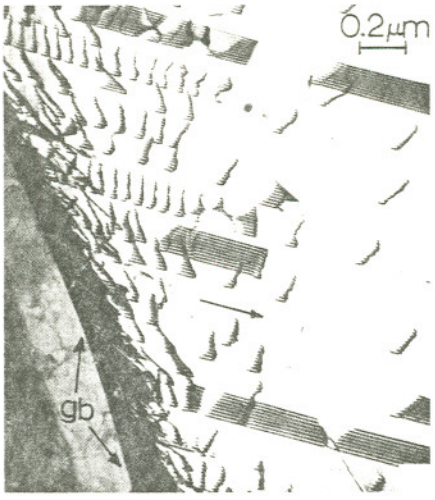

(a)

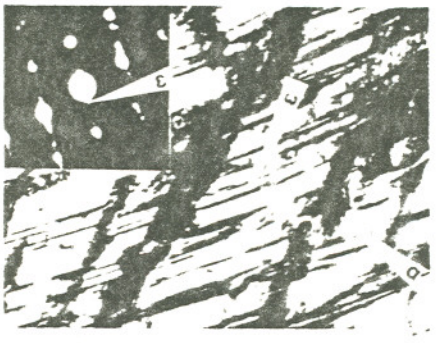

(b)

Figure 7. Transmission electron micrographs documenting the formation of planar twin-faulted regions and their intersections (a) which leads to the formation of ϵ' martensite and α' martensite (b) in Type 304 stainless steels at higher strains[12,24].

(Reprinted with permission from Dr. L.E. Murr, University of Texas at El Paso).

Stacking faults in SS overlap at higher strains forming irregular areas which are twinned and also contain hexagonal close packed ϵ regions[12]. Identification of individual faults and twins in these heavily deformed regions is difficult, and the mix of twins and fault structures are often called "twin-faults". Intersections between twin-faults produced at higher strains which satisfy crystallographic conditions proposed by Olsen and Cohen[21,22] form BCC α'-martensite at the intersection (Figure 7b). The occurrence of significant levels of martensite in Type 304 SS has been documented by numerous researchers[23-29], though Type 316 SS has been reported to not form martensite during straining[30].

DEFORMATION EFFECTS ON ISOTHERMAL GRAIN BOUNDARY CHROMIUM DEPLETION IN STAINLESS STEELS

Concepts

J.W. Christian[31] has postulated that cold working accelerates reaction rates in materials due to its effects on

* Increasing the vacancy concentration leading to increased diffusivity
* Lowering the activation barrier to diffusion
* Decreasing the free energy barrier to nucleation
* Increasing the effective driving force for nucleation

Christian[31] also proposed that the effects of plastic deformation on transformation kinetics is dominant only up to temperatures at which internal stresses cannot be removed rapidly by recovery or recrystallization.

Extrapolating these theories to GBCD in SS suggests that the thermodynamic and kinetic aspects of the phenomena can be expected to be altered by deformation until recovery and recrystallization of the alloy occurs. Time, temperature and strain conditions observed to cause recrystallization in a 0.07% Type 316 SS are summarized in figure 8[32].

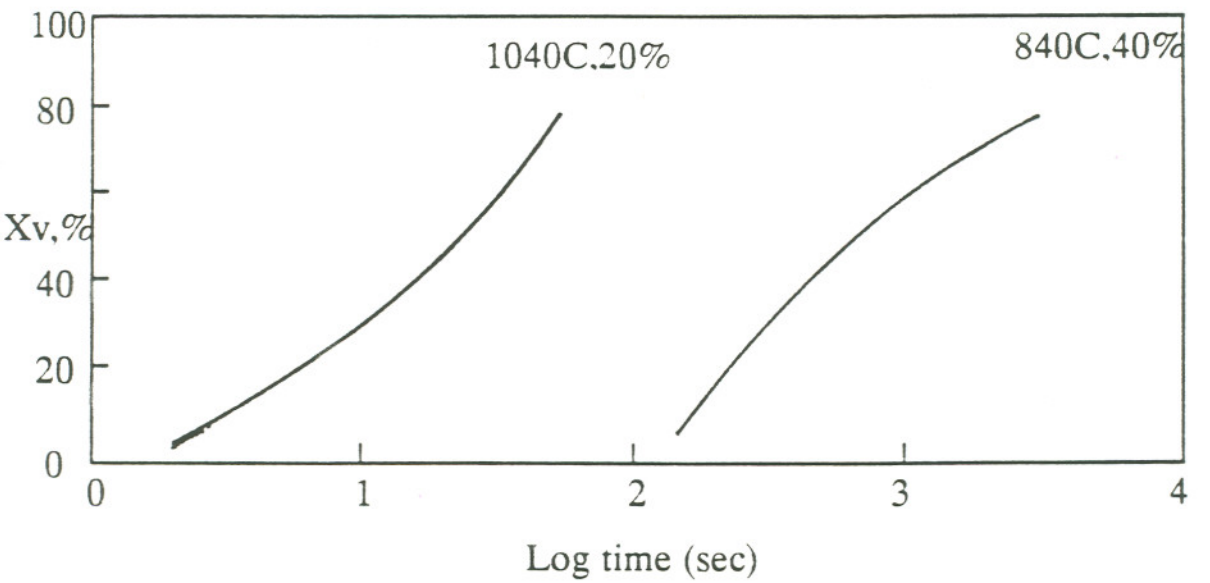

Figure 8. Evolution of fraction recrystallized (Xv%) with strain, annealing temperature and annealing time for a 0.07%C Type 316 stainless steel[32].

The formation of vacancies during deformation can increase chromium diffusivity in SS during low temperature thermal treatment. This is because the diffusion of chromium in SS occurs by substitutional diffusion, which requires transport of atoms through the presence of vacancies in the vicinity of the diffusing atom[33-35]. However, an increase in the vacancy concentration during deformation is not anticipated to play a critical role in sensitization development as annhiliation of strain-induced vacancies usually occurs well below the sensitization temperature range for SS[33-35].

A reduction in the activation barrier to diffusion (Q_a) with strain is anticipated due to increased dislocation density and dislocation pipe diffusion of chromium. A number of papers illustrating this aspect for other systems have also been written and reviews evidencing this are available in the work of Gjostein[36] and Baluffi[37]. Additional factors which can also contribute to increased diffusivity in SS are chromium segregation to dislocations, dislocation sweeping to grain boundaries and martensite formation during straining of SS.

Classical nucleation theory considers the effect of deformation on the free energy barrier to nucleation (ΔG^*) based on formation of nuclei on dislocations created during

straining[38]. This is because heterogeneous nucleation on dislocations results in a destruction of the strain field around the dislocation which favors its occurrence over random, homogeneous nucleation on undistorted lattice sites.

The effect of deformation on grain boundary chromium carbide nucleation during sensitization is more complex to consider because IG precipitation already lowers ΔG^* by destruction of the strain field around the grain boundary. There is, however, a possibility of changes in ΔG^* due to increases in grain boundary ledge densities during deformation of SS[12,13]. This is because ledges are high energy sites within grain interfaces which accelerate nucleation versus the overall grain boundary[39-43] (Figure 9).

An additional factor which can play a role in lowering the ΔG^* is the formation of martensite during deformation. Martensite laths are also high energy sites within the grain which may compete with the grain boundary for nucleation. This can result in mixed IG and intragranular precipitation and cause changes in GBCD development.

Figure 9. Precipitation of chromium carbides on grain boundary ledges in Type 316 austenitic stainless steels[39].

The increase in the effective driving force for nucleation (ΔG_v) with strain, postulated by Christian, suggests an increase in the chemical activity of chromium and carbon, which are involved in chromium carbide nucleation. This can occur if local enrichment of chromium and carbon on matrix and grain boundary defect structures occurs with increasing strain. Segregation of elements to grain boundaries in SS are well documented though implications towards nucleation are not discussed.

Literature Observations

Deformation effects on GBCD have been studied for various deformation and heat treatment combinations which include application of strain prior to, and simultaneous with, isothermal or continuous cooling heat treatment cycles. This review covers the available literature on the effect of prior (or ambient temperature) straining on isothermal sensitization applicable to the current research.

Prior deformation effects on isothermal sensitization were first investigated by Bain et al[1] and Tedmon et al[44] for Type 304 SS strained to 50 -55%. Results on these studies indicated that deformation produced accelerated development of chromium depletion in SS. The sensitization susceptibility of the SS

was, however, considered less severe since the depletion was spread over both grains and grain boundaries, rather than being concentrated at the grain boundary.

Briant and Ritter[45-48] noted accelerated sensitization and desensitization development in 304 and 316 SS strained to high levels (close to σ_{uts}), as shown in Figure 10. The acceleration was more prominent in 304 SS over 316 SS due to formation of martensite, and thereby faster diffusivity of chromium, for 304 SS. Formation of martensite accelerated carbide precipitation on martensite laths, as evidenced by transmission electron microscopy (TEM)[46,49], and also induced transgranular (TG) attack[45-49] on depleted regions around laths during sensitization testing.

Extensions of the above high strain studies on sensitization to a wider range of strains (0-50%) for Type 304 SS[50,51], Type 304L SS[52] and Type 316 SS[53] asserted the presence of deformation induced-accelerated sensitization through the entire range of strains. The dominant effect of martensite in Type 304 SS was also confirmed at higher strains. At lower strains and for Type 316 SS deformation effects on increasing sensitization was postulated to be due to increases in dislocation density and chromium diffusivity with strain.

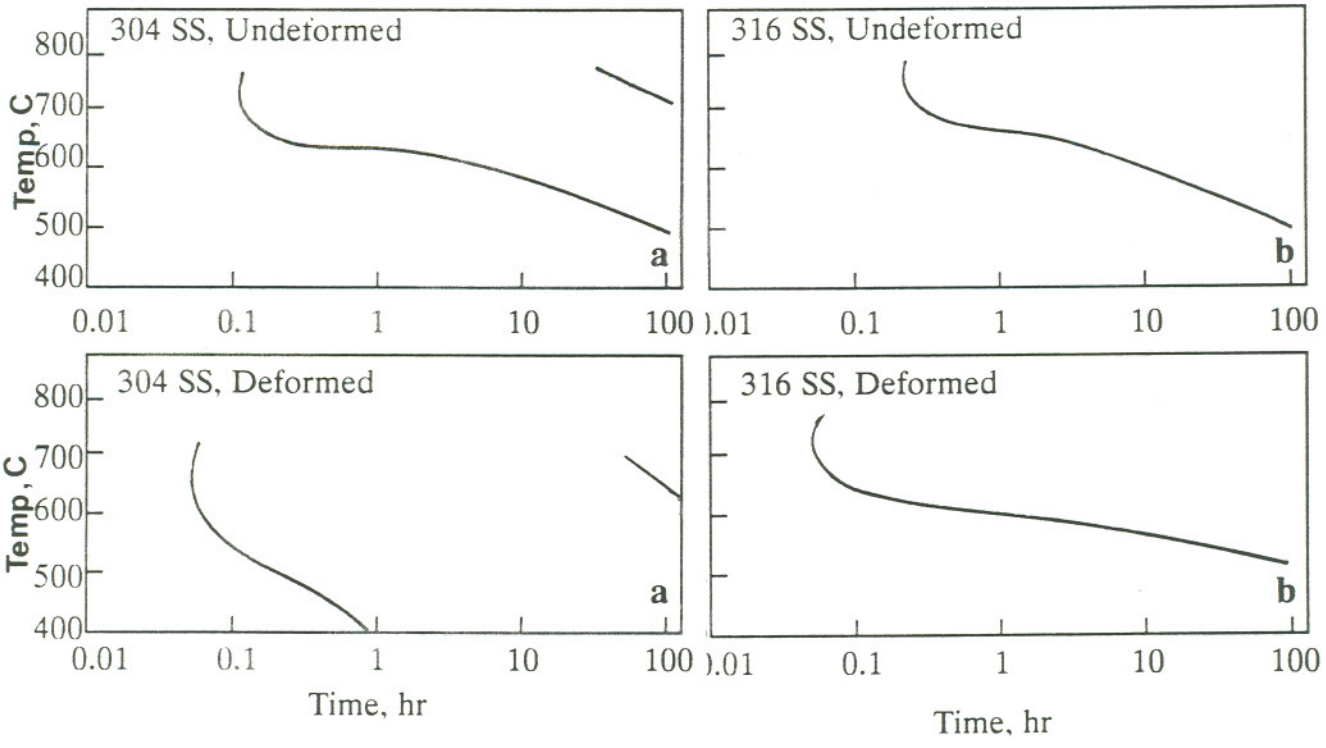

Figure 10. Deformation effects on sensitization in Types 304 and 316 austenitic stainless steels. Lines through the graphs show time-temperature required to develop sensitization and produce desensitization for unstrained and strained 304 SS (b) and unstrained and strained 316 SS (b)[46].

Measurements illustrating increases in dislocation density with strain in sensitized samples have also been made (figure 11[53]).

The effects of cold deformation on sensitization have been summarized as time-temperature-sensitization (TTS) diagrams for 304 and 316 SS[54,55] (Figure 12). These diagrams indicate the time-temperature heat treatments required to develop sensitization in SS, and were used to compare sensitization behavior of 20 - 50% strained versus unstrained SS. The TTS diagram for strained materials is seen to be to the left of and below that of unstrained materials in all cases. This indicates that deformation reduces the time to develop sensitization and also the maximum temperature at which sensitization occurs for the alloy. It substantiates the fact that deformation accelerates the occurrence of sensitization and desensitization in 304 SS and 316 SS, as observed by various researchers.

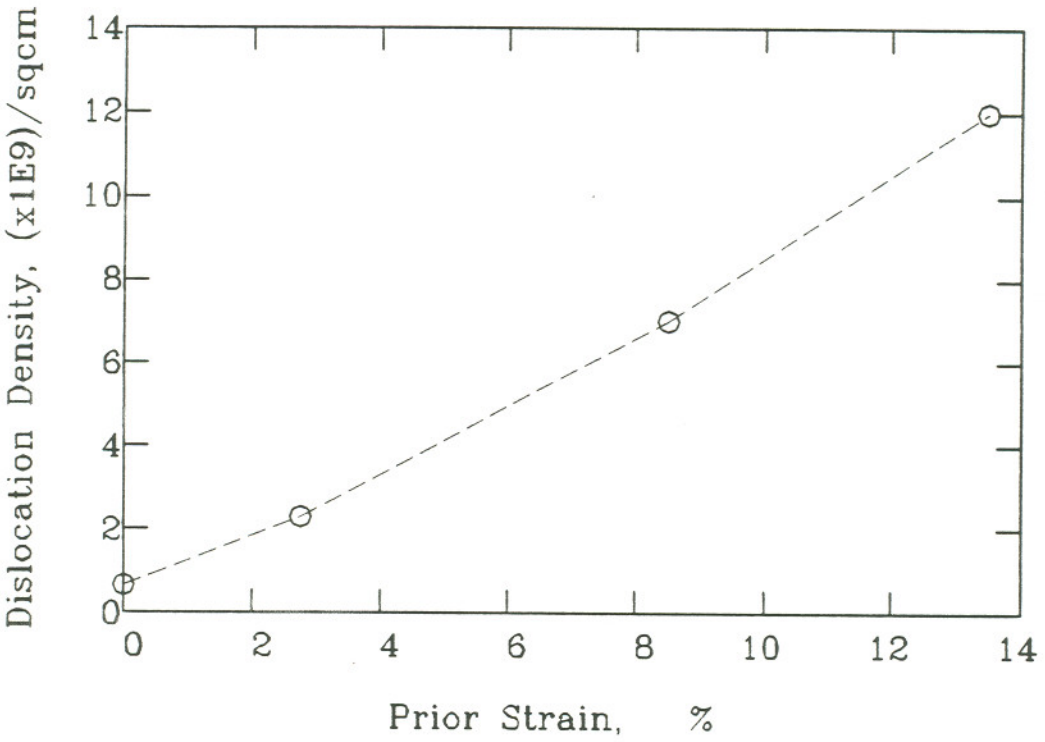

Figure 11. Documentation of increases in dislocation density in strained Type 316 SS samples after 100 hrs of aging at 625°C[53].

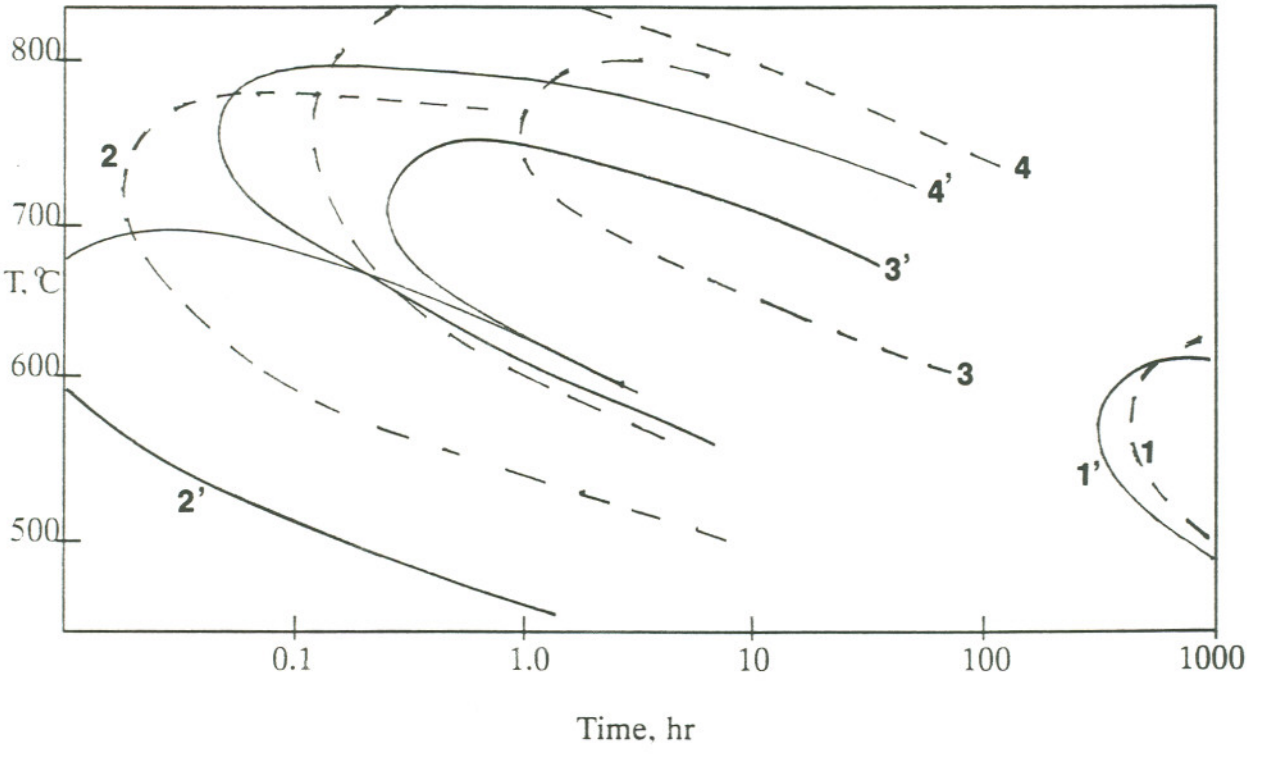

Figure 12. Strain effects on sensitization, as indicated by time-temperature-sensitization diagrams for unstrained and strained 18Cr9Ni Stainless Steels containing 0.022%C (1,1'), 0.08%C (2,2') and 17Cr11Ni2Mo stainless steels containing 0.053%C (3,3') and 0.073%C (4,4')[55]. Curves followed by ' represent strained specimens while un-dashed curves represent unstrained specimens.

MODELING DEFORMATION EFFECTS ON GRAIN BOUNDARY CHROMIUM DEPLETION

Grain Boundary Chromium Depletion Modeling

Modeling of GBCD in SS requires the ability to model the thermodynamic Cr_{min}, nucleation time t_n, depletion width W_{cr} and desensitization which are critical to the phenomena.

The thermodynamic chromium minimum is modeled by considering equilibrium for the reaction

$$23Cr + 6C = Cr_{23}C_6$$

This reaction assumes that the $M_{23}C_6$ carbide is entirely $Cr_{23}C_6$, and equates the Cr_{min} value to

$$Cr_{min} = \frac{1}{(\gamma_{cr}) * (k.\ \gamma_c^{\,6}.\ X_c^{\,6})^{1/23}}$$

where
- k = the equilibrium constant for $Cr_{23}C_6$ formation
- γ_{cr} = the chromium activity coefficient
- γ_c = the carbon activity coefficient
- X_c = the mole fraction of carbon in equilibrium with the carbide

Much of the work in modeling chromium minimums has been in determining the activity coefficient terms in the above

expression, while assuming Xc is equivalent to the mole fraction of carbon in the matrix and k, the equilibrium constant is given by

$$k = \exp(-\Delta G/RT)$$

where ΔG = free energy change involved in the chromium carbide precipitation reaction
R = gas constant
T = temperature in degree Kelvin

The approaches used[57-59] to determine the activity coefficients have been based on methods developed by Wagner[60] and Kohler[61] and involve considering complex interactions between the various elements involved in the reaction. Bruemmer[56] has also empirically adjusted these parameters to fit Cr_{min} values measured using scanning TEM -electron dispersive x-ray (STEM-EDS) analyses of GBCD.

Nucleation time t_n for chromium carbide precipitation is modeled by equating it to the time required to develop a minimum number of critical nuclei (N_c) at the grain boundary and is given by

$$t_n = \frac{N_c}{c} \exp\frac{Q_a}{RT} \exp\frac{\Delta G^*}{RT}$$

where c = nucleation rate constant

and ΔG^*, Q_a, R and T represent the thermodynamic barrier to nucleation, activation barrier to diffusion, gas constant and temperature, as given earlier. This equation is essentially the inverse of the classical nucleation rate equation developed by Becker[62] and Christian[31], and was modified for the chromium carbide nucleation by Logan[63] using the approach developed by Grobner[64].

The width of chromium depletion W_{cr} (taken at the bulk chromium (Cr_{bulk}) level on the depletion profile) is estimated by relating to the chromium diffusivity (D_{cr}) and heat treatment time t using the relation[65]

$$W_{cr} = 2\sqrt{D_{cr}t}$$

This relation assumes the presence of a continuous chromium-carbide film on the grain boundary and the completion of nucleation prior to its application. The width (W_x) corresponding to any chromium concentration Cr_x on the depletion profile may also be estimated using the inverse of the equation

$$Cr_x = Cr_{min} + (Cr_{bulk} - Cr_{min})\ \mathrm{erf}\ (W_x/2\sqrt{D_{cr}t})$$

This equation is a solution to Fick's second law of diffusion modified by Thorvaldasson[66] for direct application to GBCD width determination in SS. It also reverts to the $2\sqrt{D_{cr}t}$ value at the bulk chromium level through the boundary condition $Cr_x = Cr_{bulk}$.

Desensitization may be modeled by increasing Cr_{min} towards Cr_{bulk} to maintain equilibrium with a continuously increasing matrix carbon level. The increase in Cr_{min} with time (Cr_t) has, however, only been modeled[56] empirically using the relation

$$Cr_t = Cr_{min} + (13.5 - Cr_{min}) \left(\frac{k \, t_n \, D_{cr}}{t_{ds}} \right)^2$$

where k = an empirical constant
t_{ds} = time to desensitize the SS

The desensitization time t_{ds} essentially refers to the time to eliminate the chromium depletion (assumed at 13.5% chromium level) existing at the grain boundary. Stawstrom and Hillert[65] proposed a simple empirical relation to estimate t_{ds} as

$$t_{ds} = \left(\frac{GS.\ C}{(X_{crb} - 0.13)\ \sqrt{D_{cr}}} \right)^2$$

where GS = grain size of the material
X_{crb} = bulk chromium in the material expressed as a mole fraction
C = Carbon Content of the material

Verification of the predictive capability of the desensitization equations is, however, limited due to lack of experimental documentation on the phenomena[56].

Deformation Effects Modeling

Deformation effects on kinetics and thermodynamics of precipitation reactions is modeled through dislocation-pipe diffusion effects on the activation barrier to diffusion and dislocation energy effects on the thermodynamic barrier to nucleation, as summarized below.

Dislocation pipe diffusion effects on the activation barrier to nucleation has been modeled by numerous researchers. The earliest and simplest model on the phenomena was developed by Hart[67]. This model considered that the distorted pipe around the dislocation core (Figure 13[68]) would lead to increased diffusivity depending on the fraction of time spent by an atom in the pipe versus a regular lattice site. Statistical analysis based on this concept determined that the total diffusivity (D_{tot}) in a material is related to the

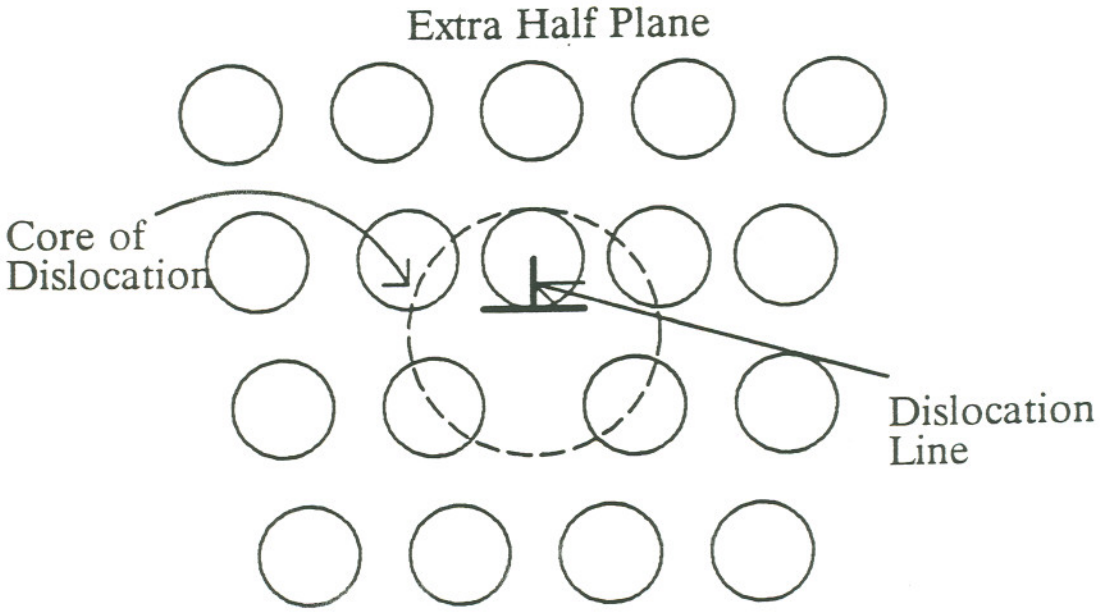

Figure 13. Schematic illustration of an edge dislocation showing location of the dislocation pipe at the core of the dislocation line[68].

(undistorted) lattice diffusivity and the dislocation pipe diffusivity through

$$D_{tot} = D_o \exp(-Q_a/RT) + n A D_{o,p} \exp(-Q_{a,p}/RT)$$

where

D_o	=	Diffusion coefficient for lattice diffusion
Q_a	=	Activation barrier for lattice diffusion
A	=	Area of dislocation pipe
n	=	Dislocation density
$D_{o,p}$	=	Diffusion coefficient for pipe diffusion
$Q_{a,p}$	=	Activation barrier for pipe diffusion
R	=	Gas Constant
T	=	Temperature in degrees Kelvin.

Ruoff and Baluffi[69] later placed restrictions on the Hart theory and professed that it would be valid only if

$$\sqrt{Dt} >> L$$

where L = the dislocation spacing.

This condition was developed by considering that the basic assumptions of the Hart theory were only valid if the diffusing atom visited a large number of dislocations during the diffusion process and implied that the Hart theory worked well for large dislocation densities and long heat treatment times.

Work by Morrison[70], Asai and Gupta[71] and Le Claire[72], however, indicated that the Ruolff and Baluffi condition was too restrictive. Le Claire[72] also suggested that the basic assumptions of the Hart model were satisfied if

$$\sqrt{Dt} \geq 10\ L$$

which still maintains that the Hart model works for high dislocation densities, though the condition implied is less restrictive. For lower dislocation densities modifications were developed by assuming that the transport down and out of the dislocations was equivalent to that of a grain boundary[37,73] or by modeling of solutions that consider diffusion in and out of individual dislocations[74-76].

Strain effects on ΔG^* for intragrain nucleation has been modeled by considering that the strain energy (ΔG_d) of the dislocation favors nucleation on the dislocation, rather than at a random location within the matrix. The value of ΔG^* for precipitation on a dislocation is given by considering an energy balance between the chemical driving force for

nucleation ΔG_v, ΔG_d and energy required to create a new surface (ΔG_s)

$$\Delta G = - A \Delta G_d + A \Delta G_s - V \Delta G_v$$

and developing a solution for the equilibrium condition

$$d(\Delta G/dr) = 0$$

where r = nucleus radius

This method is similar to that for determination of ΔG^* for random (or homogeneous) nucleation[38] but was modified to consider the strain energy term.

Modeling deformation effects on grain boundaries requires modification of the solution to the energy balance equation for nucleation on grain boundaries. While the equilibrium solution for the grain boundary energy balance equation has been developed as

$$\Delta G^* = \frac{16\pi \Delta G_s^3}{3 \Delta G_v^2} K_j$$

for a variety of grain boundary nucleus shapes[77] through shape factor K_j (Figure 14), the methodology and solutions to account for the effects of strain on grain boundary precipitation reactions are not well established.

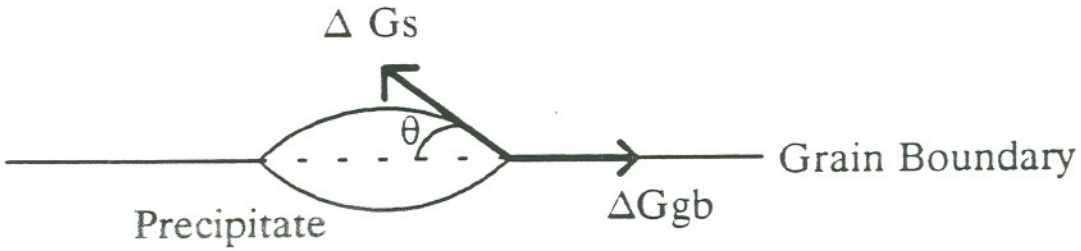

$$\text{Cos}\,\theta = \frac{\Delta Ggb}{2\Delta Gs}$$

$$Kj = \frac{2 - 3\,\text{Cos}\theta + \text{Cos}^3\theta}{2}$$

Figure 14. Shape and shape factor (K_j) values for nucleation of simplest precipitate shape on grain boundary[77].

Deformation Effects on Sensitization Modeling

While the development of GBCD in SS has been modeled by numerous researchers[56-59,63,65,66,78-85], the phenomena of deformation effects on GBCD has only been empirically estimated in the model developed by Bruemmer[56,82]. This model predicts strain effects on sensitization by empirically modifying chromium diffusivity to fit a database developed to evaluate deformation effects on the phenomena. Although the empirical equations used in the Bruemmer model lacks a theoretical basis for modifying deformation kinetics and do not consider thermodynamic effects of strain, predictions of the data developed are reasonable, as seen in Figure 15.

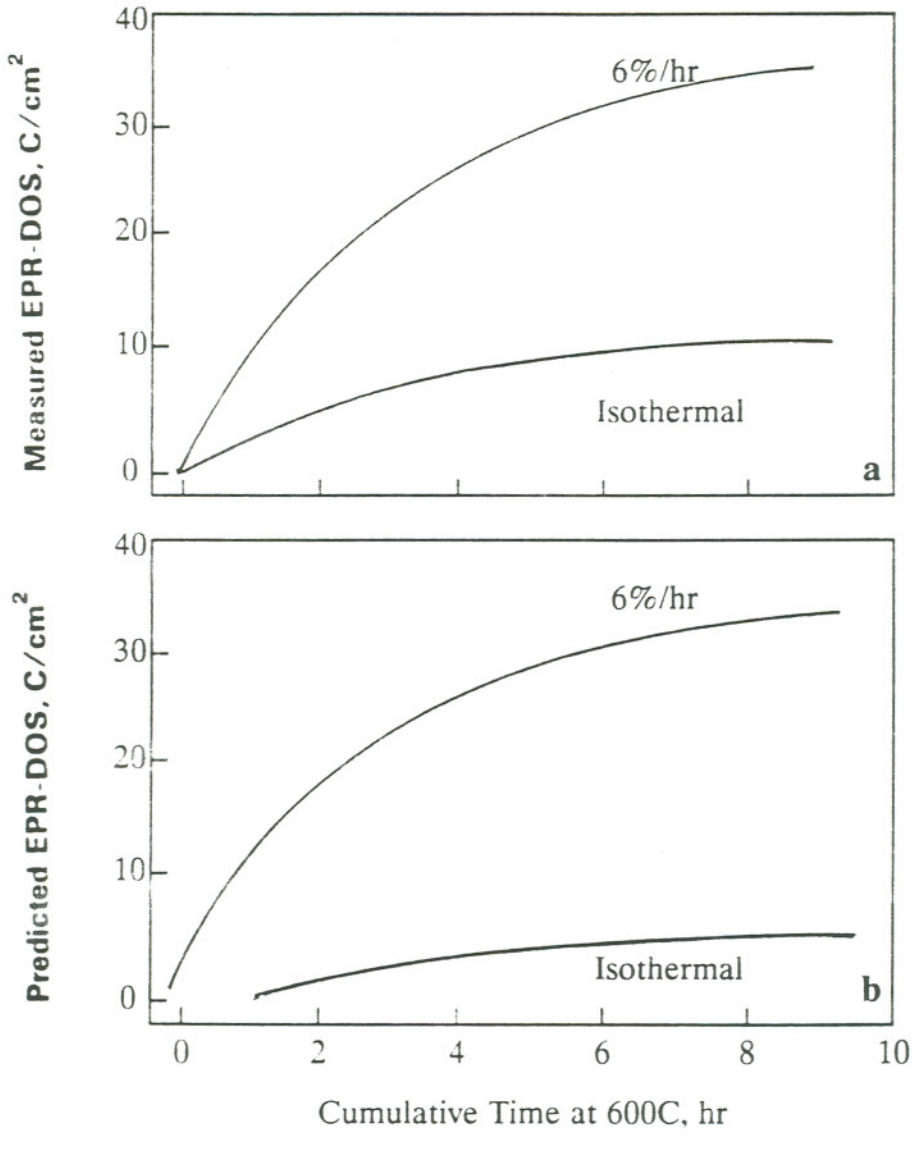

Figure 15. Comparison of deformation effects on sensitization as measured (a) and predicted (b) by Bruemmer[56].

CHAPTER 2

EXPERIMENTAL TECHNIQUES

EXPERIMENTAL METHOD

The method used to study deformation effects on GBCD in SS involved the following sequence of experiments:

1) Ambient temperature straining to induce strains from 0 - 40% ϵ in SS
2) Isothermal treatment from 550°C to 800°C to induce carbide precipitation and GBCD development on strained specimens.
3) GBCD measurement on strained and isothermally treated specimens.

These experiments critically evaluate strain magnitude and temperature effects on GBCD development in SS. Additional experimental methods used to examine deformation microstructures and measure grain size in SS are also presented.

AMBIENT TEMPERATURE DEFORMATION

Deformation was carried out through uniaxial tensile testing of samples machined from SS pipe. Two specimen configurations, termed variable strain tensile (VST) and constant strain tensile (CST) specimens (Figure 16), were loaded on a 50 kg-f Instron universal testing machine (Figure 17) and pulled in tension. Strains produced by the deformation process were measured as true strain values and given by

$$\epsilon = \log_e(A/A_o)$$

where A and A_o are the initial and final cross section areas at known locations on the specimen before and after tensile testing. Strains were varied in the range of 0 - 40% to allow comparison of strain magnitude effects on GBCD development.

Dimension, mm	Sample D2	Sample D3
Length	300	300
Gage	180	180
Width1	33.2	42.0
Width2	15.3	21.0
Tapered Section	200	200
Hole Diameter	12.5	12.5
Thickness	6.3	6.3

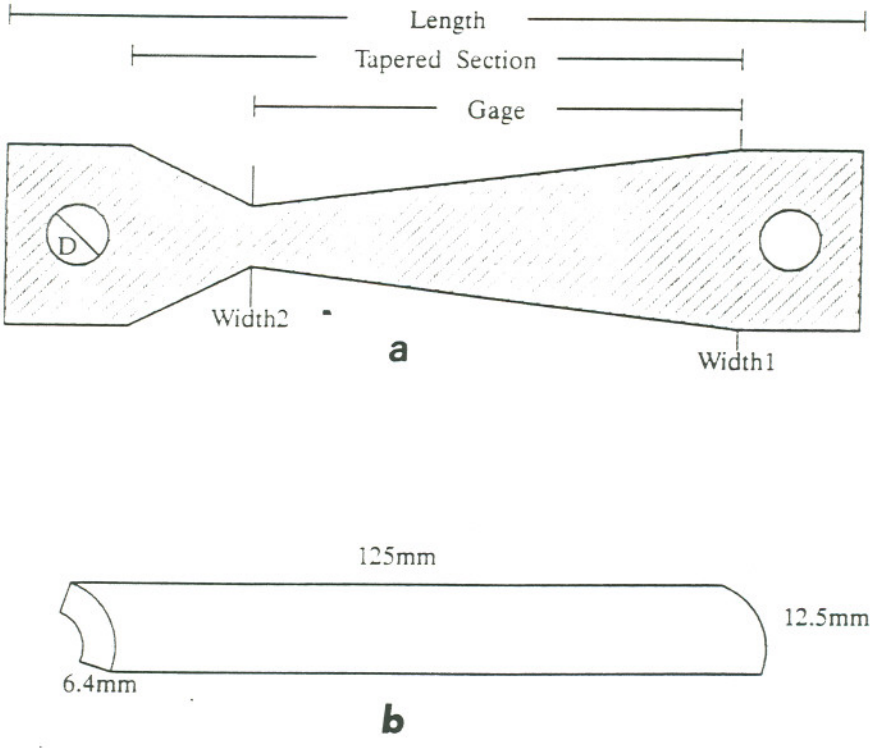

Figure 16. Specimen configurations of variable strain (a) and constant strain tensile specimens (b) used during deformation testing of SS.

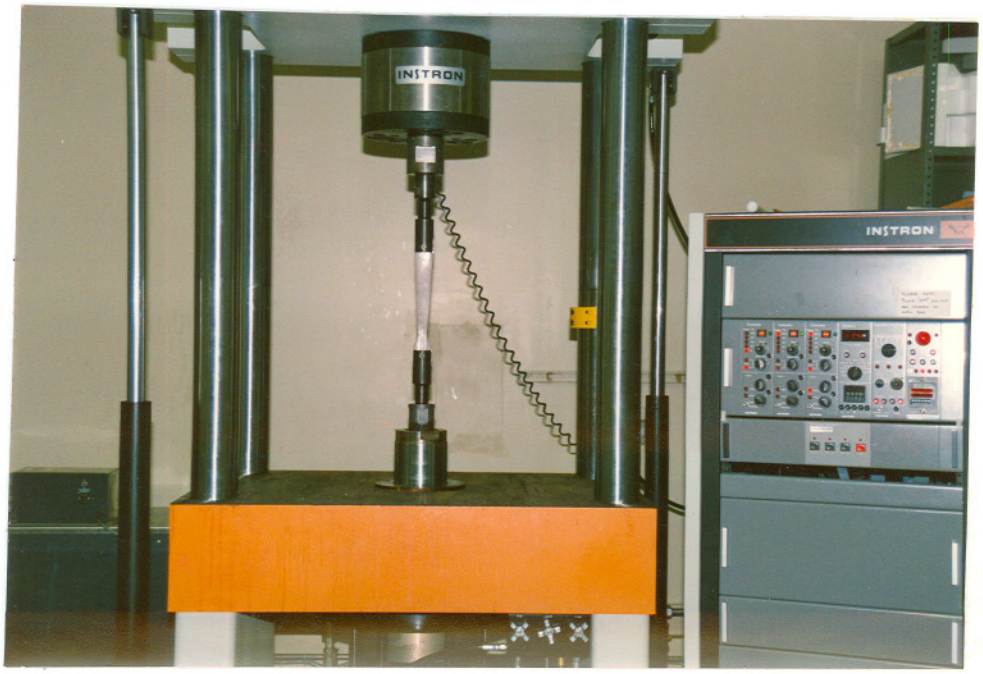

Figure 17. Photograph showing details of 50 kg-f Instron universal testing machine used for deformation testing.

The VST specimen produced a variation in strain along the tapered gage section, as illustrated by the data of Figure 18. This variation was anticipated considering the variable gage width present along the gage length of the sample. The strain-gage length data was seen to be non-linear, rising by small amounts at low strain values (typically < 1%/cm at 5% strain), and increasing more rapidly at larger strain values (typically 2%/cm at 20% strain level). Strains varying from 3 - 40% were obtained on tensile straining of VST sample D2, while strains of 2 -26% were obtained from VST sample D3. Specific sample coupons with strain values in the vicinity of 2, 6, 10, 16 and 25% were used to separate the effects of various strain levels on the sensitization phenomena.

The CST samples were pulled in tension to give constant strain coupons within +/- 25mm of the sample center. A variety of strain samples also in the range of 0 - 25% were produced by testing the CST to different peak load values. Coupons corresponding to 2, 6, 10, 16 and 25% were again selected among the various specimens available, to match strain values obtained in the CST and VST specimens.

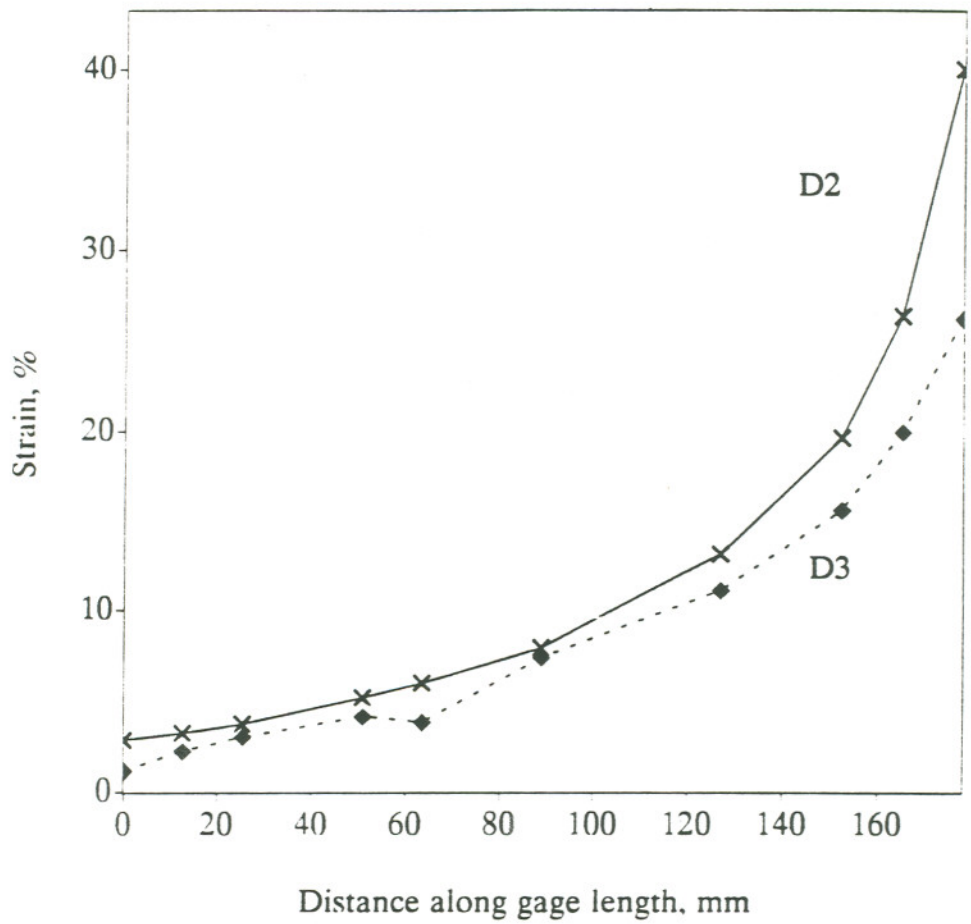

Figure 18. Plot of variation of strain along gage length for variable strain tensile specimens D2 and D3.

ISOTHERMAL HEAT TREATMENT

Isothermal treatment of strain coupons was carried out using a Lucifer box furnace (Figure 19). These heat treatments were done at temperatures in the range of 550°C - 800°C for 0.1 to 500 hours to compare temperature-time effects on strain-induced sensitization development in SS.

Isothermal treatments were carried out in additive steps. Specimens were placed in the furnace for a desired period of time at the required treatment temperature, quenched and used for GBCD measurements. The specimens were again placed in the furnace, heat treated for additional time, quenched and retested. The procedure was repeated until a desired cumulative heat treatment time was achieved for a particular treatment temperature.

Figure 19. Photographic illustration of Lucifer box furnace used for sample isothermal treatments.

MEASUREMENT OF GRAIN BOUNDARY CHROMIUM DEPLETION

Measurement of GBCD required usage of a method that is

* sensitive to the depletion phenomena
* reliable and quantitative

The indirect, single loop electrochemical potentiokinetic reactivation (EPR) test method[86,87] was selected to quantify GBCD development. Transmission electron microscopy was also used to examine carbide microstructures in selected sensitized samples to support the EPR test observations.

EPR MEASUREMENTS OF GBCD

The EPR test is a simple, indirect method for investigating the GBCD susceptibility of Types 304 and 316 austenitic SS. This electrochemical technique provides a reliable, quantitative measurement on the degree of sensitization (DOS) of SS. Measured EPRDOS values can also be directly correlated to the severity of chromium depletion existing at the grain boundaries.

Samples used in EPR testing were typically 1.25cm x 1.25 cm strained and heat treated blanks of SS pipe. These were threaded to a SS screw and mounted in an acrylic medium, polished to 1 μm diamond finish, and masked at a desired location for use as the working electrode in the EPR test (Figure 20a,b). Reference and counter electrodes used during the electrochemical test were saturated calomel (SCE) and graphite electrodes respectively. The electrolyte employed was a 0.5M H_2SO_4 + 0.01M KSCN aqueous solution held at 30 ± 1°C for testing.

The EPR test consisted of a sequence of operations which resulted in the determination of DOS for SS. The steps basically involved measurement of the corrosion potential

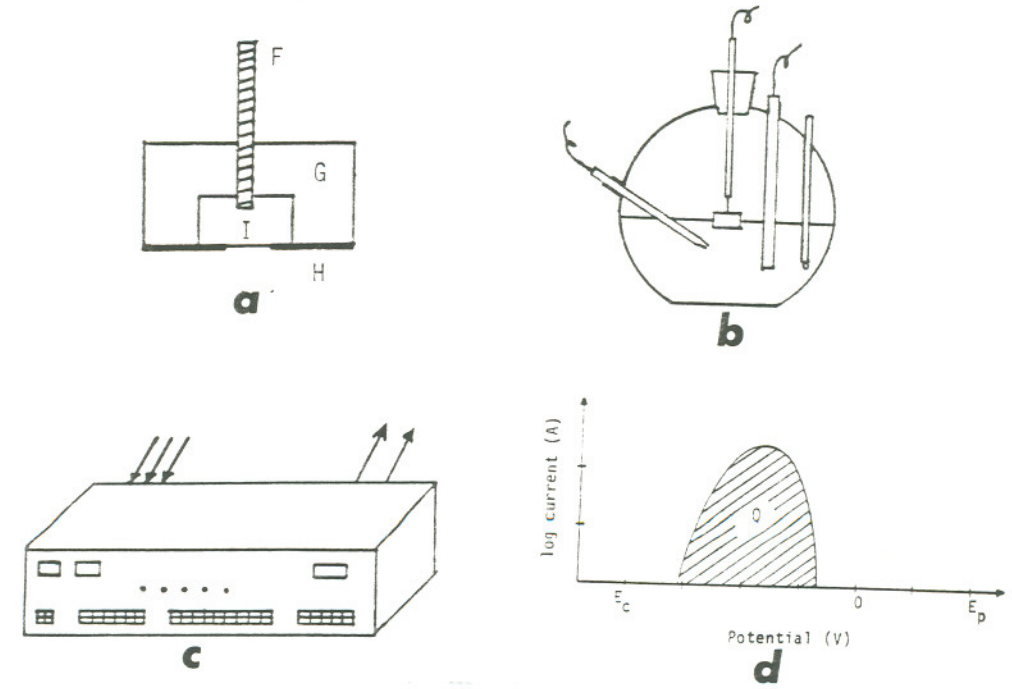

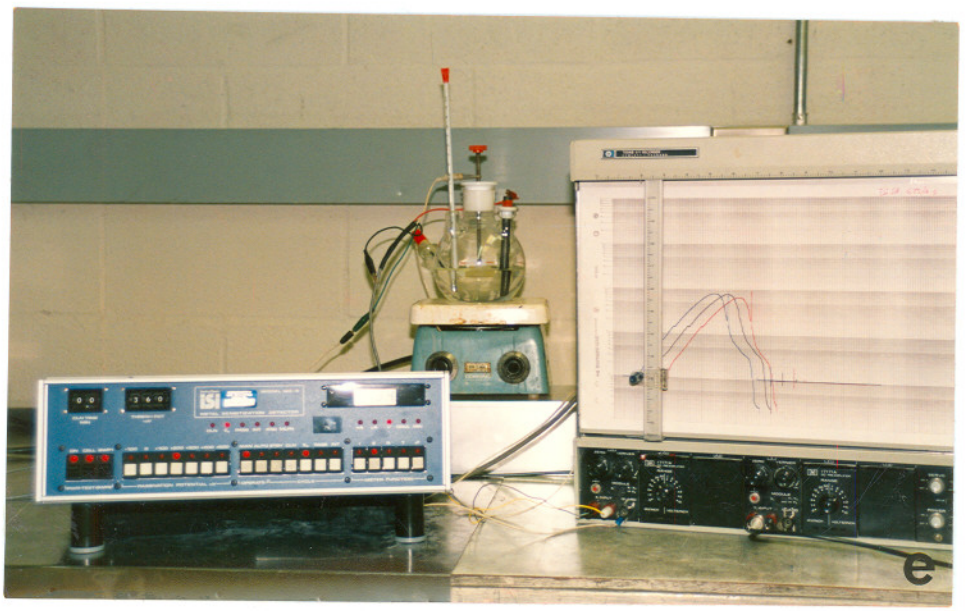

Figure 20. Electrochemical Potentiokinetic Reactivation test set up illustrating sample configuration (a), Corrosion Cell (b), model ISI Model WC-5 Potentiostat (c), typical chart record (d) and overall set up (e) for sensitization testing.

(E_c), passivation of the sample (E_p) and integration of the area under the current-time curve (Q) during a reactivation scan (E_p --> E_c), as shown in Figure 20c. This sequence of steps was performed automatically using an ISI model WC-5 metal sensitization detector (Figure 20d). Specific experimental and electrochemical parameters used in the EPR test for samples in this work are summarized in Table 1, while the entire set up is shown in the photograph of Figure 20e.

Table 1. Electrochemical Potentiokinetic Reactivation test parameters for Type 316 stainless steel

Sample :	1μ diamond polish
Mask Area :	0.6 cm^2
Electrolyte :	0.5M H_2SO_4 + 0.01M KSCN
Test Temperature :	30 ± 1°C
Corrosion Potential :	- 0.350V
Passivation Conditions :	0.20 V for 2 mins
Reactivation Scan Rate :	3 V/hr

The DOS of the SS was quantified by normalizing the reactivation peak area (Q) with the grain boundary area (GBA) using the relationship[86,87]

EPRDOS = Q/GBA in coulombs/sqcm (C/cm^2)

where Q = charge measured on the current integrating instrument

GBA = 5.1×10^{-3} A $exp^{0.35G}$

and A = Mask Area (cm^2)

G = ASTM grain size number at 100X

Metallographic examination of EPR test surfaces was also carried out using a Nikon optical metallograph at a magnification of 100X. This was used to qualitatively relate the quantitative EPRDOS values to the microstructures produced during EPR test attack.

EPRDOS values were related to STEM-EDS measurements of GBCD through the correlation

$$EPRDOS = 1.1\ VP - 6.1 \times 10^{-3}\ VP^2 + 1.1 \times 10^{-5}\ VP^3$$

where VP is the (normalized) volume parameter representing the region of GBCD below a critical level of chromium required for attack (Cr_{atk}) in the EPR test and is given by

$$VP = \frac{(Cr_{atk} - Cr_{min})\ W_{cr}}{2\ Cr_{atk}}$$

These relationships have been developed by Bruemmer[56,85] assuming that attack in the EPR test occurs for Cr_{min} values below assumed Cr_{atk} value of 13.5%.

TEM EXAMINATION OF CARBIDE PRECIPITATION

TEM was used to support the EPR test results through qualitative examination of carbide precipitate sizes and densities at the grain interface for selected specimens.

Slices typically 300 μm thick were cut from the specimen using a slow speed cut-off saw with a cubic boron nitride cut-off wheel. The slice was mounted on a support and wet ground on 240 grit through 600 grit silicon carbide papers until the sample thickness was approximately 150 to 200 μm. Squares of side 3 mm were cut from the thin foil and mechanically dimpled on both sides. This facilitated uniform sample thinning and formation of a centrally located hole during subsequent electropolishing, which was carried out using a twin jet polishing system. The electrolyte used for electropolishing was 5% $HClO_4$ in methanol at -35°C while current and voltage conditions used for polishing SS were typically 80-90 mA and 100-120 V, respectively. Thin foils prepared above were examined using the Hitachi H-800 STEM employed in the conventional TEM (C-TEM) mode.

EXAMINATION OF DEFORMATION MICROSTRUCTURE

MATRIX DISLOCATION DENSITY MEASUREMENT

The experimental procedure used for estimating dislocation density in SS was a two-step procedure, which first required documentation of the dislocation structure in thin foils using TEM and analyzing the micrographs to yield the dislocation density.

To document the dislocation structure in the TEM

1) The sample was tilted to the [110] orientation.
2) A (111) two-beam condition with deviation parameter s slightly positive was then obtained.
3) A bright field image of the dislocations was documented.
4) The number of thickness fringes (n) leading to the location at which dislocation structure was obtained was also noted.

Micrographs of the dislocation structure were analyzed by measuring the total length of dislocation line in a unit volume of crystal, as given by Hirsch[88]. A grid of length 110 cm was placed on the micrograph and the number of dislocation

intersections with the grid N were counted. The dislocation density was then computed using

$$d = \frac{2N}{Lt}$$

where L = length of grid/Micrograph Magnification(X)
= 110/X
t = thickness of foil = $n \epsilon_g$

and ϵ_g = dynamical extinction distance
= 324[89] for g = (111) at 200KV accelerating potential

It should be noted that all measurements of dislocation density were carried out at the [110] pole with a fixed g reflection of (111) to provide the advantage of comparing dislocation densities under identical diffraction conditions. Absence of a statistical analysis of dislocation densities, however, suggests that numerical values obtained in this work are only an approximate estimate of dislocation density.[88]

ANALYSIS OF DISLOCATION DENSITIES AROUND TWIN BOUNDARIES

Dislocation density in the vicinity of twin boundaries was documented by photographing the TEM image near the twin interface at the [110] pole with g = (111) and s slightly positive (similar to matrix dislocation density measurement). This, as mentioned above, had the advantage of comparisons of dislocation density under identical diffraction conditions. Only qualitative analysis of dislocation densities near the interface was, however, carried out.

GRAIN SIZE MEASUREMENT IN SS

Grain size in specimens was estimated using the Abrams procedure recommended in ASTM E112-85[90]. Samples of SS electrolytically etched with 60% Nitric Acid at 1.2V DC (ideal for grain boundary etching in SS[91]) were photographed at 50X - 100X using a Nikon optical metallograph. A three circle grid of length 500 cm was placed on the micrograph and number of intersections between the grain interfaces and grid were documented. The grain size was then computed using charts of ASTM grain size versus number of intersections drawn at different magnifications in the ASTM E112-85 procedure sheet.

CHAPTER 3

MATERIAL ANNEAL CONDITION EFFECTS ON GRAIN BOUNDARY CHROMIUM DEPLETION

TASK ANALYSIS

This task examined the effect of prior solution annealing (SA) on microstructural development and isothermal sensitization behavior of SS. The work resulted in a selection of a suitable initial material condition for examining deformation effects on sensitization of SS.

STAINLESS STEEL COMPOSITION

The SS used in this investigation was a high carbon (C) type 316 SS of composition given in Table 2.

TABLE 2. Chemical Composition of high Carbon 316SS

Alloying Element Composition, wt%									
C	Cr	Ni	Mo	Mn	Si	P	S	N	B
0.058	17.11	11.43	2.16	1.77	0.41	0.014	0.005	0.008	0.002

The heat was obtained as a 10 cm inside diameter seamless pipe with a wall thickness of 0.62 cm.

A high C grade of 316 SS was preferred to a low C grade as it allows usage of

* shorter aging time schedules and
* wider range of temperatures

for examining deformation effects on DOS in Type 316 SS[56].

MATERIAL ANNEAL CONDITIONS

The heat of Type 316 SS was received in the mill processed (MP) condition. Specifications received with the piping indicated that the MP treatment consisted of annealing the SS at 1100°C for 5 minutes, followed by rapid cooling. No further information on the deformation history and cooling rate was available, as is the case for most commercially purchased products.

Solution annealing of the MP material was carried out in the range of 1000°C - 1100C for times varying from 0.5 to 4 hrs. Specific temperature and time schedules used for the annealing treatments are summarized in table 3. Materials treated at 1000°C, 1050°C and 1100°C have been termed SA1000, SA1050 and SA1100 respectively.

Table 3. Temperature and time conditions employed for solution annealing 316 SS

Material Anneal Condition	Solution Annealing Treatment	
	Temperature °C	Time, hr
SA1000	1000	0.5,1.0,1.5
SA1050	1050	0.5,1.0,1.5,4
SA1100	1100	0.5,0.75,1.0, 1.25,1.5,2,2.5

MICROSTRUCTURAL CHARACTERIZATION OF MATERIAL CONDITIONS

MILL PROCESSED MATERIAL MICROSTRUCTURE

The MP material had a relatively fine grain size with a uniform distribution. This uniformity was observed both on the outer surface and through-thickness of the pipe section, and appears as shown in the micrographs of Figure 21. Grains were noted to be equiaxed and did not show any evidence of the deformation produced during the mill TM treatment. Grain size of the MP samples was measured to be approximately 50 μm.

The extent of matrix and grain boundary deformation of the MP material was observed to be low in the TEM. Only isolated dislocations (density $\approx$ 6 x $10^7/cm^2$) were visible in the matrix or in the vicinity of twin and grain boundaries of the material (Figure 22a,b,c). No second phase particles (eg. carbide precipitates) were seen on twin and grain interfaces of the material.

An isolated observation made during TEM of the MP samples was the presence of an extremely small grain of size 0.25 μm (Figure 22d). This grain was, in fact, so small that it initially appeared to be a second phase particle on the grain

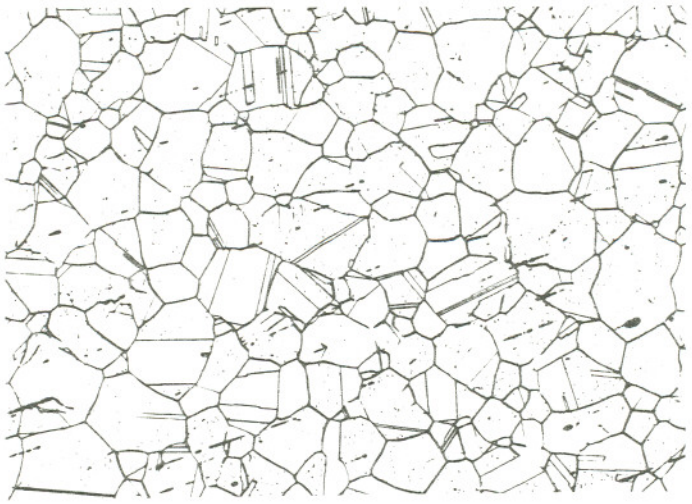

(a)

100 μm

(b)

100 μm

Figure 21. Optical micrographs illustrating the uniform, fine grain size on the mill processed material for samples obtained on the outer surface (a) and through thickness (b) of the pipe section. Microstructures were obtained through electroetching of polished stainless steel surfaces with 60% Nitric acid at 1.2V.

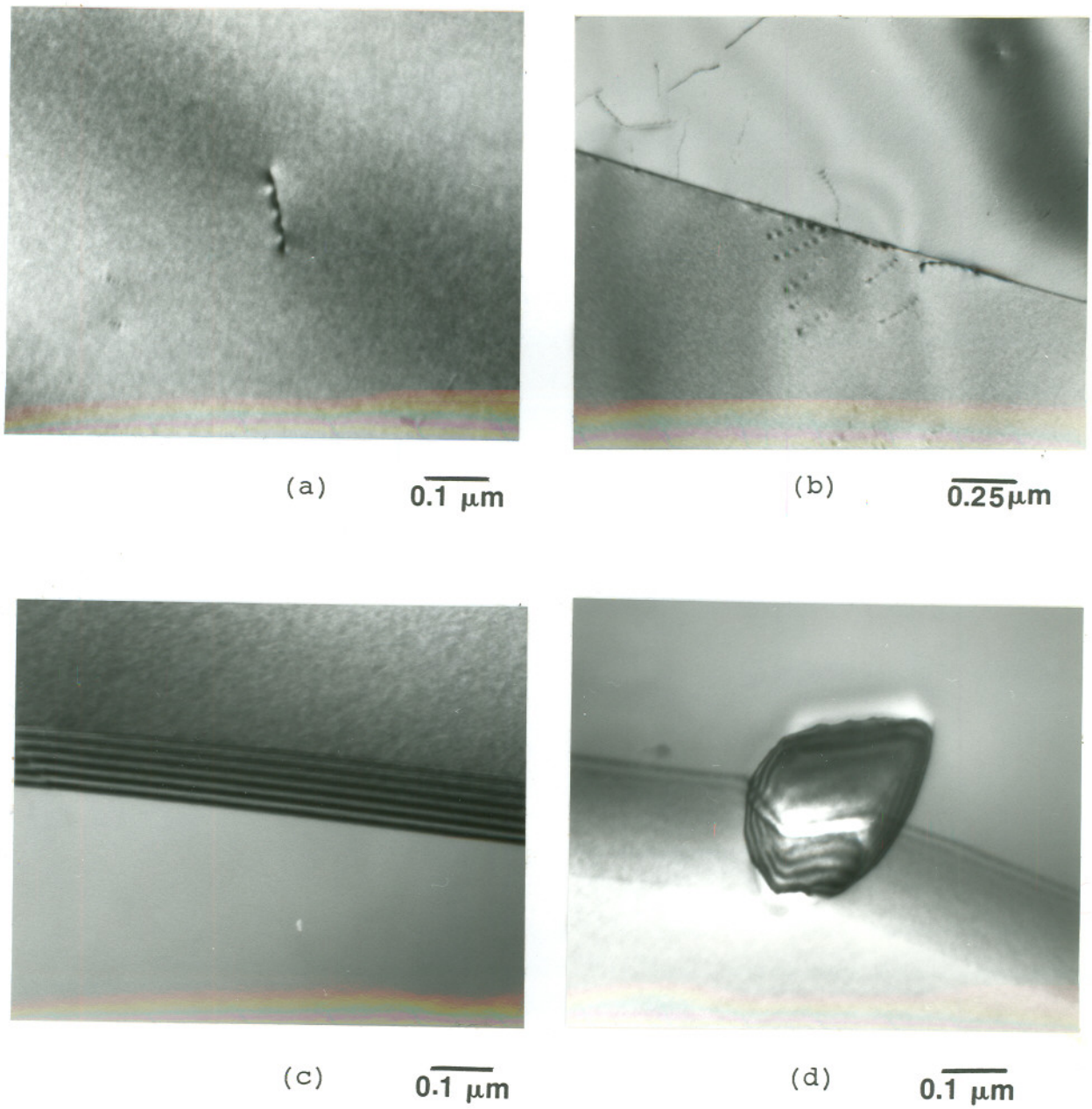

Figure 22. Transmission electron micrographs documenting the dislocation density levels in the matrix (a), twin boundary (b) and grain boundary (c). Also noted is the absence of carbides on the twin and grain interfaces and presence of an extremely small grain in the material(d).

boundary. Tilting and diffraction analysis carried out on the sample, however, verified that the observed microconstituent was a grain, rather than a second phase particle.

SOLUTION ANNEALING EFFECTS ON MICROSTRUCTURAL DEVELOPMENT

Grain size was determined to be dependent on the solution heat treatment temperatures and times employed to anneal the MP material. This dependence is shown in a plot of grain size versus SA time and temperature (Figure 23). Optical micrographs showing grain size development in selected annealed conditions are shown in Figure 24.

The figures 23 and 24 illustrate that SA1000 specimens have a uniform grain size of 50 μm similar to that observed in the MP material. This indicates that annealing at 1000°C for less than 1.5 hours does not induce any significant grain growth.

Distinct grain size increases are seen in the data at 1050°C. Average grain diameters varied from 50 μm to 150 μm during 4 hours of annealing at this temperature. Optical observations on SA1050 specimens heat treated for less than 1.5 hours, however, alluded to the presence of a dual grain size distribution in these specimens. The dual grain structure contained clusters of MP size grains at some locations and significantly larger grains 3 to 4 times the size of MP grains

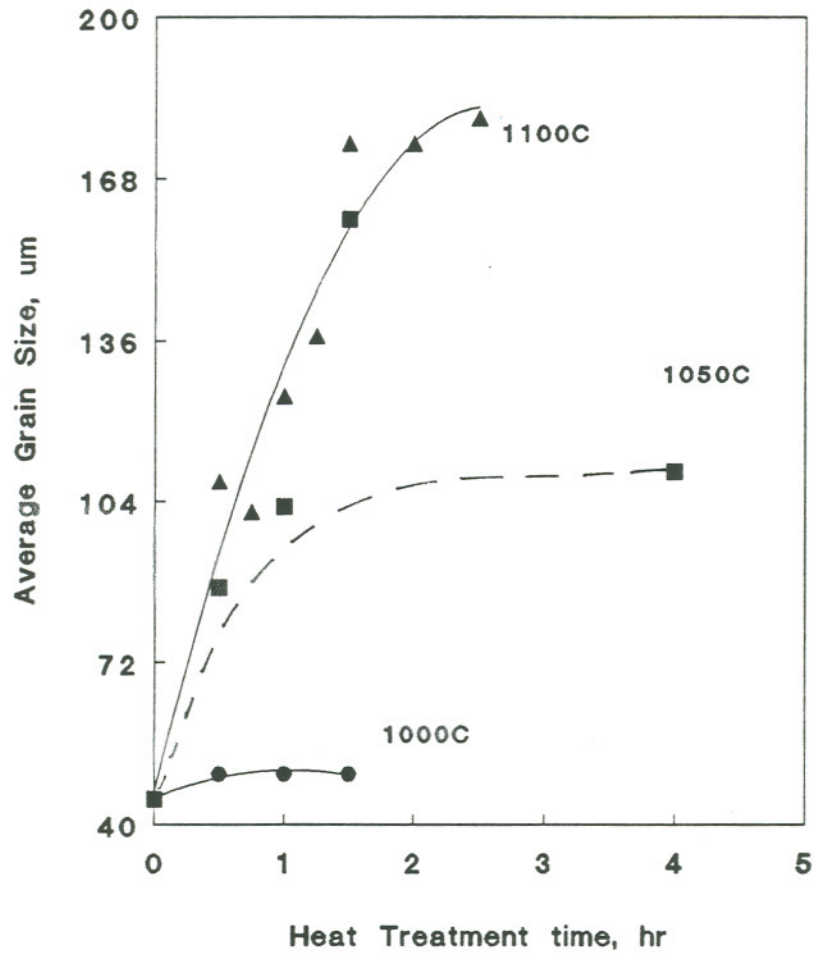

Figure 23. Solution annealing heat treatment effects on grain size development in Type 316 stainless steel.

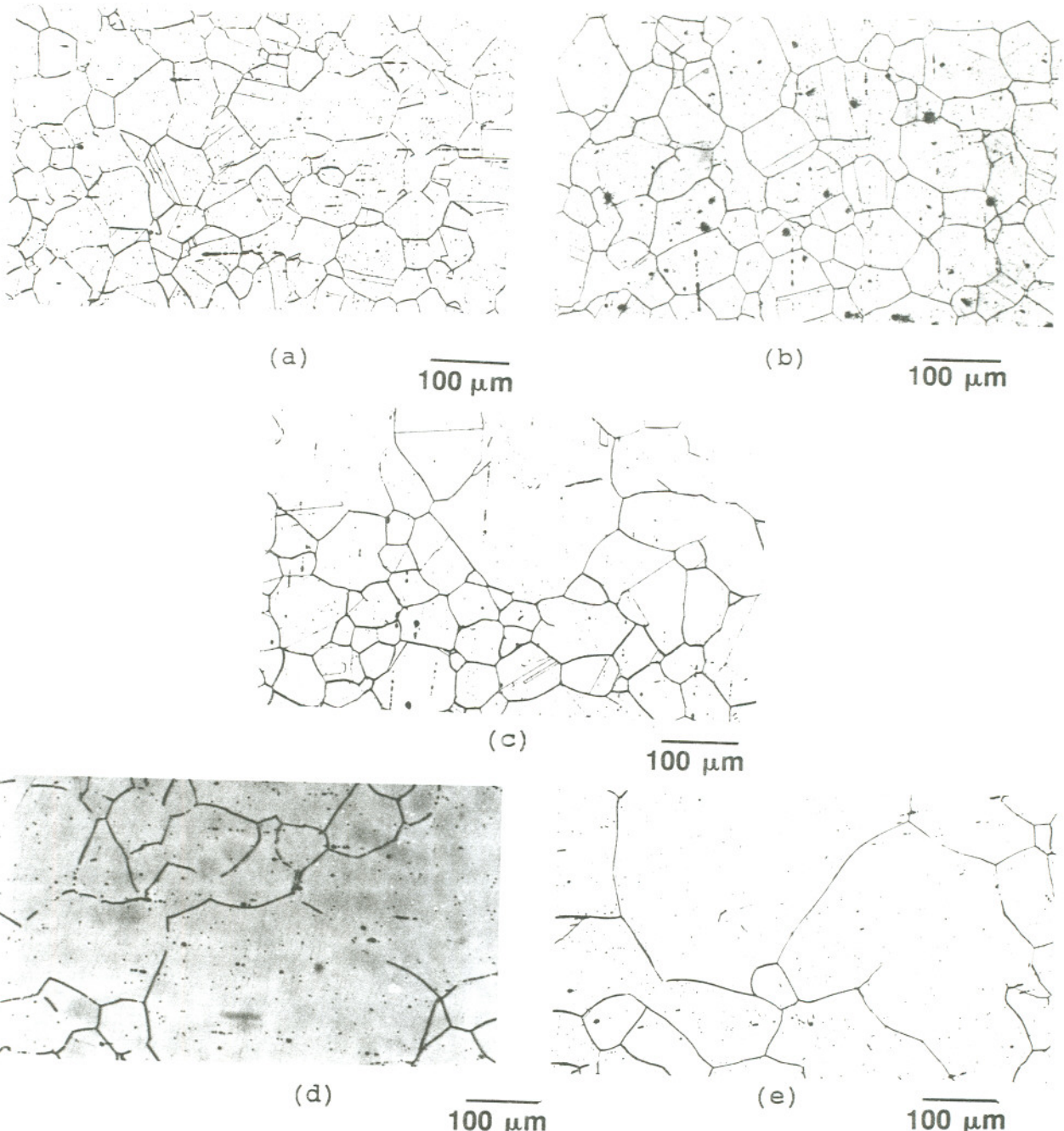

Figure 24. Optical micrographs depicting grain size distribution in specimens solution annealed at 1000°C for 1 hr (a), 1050°C for 0.5 hr (b), 1 hr (c) and 4 hrs (d) and 1100°C for 1 hr (e).

at other locations. The small grains in the mixed structure also slowly increased in size with increasing heat treatment and a uniform, large grain size material was observed after 4 hours of SA at 1050°C.

Heat treatment at 1100°C for times varying from 0.5 hours to 2.5 hours resulted in uniform grain growth even at the shortest treatment time of 0.5 hours. Grain sizes increased rapidly from 50 μm to 135 μm within 1 hour of annealing at 1100°C. Longer times of heat treatment, however, resulted in relatively slower grain growth at this temperature, and the largest grain diameter observed after a 1100°C - 2.5 hrs heat treatment was only 180 μm .

Transmission electron microscopy of matrix deformation in SA1000-1hr and SA1100-1hr samples revealed that these materials had low dislocation levels ($10^8/cm^2$ order), similar to that of the MP material (Figure 25a,b). Regions in the vicinity of twin boundaries also had low dislocation densities, though the presence of dislocation emission was seen at kinks on twin boundaries in the SA1100-1hr material (Figure 25c,d).

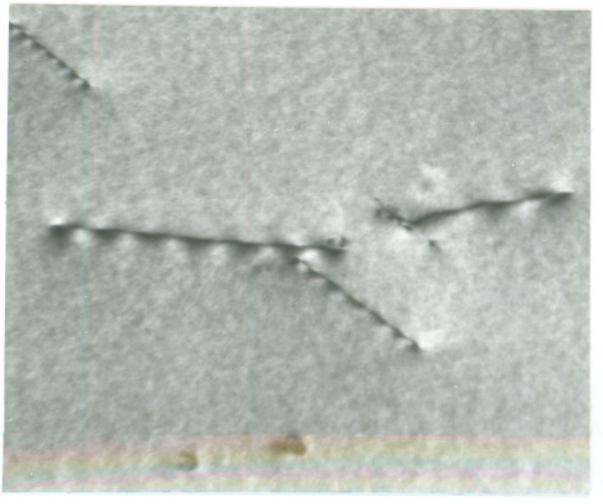

(a) 0.1 μm

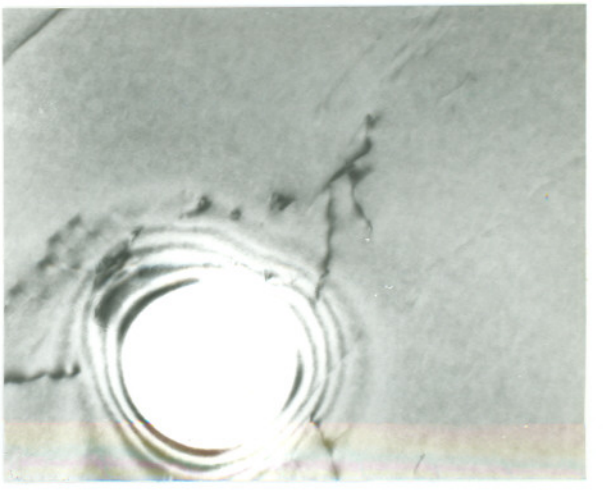

(b) 0.1 μm

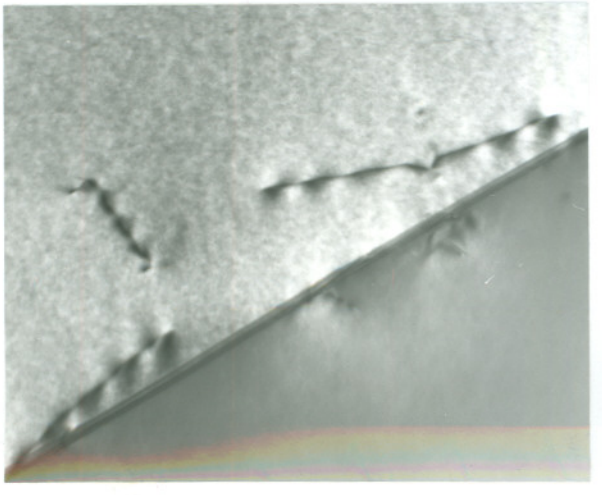

(c) 0.1 μm

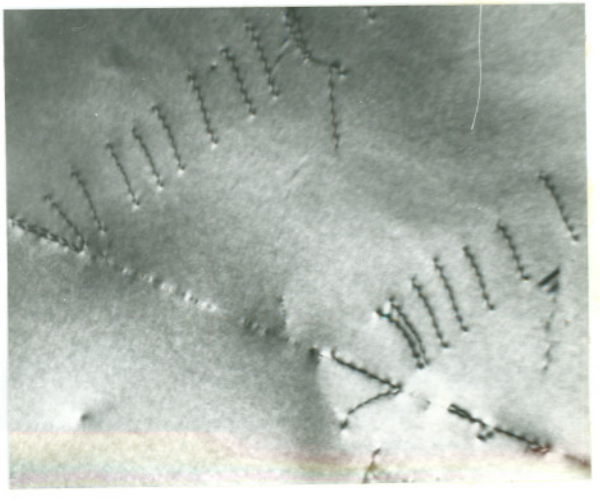

(d) 0.25 μm

Figure 25. Transmission electron microscope micrographs documenting low deformation levels in the matrix (a,b) and around twin boundaries (c,d) in materials solution annealed for 1 hour at 1000°C and 1100°C respectively.

Observations of grain boundary carbide precipitation in certain SA specimens were different from that documented in the MP material. Carbide precipitation was seen in specimens annealed for 1 at 1000°C and 0.5 hr at 1050°C, in contradiction to that of the MP material. The 1100°C - 1 hr and 1050°C-1 hr samples, however, did not show any carbide precipitation and were, in this respect, similar to the MP sample.

Carbides seen in the SA1000-1 hr specimens had an uneven distribution. Selected boundaries were seen to have a large, continuous distribution of carbides at the interface (Figure 26 a,b). Other boundaries showed precipitation of blocky, irregular shaped carbides particularly at triple points, while the remaining grain boundary length showed no precipitation (Figure 26c).

Similar massive carbides were documented at isolated locations on grain boundaries of the SA1050-0.5 hr dual grain size specimen (Figure 27a). In addition, other grain interfaces in this specimen indicated the presence of additional spots (possibly due to carbides) on diffraction patterns taken in the grain boundary region (Figure 27b).

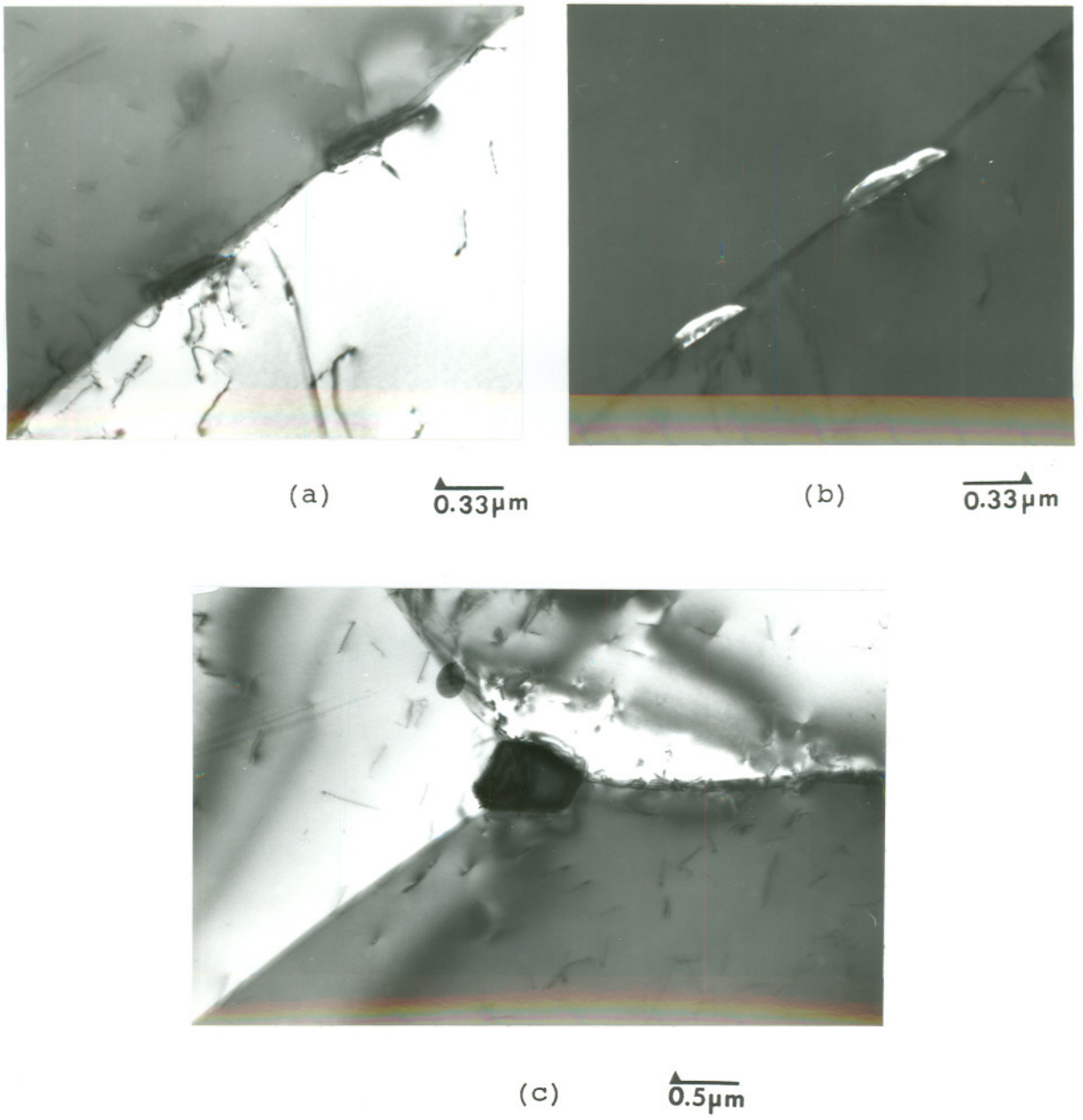

Figure 26. Transmission electron micrographs documenting continuous distribution of carbides on selected grain boundaries seen in the bright field (a) and dark field (b), and blocky, irregular carbide precipitation on triple points (c).

(a) 0.1 μm

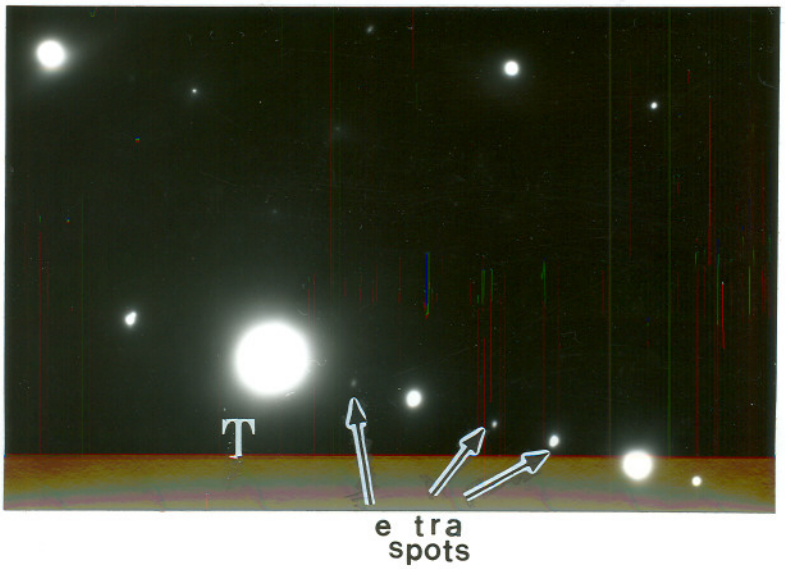

(b)

Figure 27. Bright field micrograph (a) and diffraction patterns (b) documenting formation of a massive carbide precipitate and unresolved second phase particles on grain boundaries in the 1050°C - 0.5 hour treated specimen.

Bright and dark field observations of these regions could not, however, resolve the presence of second phase constituents on the boundaries. This indicates that carbides, if present on these boundaries, were too small to be resolved clearly in the TEM.

Materials annealed at 1050°C for 1 hour and 1100°C for 1hr illustrated clean grain boundaries, with no carbides observed at any location in these samples (Figure 28).

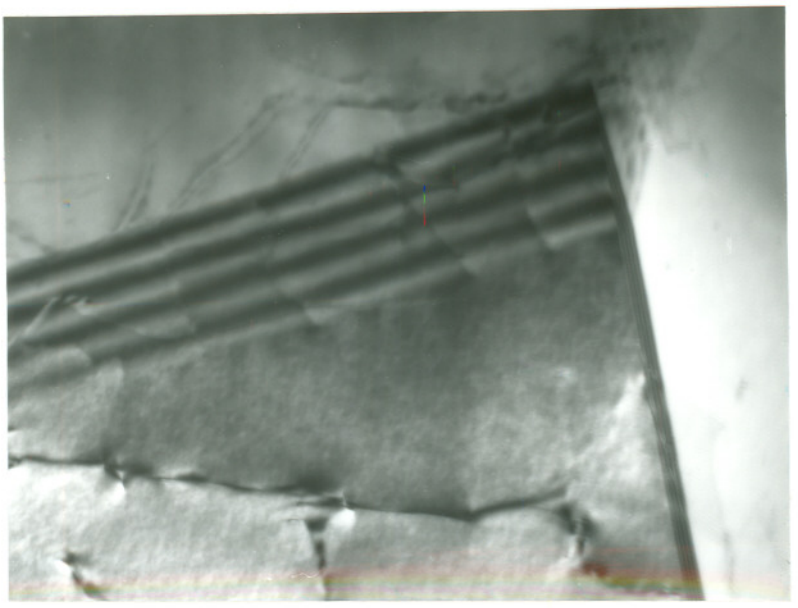

(a) 0.1 μm

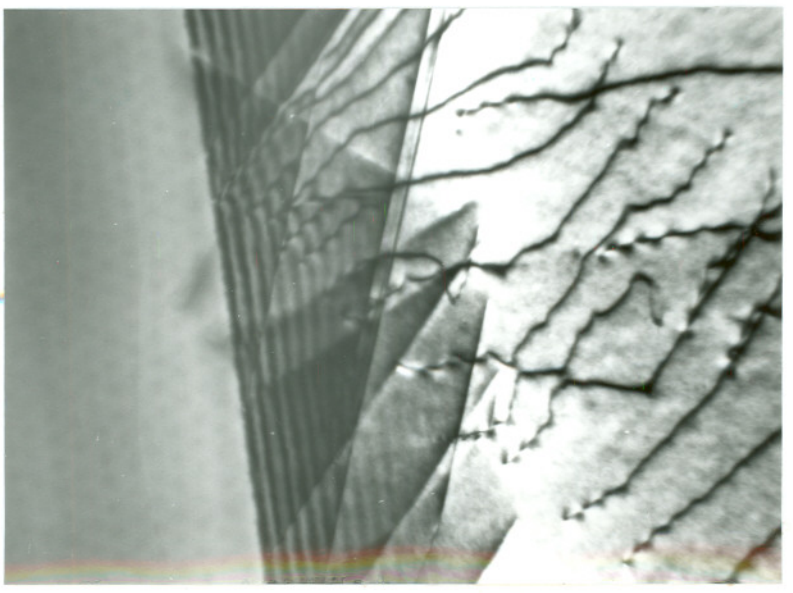

(b) 0.2 μm

Figure 28. Transmission electron micrographs documenting the presence of precipitate-free grain boundaries in samples annealed at 1050°C -1 hour and 1100°C - 1hr.

ISOTHERMAL GRAIN BOUNDARY CHROMIUM DEPLETION DEVELOPMENT

MILL PROCESSED MATERIAL SENSITIZATION DEVELOPMENT

Sensitization development of the MP material was measured as a function of heat treatment for temperatures ranging from 550 to 850°C and times varying from 0.05 to 100 hours. EPRDOS values obtained for isothermally treated specimens are plotted as a function of heat treatment time and temperature in Figure 29. Three principal patterns of sensitization behavior corresponding to low (550°C), intermediate (625°C, 670°C) and high temperatures (780°C, 850°C) were noted to be present in this plot.

Sensitization did not develop with isothermal heat treatment at low temperatures (550°C). This was noted when EPRDOS values were well below 5 C/cm^2 even after 100 hours of heat treatment at 550°C.

Significant increases in DOS with heat treatment were observed in the results obtained at 625°C and 670°C intermediate temperatures. Sensitization first developed after an initial incubation time of 10 to 25 hours at 625°C. EPRDOS then increased rapidly to approximately 5 C/cm^2 after 26-50 hours

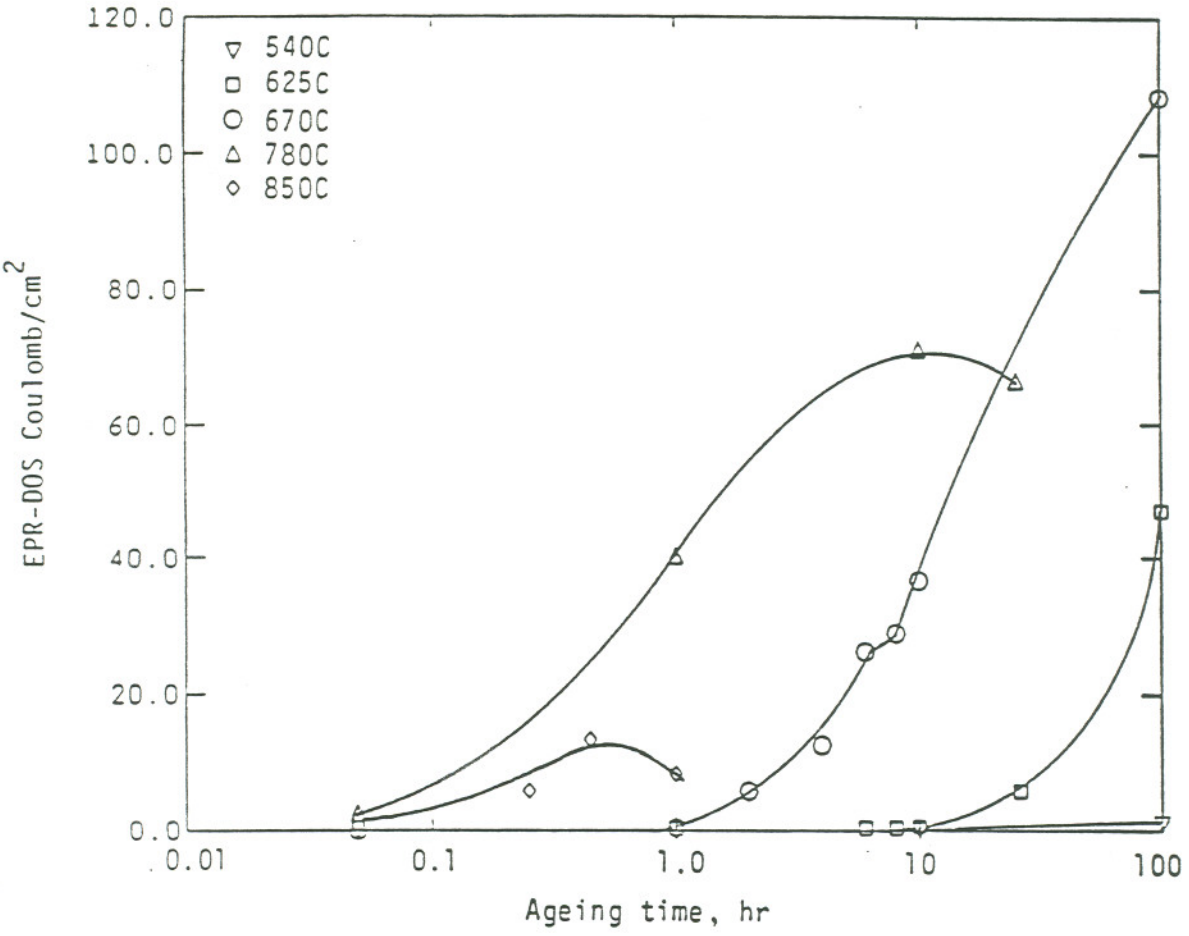

Figure 29. Isothermal sensitization behavior of mill processed Type 316 stainless steel portraying three patterns of behavior corresponding to low (550°C), intermediate (625°C, 670°C) and high (780°C, 850°C) temperatures.

and further to 50 C/cm^2 within 100 hours of treatment at this temperature. This is also illustrated through optical microscope comparisons of increases in grain boundary attack from 10 to 25 hours at 625°C (Figure 30). Similar trends were seen in the results for 670°C with the difference that sensitization occurred in shorter times and achieved higher EPRDOS values in equivalent treatment times at 670°C versus 625°C.

Sensitization occurred at shorter times, increased to a maximum at a faster rate, and then decreased with further heat treatment at higher temperatures due to desensitization (780°C, 850°C). The maximum EPRDOS value before the turn-over of the sensitization curve and duration of the entire sensitization cycle (from start to end) also decreased as the treatment temperature was raised from 780°C and 850°C.

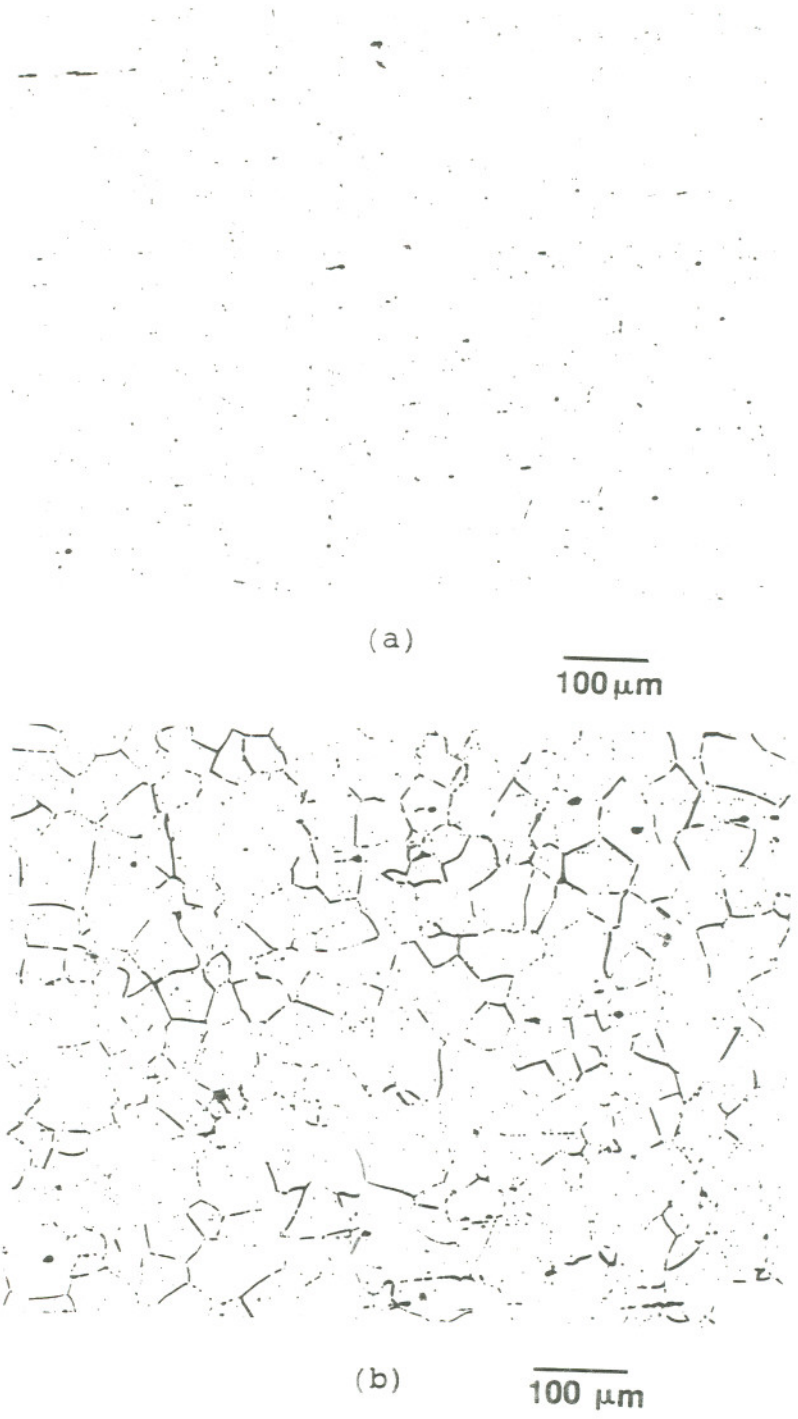

Figure 30. Optical micrographs illustrating increase in grain boundary attack for mill processed materials treated for 8 - 10 hrs (a) and 26 hours (b) at 625°C.

SOLUTION ANNEALING EFFECTS ON SENSITIZATION

Sensitization response of the SA1100-1hr material was studied in detail from 575°C - 775°C (Figure 31). EPRDOS values measured on these specimens illustrated that increasing heat treatment temperature from 575°C to 775°C resulted in shorter sensitization times and faster sensitization rates, as was observed in the MP material. Heat treatment effects on EPRDOS values of the SA1100 and MP samples were also comparable, as illustrated in Figure 32.

Degree of sensitization of SA1000-1hr and SA1050-0.5 hr and 1 hr samples were also examined after heat treatment at 625°C. Accelerated sensitization development was observed in all conditions as compared to that observed in the MP and SA1100-1hr specimens (Figure 33). EPRDOS values for the SA1000, SA1050-0.5, 1hr materials were, for example, above 3 to 4 C/cm^2 after 625°C - 8hrs and 20 C/cm^2 after 625C/26 hrs, while the MP and SA1100-1hr samples had EPRDOS values below 5 C/cm^2 after identical heat treatments.

This acceleration in EPRDOS values for the 1000°C-1hr and 1050°C-0.5, 1hr samples was corroborated through metallographic examination of EPR attack surfaces. Increased grain boundary attack was seen on the EPR test surfaces for

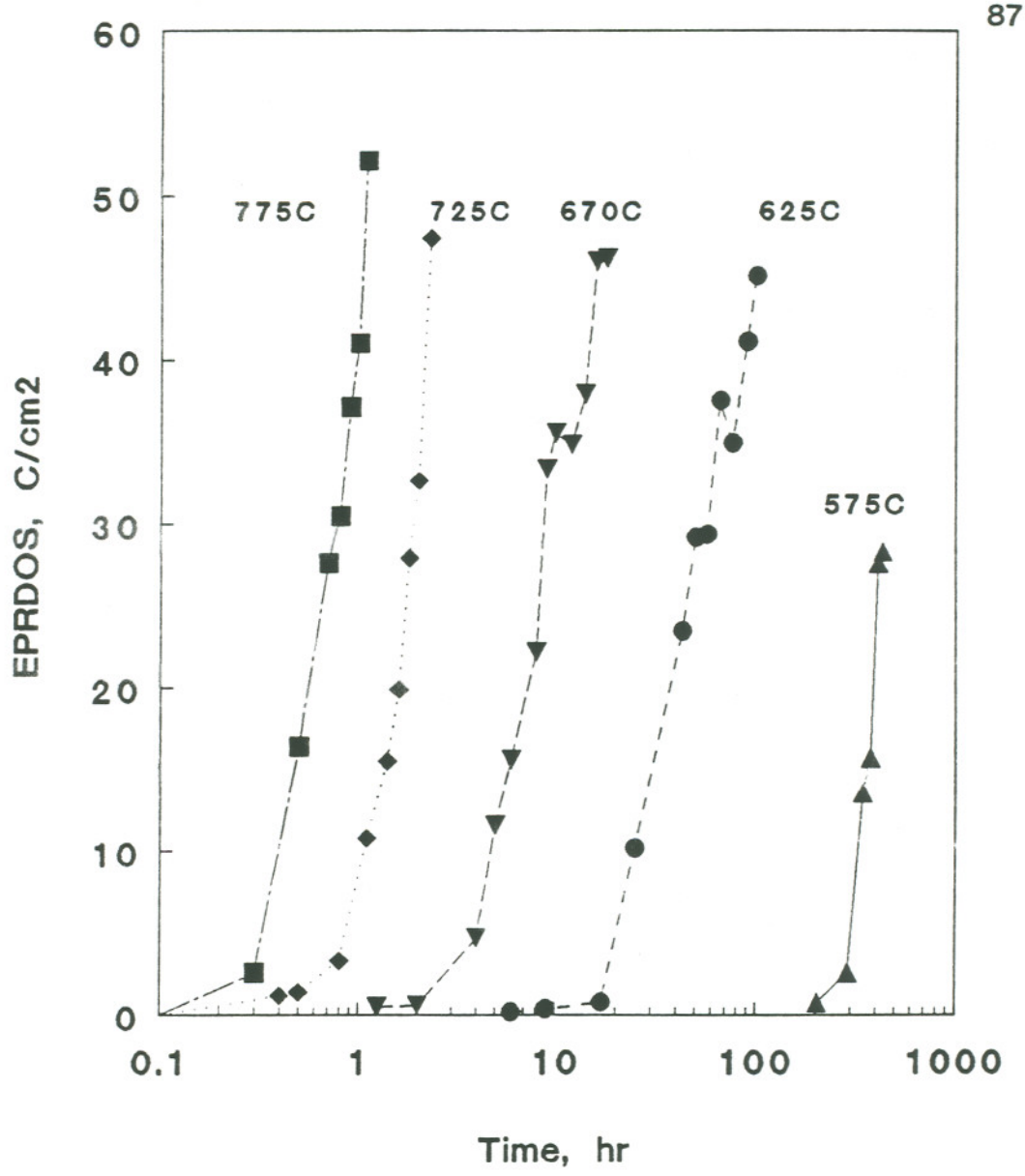

Figure 31. Sensitization development in the 1100°C - 1hr sample for treatments varying from 550°C to 800°C.

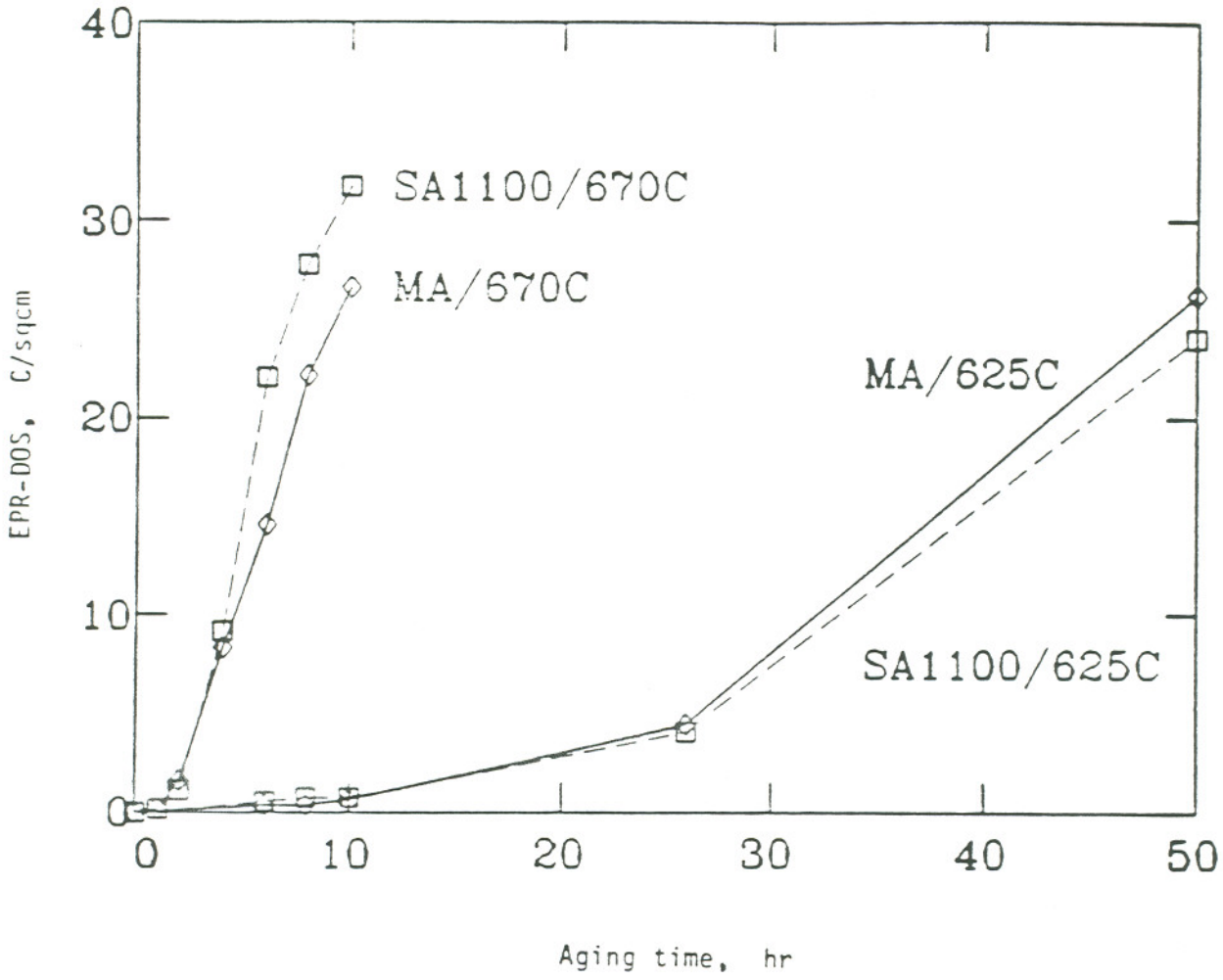

Figure 32. Comparison of EPRDOS values obtained during heat treatment of the mill processed and 1100°C - 1 hr solution annealed materials at 625°C and 670°C. The data indicates EPRDOS values of the two samples to be similar.

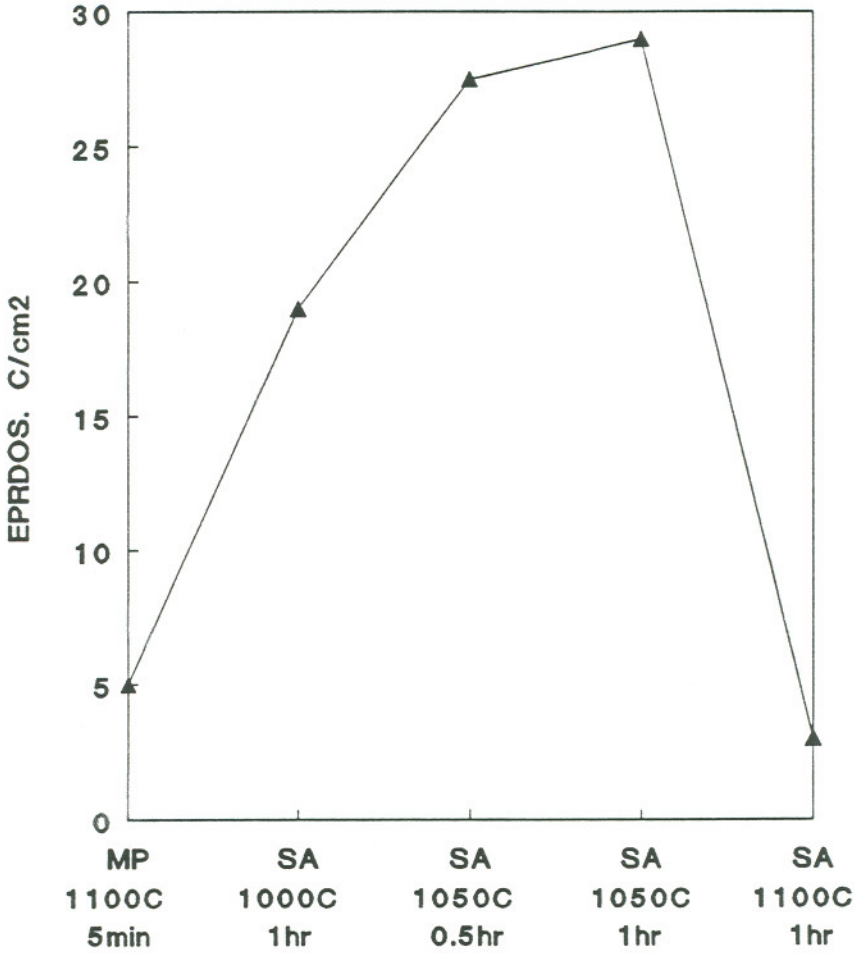

Figure 33. Comparison of sensitization development of solution annealed material conditions illustrating accelerated sensitization development in 1000°C-1hr,1050°C-0.5,1hr samples over mill processed and 1100°C-1hr samples.

the SA1000 and SA1050-0.5, 1hr treatments, as compared to the MP and SA1100-1hr and SA1050-4hr materials for 625C-26 hr heat treatments (Figure 34).

An additional interesting observation made after heat treating and sensitization testing of the SA1050 dual grain size materials was that the EPR test attack in these materials tended to concentrate on the small grains of the material. This is better portrayed in an optical micrograph for the SA1050-1hr sample heat treated at 625°C for 10 hrs (Figure 35).

The acceleration in sensitization was also confirmed by comparison of carbide densities after a 625°C-10 hr heat treatment of the SA1000-1hr, SA1100-1hr and MP materials, as shown in Figure 36. These micrographs clearly evidence the presence of a semi-continuous distribution of IG carbides on the SA1000 specimens after 10 hrs at 625°C versus isolated distribution of carbides for MP and SA1100 materials after the same heat treatment. Comparisons drawn after 26 hrs at 625°C did not, however, yield similar trends. This is because carbide densities in all materials appeared to be qualitatively similar. A statistical analysis was required to quantify the difference in carbide densities in these materials, but was not deemed necessary for this work.

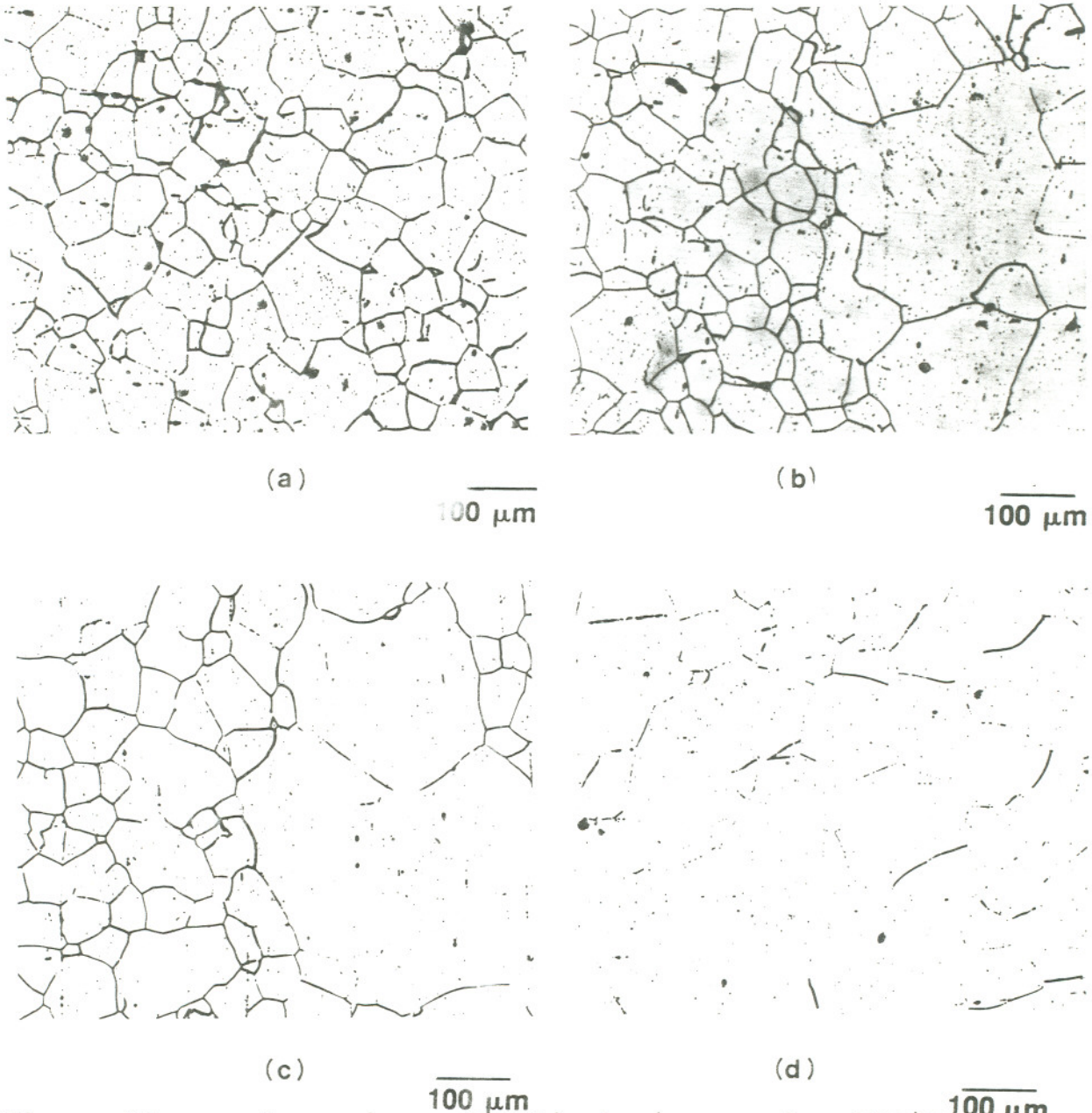

Figure 34. Comparison of optical micrographs obtained on EPR attack surfaces of 1000°C-1 hr (a), 1050°C-0.5hr (b), 1050°C-1hr (c) and 1100°C-1hr (d) specimens after heat treating at 625°C for 26 hours.

Figure 35. Illustration of favored EPR test attack on small grains of the dual grain size 1050°C-1hr treated samples after heat treating at 625°C for 10 hrs.

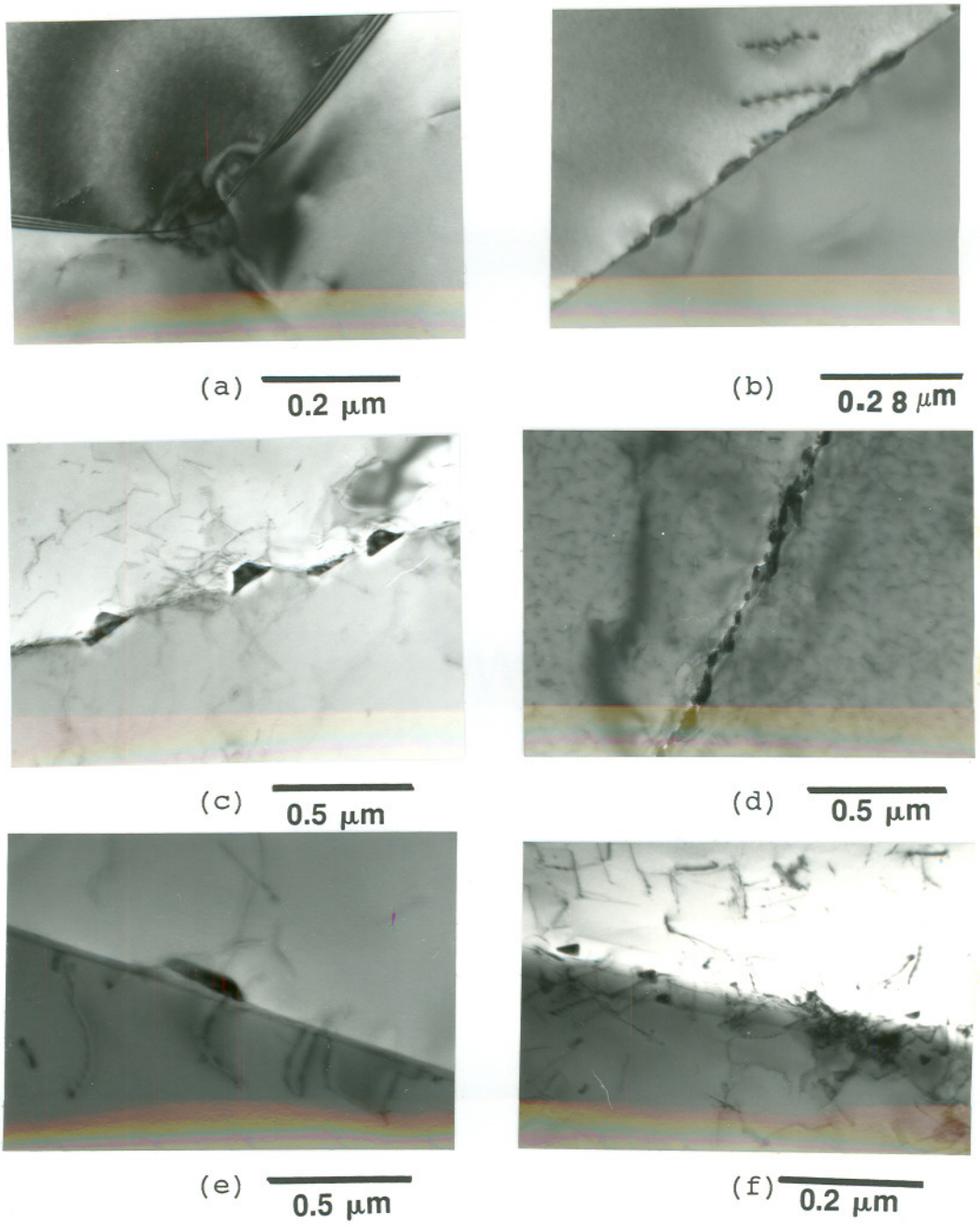

Figure 36. Transmission electron micrographs comparing carbide densities in mill processed (a,b), 1000°C-1hr (c,d) and 1100°C-1hr (e,f) materials after heat treating at 625°C for 10 hrs and 26 hrs.

EVALUATION OF MATERIAL ANNEAL CONDITION EFFECTS

Material condition has been observed to have a significant effect on carbide precipitation and GBCD development in Type 316 SS. This is especially clear when the data for the different materials are looked at in a comparative perspective. Key observations that have been made on the different annealed conditions include

* SA results in grain size changes, which are a function of temperature and time of heat treatment
* Carbide precipitation is seen in samples annealed at 1000°C-1hr and 1050°C-0.5hr, while carbides are absent in the MP, SA1050-1hr and SA1100-1hr materials
* No difference in matrix and twin boundary structures is observed between MP and SA conditions
* Sensitization development for materials annealed at 1000°C and 1050°C (up to 1 hr) is more rapid than for MP and SA1100 samples
* Small grains in the dual size material are more susceptible to attack in the EPR test

These results have mixed agreement with what has been seen in the literature.

Simmons[92] in a companion study on SA effects on DOS during continuous cooling of the same alloy has seen accelerated DOS on SA1000-1hr and SA1050-1hr annealed materials over the MP and SA1100-1hr specimens, as noted here. A difference between the continuous cooling results of Simmons and isothermal results obtained here is the observation of lower (versus comparable) DOS in the 1100°C-1hr treated material versus the MP material during continuous cooling. Observations of comparable isothermal sensitization behavior of MP and SA1100-1hr materials made by Bruemmer[56], however, agrees well with the results obtained in this work.

Presence of carbide precipitates in solution treated materials noted in this work has also been documented by other investigators. The cause for presence of carbide precipitates in SA materials was, however, attributed to incomplete dissolution of carbides formed during mill working of the SS, rather than precipitation occurring at SA temperatures, as was the case here.

Observations of low levels of deformation in the MP and SA materials and preferential attack on small grains that do not grow during solution annealing have, however, not been reported by other researchers. These results are, therefore, important observations which may only be specific to this work.

ANNEALING EFFECTS ON MICROSTRUCTURAL DEVELOPMENT

Mill Processed Material Microstructure

The observation of an equiaxed, fine grain structure and low dislocation density in the MP material indicates that the 1100°C-5 min heat treatment provided by the mill was adequate to anneal the damage caused during TM treatment of the pipe section. Recrystallization data[32] on a similar Type 316 SS further indicates that complete recrystallization of the alloy requires only 100 seconds (≈1.5 minutes) at 1040°C for a 20% strained condition which is well within the heat treatment given to the pipe. These observations appear to imply that the mill anneal treatment has produced recrystallization of the MP pipe. The extremely small 0.25μm grain observed in Figure 22 may, in fact, be a location in the material where recrystallization (but no grain growth) occurred during the mill annealing heat treatment.

Solution Annealed Material Microstructure

Solution heat treatment of the MP material at 1000°C to 1100°C did not seem to produce a change in the matrix and twin boundary deformation levels. This is because the initial mill condition already had very low levels of deformation which cannot be reduced further during high temperature annealing.

Presence of carbides in the 1050°C-0.5 hr and 1000°C-1hr samples and absence of carbides in MP samples indicates that carbide precipitation occurred at the lower temperature and time ranges of SA treatments. Absence of carbides in the SA1050-1hr and SA1100-1hr samples further suggests that dissolution of carbides occurred at the higher range of annealing treatments. The grain growth data can also be explained by this precipitation-dissolution interaction with precipitated boundaries being pinned and unable to grow during annealing, and unprecipitated boundaries being able to grow freely. The establishment of a direct link between carbide precipitation and grain growth was, however, not possible because the temperature and times used for SA can also produce grain growth patterns similar to that seen in this work.

The carbide precipitation data does not agree with experimental solubility data developed by Deighton[93], Weiss and Stickler[94] and Lai et al[95] who stated that complete carbon solubility for a 0.058%C Type 316 SS occurs below 1000°C, and precipitation is possible only at temperatures below this temperature. The fact remains, however, that carbides have been experimentally observed in samples heated at up to 1050°C and cannot be contradicted. Hall and Briant[96] have also made

similar, contradictory observations of M_7C_3 carbide precipitation beyond reported solubility temperatures in Inconel Alloy 600. Caution is, therefore, advised in the extrapolation of solubility data developed on specific materials to universal application to all materials.

ISOTHERMAL GRAIN BOUNDARY CHROMIUM DEPLETION DEVELOPMENT

Mill Processed Material

The EPR test measurements made on the mill treated material (Figure 29) can be explained based on thermodynamic and kinetic aspects of the GBCD phenomena. The low EPRDOS values measured at 550°C are due to the extremely slow kinetics of chromium diffusion which limits the amount of carbide precipitation at this temperature. At 625°C and 670°C, however, favorable thermodynamics and diffusion kinetics cause an increase in both width and depth of chromium depletion with increasing time of heat treatment. The net volume depletion below 13.5% Cr, and EPRDOS values, depends on a balance between these two variables, with increasing width resulting in an increase in VP and increasing Cr_{min} causing a decrease in VP. The increase in EPRDOS observed at 625°C and 670°C indicates that the width effect dominates at these temperatures, at least for the short times of treatment used in the current work. At time significantly longer than that examined in this work, however, the Cr_{min} values will become high enough to effect a decrease in DOS.

At high temperatures (780-850°C) the initial Cr_{min} is high (above 9 - 10%[56]) and causes a decrease in VP and EPRDOS even

at short times of heat treatment. At 850°C the initial chromium minimum dominates to the extent that only low EPRDOS values are observed at this temperatures. The entire sensitization-desensitization cycle also occurs rapidly due to the Cr_{min} reaching 13.5% at short times (within those used in this study).

The thermodynamic and kinetic aspects of GBCD development in the MP material are also reflected in the TTS diagram of Figure 37. This diagram was drawn to map the time and temperature treatments required to reach fixed DOS (or iso-DOS) values of 5, 25 and 60 C/cm^2. The TTS indicates that longer times at low temperatures (below 600°C) are required to produce the same DOS values versus high temperatures due to slow chromium diffusion kinetics at these temperatures. Higher temperature EPRDOS values are also limited by the high thermodynamic chromium minimum values and effects of desensitization on the process.

Solution Annealed Materials

Sensitization development in the SA1100-1hr material has essentially the same thermodynamic and kinetic characteristics as for the MP material. Absence of carbides in this condition implies that nucleation and growth of carbides is required for

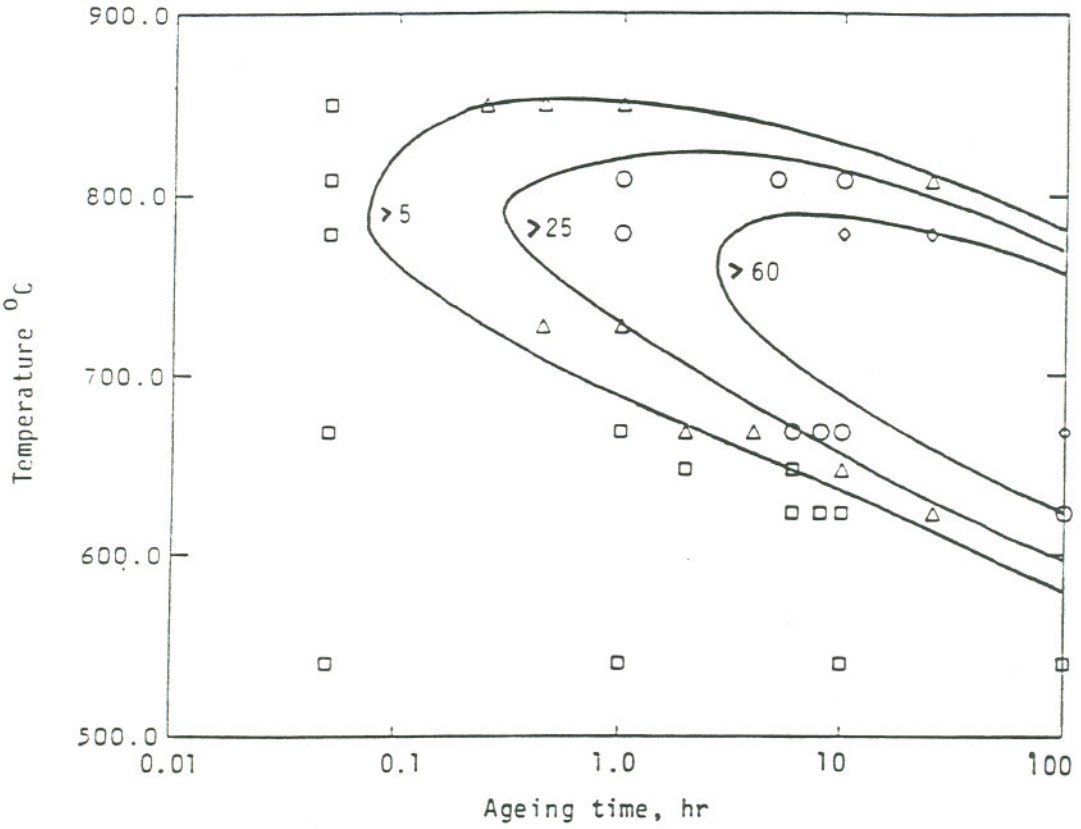

Figure 37. Time-temperature-sensitization diagram for mill processed 316 SS showing time and temperature treatments required to produce constant or iso-DOS lines of 5, 25 and 60 C/cm^2.

SA1100-1hr samples to develop GBCD. Comparable DOS values obtained in the MP and SA1100-1hr samples further indicates that differences in grain sizes of these materials is not reflected in their sensitization response. Bruemmer[56] made a similar observation in sensitization studies on 304 and 316 SS, though an additional observation of a delay in desensitization of larger grain SA materials at longer times of treatment (than used in this work) was also noted.

The presence of carbides in the as-quenched state of the 1000°C-1 hr and 1050°C-0.5 hr specimens is the cause for accelerated sensitization development observed in these samples. This is because nucleation of carbides is no longer a pre-cursor to the initiation of GBCD, and rapid growth on nucleated carbides will result in accelerated DOS even at the shortest times of heat treatment, as observed.

The observation of accelerated EPRDOS in the SA1050-1hr samples was not supported by the absence of carbides noted during TEM of this material. It may be that carbide precipitation in this material took place on selected boundaries in the material, but were not observed due to limited sample area seen in the TEM. This is more likely to be on boundaries on small grains, because it appeared that these boundaries were attacked first during EPR testing.

MATERIAL SELECTION

The microstructural and GBCD studies conducted in this work prompted selection of the SA1100-1hr condition as the initial material for the study on deformation effects on sensitization. This material had a documented 1100°C-1hr prior history, low levels of deformation, carbide-free grain boundaries and sensitization development which were well understood based on thermodynamic and kinetic concepts of the depletion phenomena.

The MP specimens also had similar deformation structures and GBCD development as the SA1100-1hr material. The MP material condition was, however, not selected for further study as the initial mill treatment was not well documented.

Accelerated sensitization development was observed in the SA1000 and SA1050-0.5,1hr samples, which was due to the precipitation of carbides during the annealing treatment. These materials were not considered as suitable candidates for the deformation study since the initial microstructures already had carbides which was expected to mask the thermodynamic (and possibly other) effects of strain on the phenomena.

CHAPTER 4

DEFORMATION EFFECTS ON GRAIN BOUNDARY CHROMIUM DEPLETION

TASK ANALYSIS

This task evaluates deformation effects on GBCD in solution annealed Type 316 SS. The effects of strain on matrix and twin boundary structures, isothermal GBCD or EPRDOS values and carbide precipitation have been examined.

MICROSTRUCTURAL CHARACTERIZATION OF DEFORMATION SPECIMENS

SOLUTION ANNEALED 1100°C-1HR MATERIAL

Defect structure analysis of the unstrained, solution annealed material has already been discussed in Chapter 3 (Figures 25, 28). The key observation made on the microstructure of this material was that it contained low levels of deformation in the matrix and around twin boundaries. Matrix dislocation density measured on this material was approximately 3 x $10^8/cm^2$, which is typical of well annealed materials. No evidence of carbide precipitation was also seen on the grain boundaries of this material condition.

DEFORMATION EFFECTS ON MICROSTRUCTURAL DEVELOPMENT

Matrix Deformation

Deformation of the SA1100-1hr material to 2% sharply increased the matrix defect structure (Figure 38a). Matrix dislocations were created by the straining process and observed to be of significant levels in every grain. An increase in the dislocation density to 5 x $10^9/cm^2$ was measured in this strain material. Evidence of a planar dislocation structure was also found at a strain level of 2%.

Increasing the strain to 6% resulted in further uniform increases in matrix dislocations (Figure 38b). Dislocation interactions and tangles were also evident. The dislocation density increased to about 6 x $10^9/cm^2$ in the 6% strain material condition. No significant deformation banding was seen at the 6% strain level, although further development of the planar dislocation structure seen at 2% was also apparent.

The dislocation density increased further on straining to 16% (Figure 38c), though measurement of density at this level was difficult due to formation of an overlapping dislocation structure. Densities were measured to be approximately

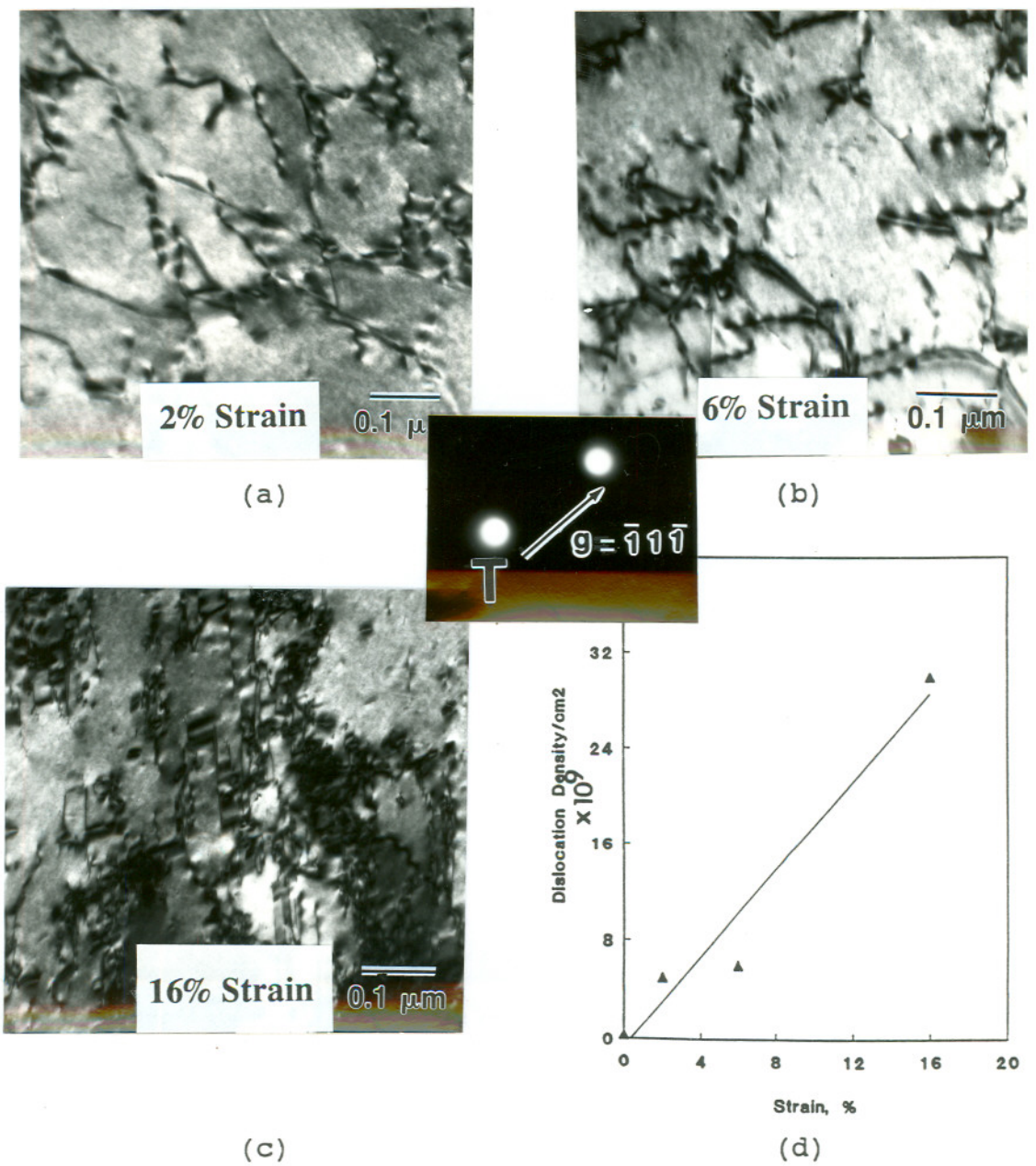

Figure 38. Deformation effects on increase in matrix deformation as documented in TEM micrographs of specimens deformed to 2% (a), 6% (b) and 16% (c) and in a comparison plot of dislocation density versus strain (d).

3 x $10^{10}/cm^2$. This indicated a linear relationship between dislocation density and strain, as documented in Figure 38d.

An intermix of stacking faults and deformation twins were present at 16% strain levels giving the appearance of a "banded" microstructure to the specimen (Figure 39a). The twin-faulted region was extremely irregular making it difficult to identify the individual faults. Twin-faults also appeared to favor certain grains over others, rather than being evenly spread throughout the sample. Variations within grains were also possible to the extent that cellular dislocation regions were observed at some locations on the specimen (Figure 39b).

Deformation induced α'- martensite has been reported to form at twin-fault intersections above 5% strain in Type 304 SS.[2] Similar intersections of twin-faulted regions obtained here were carefully examined by TEM in this work to identify if the α' phase formed in Type 316SS. A ferrite gage was also used to help verify the presence of martensite in the bulk sample.

No martensite was detected using the ferrite gage technique, even for the lowest ferrite number two magnet on the 16% strain specimen. Transmission electron microscope examination of twin-fault intersections, however, revealed the presence

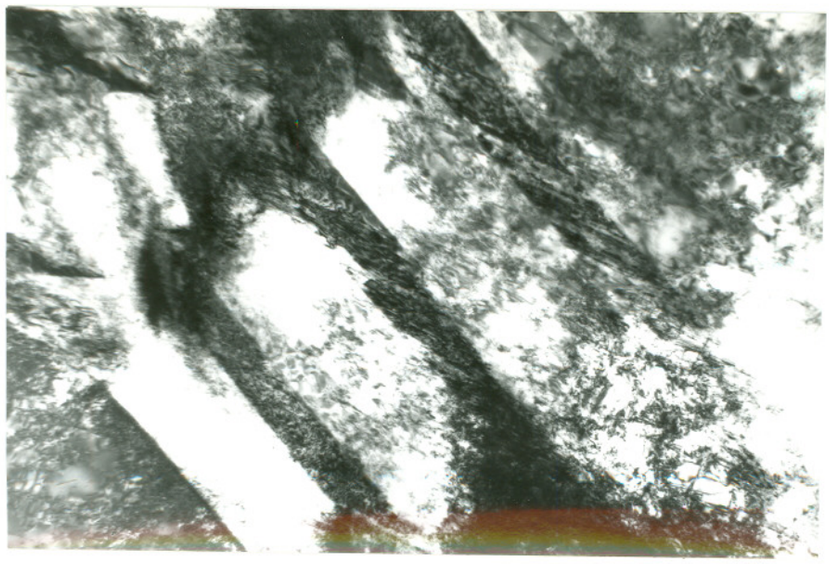

(a)

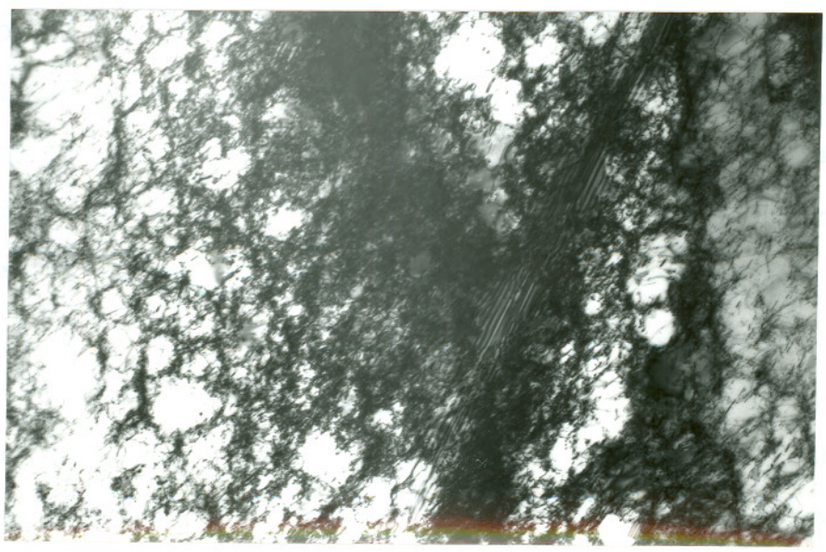

(b)

Figure 39. Transmission electron micrograph documenting the presence of a twin-faulted region (a) and cellular dislocation structure (b) in 16% strained Type 316 stainless steel.

of a phase appearing similar to α'- martensite reported in Type 304 SS[12](Figure 40). The phase tended to be present as thin plates confined to the intersection of twin-faults as seen in Type 304 SS. This isolated observation, however, does not compare to the levels of strain-induced martensite reported for Type 304 SS at comparable strains.

The 25% strain material exhibited a substantial level of deformation banding and twin-fault intersections that was significantly more than that observed at 16% strain level. The twin faulted regions in this material were also more evenly spread and were seen in a larger number of grains (Figure 41). No martensite was seen in the 25% strain sample, despite the large number of deformation band intersections present in this specimen. The ferrite gage measurements also did not register the presence of the bcc phase, thereby, confirming the absence, or very low density of martensite in the bulk of this sample.

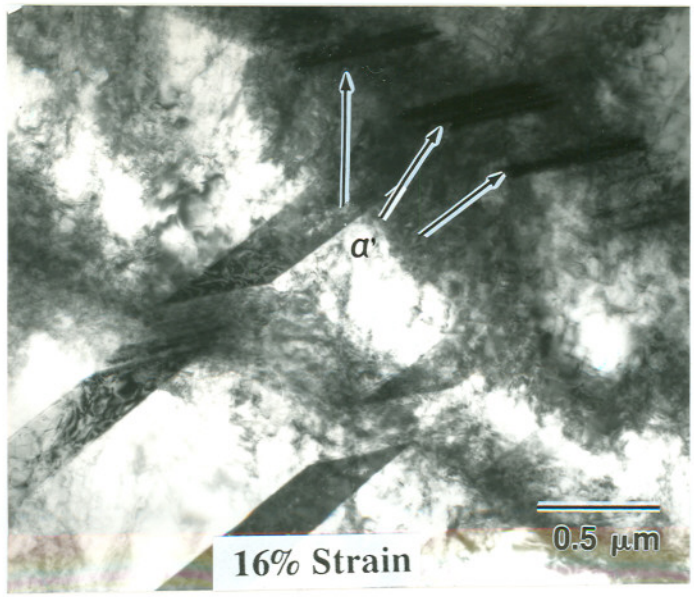

(a)

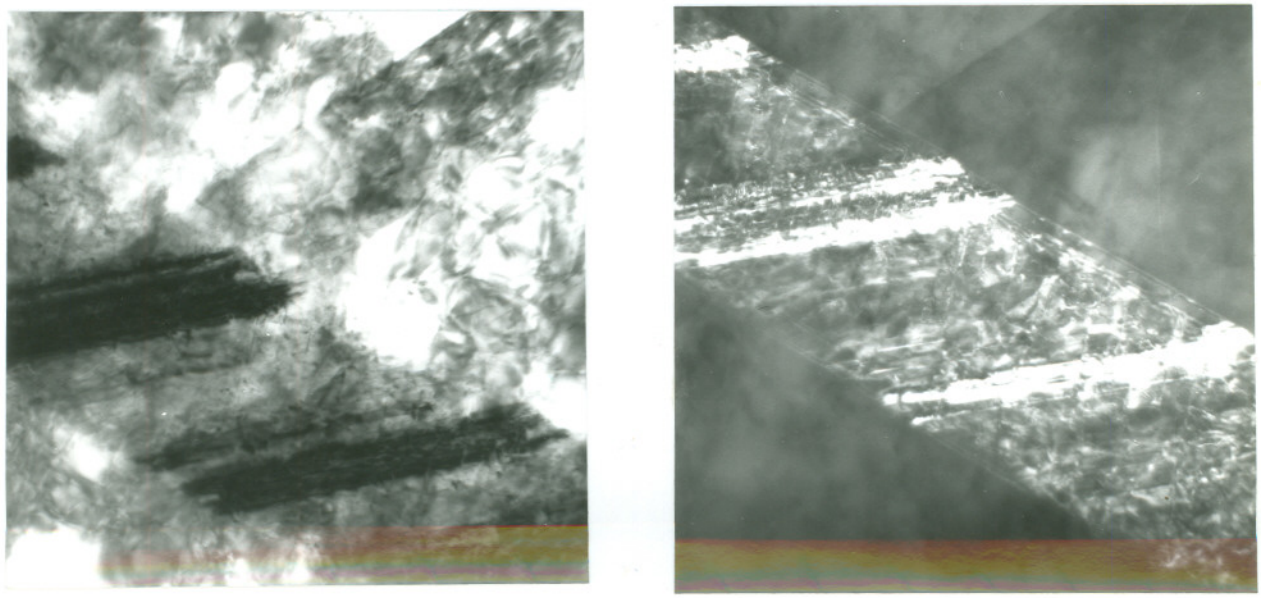

(b)

Figure 40. Transmission electron micrographs showing isolated location of second phase appearing similar to α' martensite in 16% strained sample.

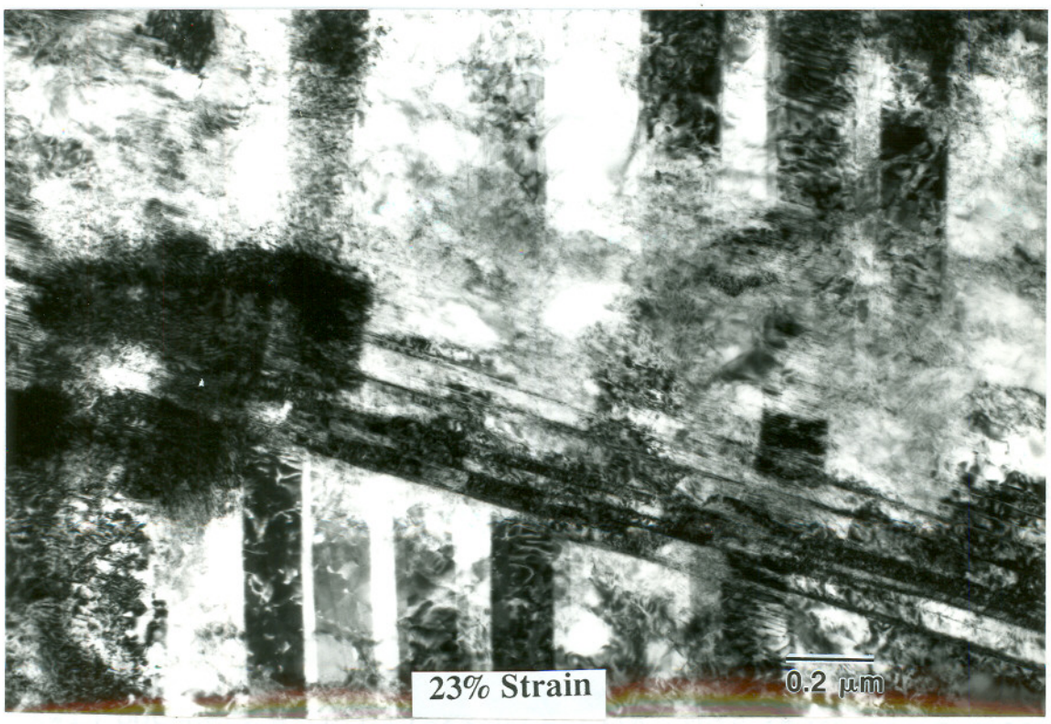

Figure 41. Transmission electron micrograph documenting high density of deformation bands, which intersect at a significant number of locations in the microstructure.

Twin Boundary Deformation

Analysis of dislocation densities near twin boundaries revealed an increase in the density of dislocations around the twin boundary with increasing strain. This increase is clearly seen in the micrographs for the 2% and 16% strained (Figure 42a,b) versus unstrained materials (Figure 25)taken under identical [110] foil orientation conditions. The interface between the twinning crystals was seen to be sharp though some dislocation emission profiles were visible near the interface. In contrast, a dislocation structure was developed along the entire twin boundary even for strains at the lowest level of 2% (Figure 42b). This dislocation structure increased with increasing strain, to the point that at 16% strain individual dislocations were difficult to distinguish due to extensive deformation in the interfacial region (Figure 42c).

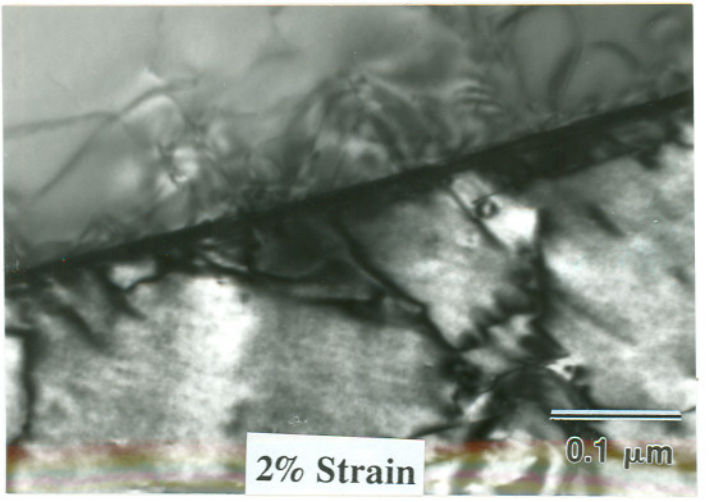

(a)

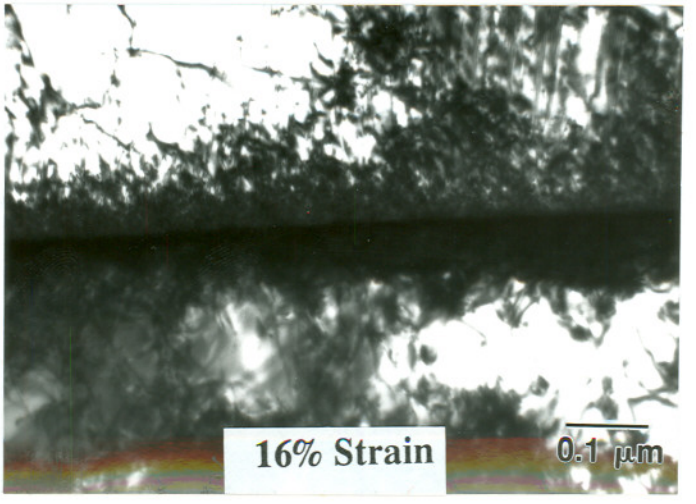

(b)

Figure 42. Transmission electron microscope observations of deformation in the vicinity of annealing twin boundaries for 2% strained (a) and 16% strained (b) specimens. Micrographs were taken under identical [110] foil orientations for an operating reflection of g = (111).

DEFORMATION EFFECTS ON ISOTHERMAL GRAIN BOUNDARY CHROMIUM DEPLETION DEVELOPMENT

TEST MATRIX

Deformation effects on isothermal GBCD was studied for 0 - 35% strain coupons, in the range of 550°C to 850°C from 0.1 to 500 hr using the EPR test and TEM. The matrix of strain specimens and heat treatments examined is summarized in Table 4.

Table 4. Matrix of deformation specimens and heat treatment schedules used for analysis of GBCD in 316 SS.

Strain Level %	Temperature °C	Time hr
0 - 25%	575	0-400
0 - 27%	625	0-100
0 - 35%	670	0- 15
0 - 25%	725	0-2.5
0 - 25%	775	0-1.3

The results observed for deformation effects on GBCD have been separated into five sections

* Unstrained, SA1100-1hr material condition
* Low strain (<20%) induced GBCD at 625°C
* High strain (>20%) induced GBCD at 625°C

* Temperature effects on low strain induced GBCD and
* Temperature effects on high strain induced GBCD

to better understand the phenomena for different strain levels and temperature regimes.

SOLUTION ANNEALED 1100°C-1HR SENSITIZATION DEVELOPMENT

Results on sensitization development in the SA1100-1hr material were presented in Chapter 3. The important observations made are, however, summarized here as a time-temperature-sensitization diagram (Figure 43). This plot shows the time and temperature required to achieve EPRDOS values of 5 and 35 C/cm^2 for temperatures ranging from 575°C to 775°C, and reflects changes in thermodynamics and kinetics of GBCD phenomena occurring with heat treatment (ref: Chapter 3).

The iso-DOS line at 5 C/cm^2 indicates that sensitization development in this material took substantially longer at low temperatures compared to high temperatures. There was a three orders of magnitude difference in the time to achieve 5 C/cm^2 between the lowest and highest temperatures studied. EPRDOS values of 5 C/cm^2 were also achieved in considerably shorter times versus 35 C/cm^2. No desensitization of the material was observed to occur (as in Figure 37) due to shorter times and lower temperatures of heat treatment used for this condition (in comparison to the MP condition).

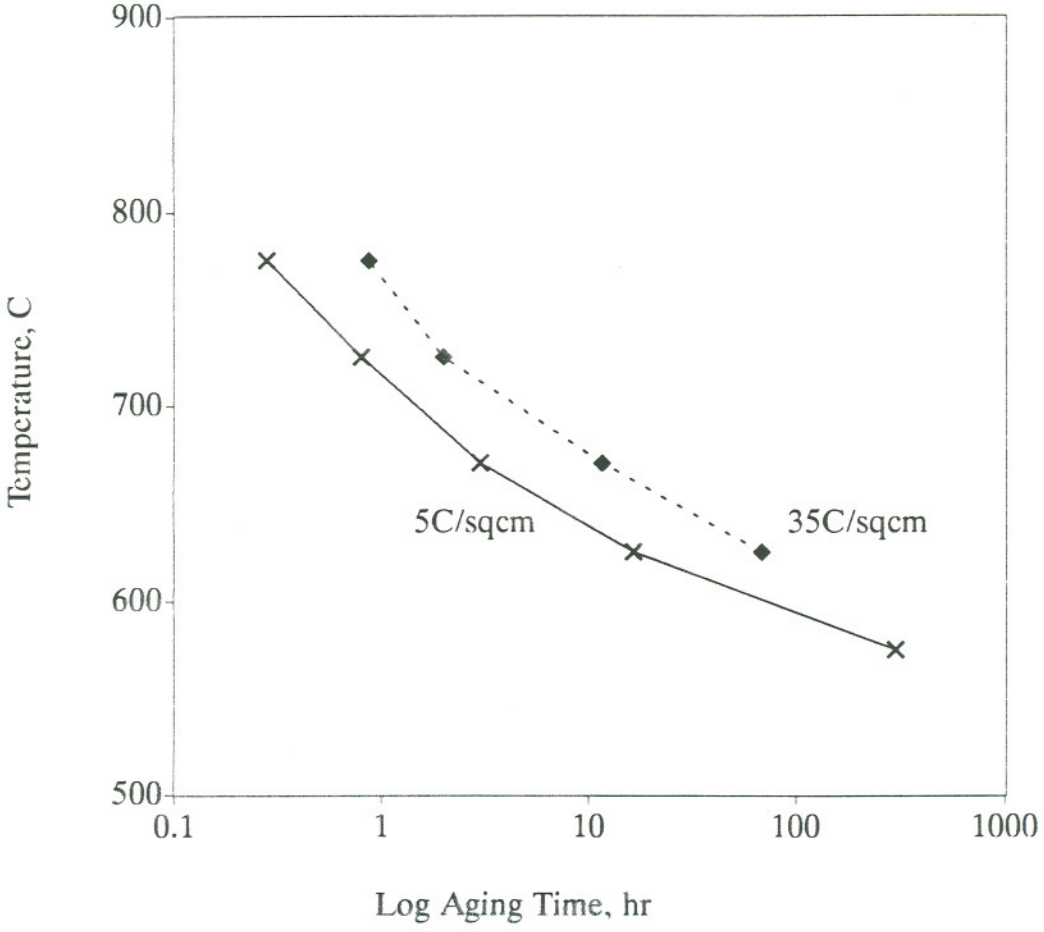

Figure 43. Time temperature sensitization diagram for 1100°C-1hr unstrained material.

LOW STRAIN (< 20%) EFFECTS ON SENSITIZATION AT 625°C

Deformation was observed to accelerate the development of sensitization in Type 316 SS at 625°C. The magnitude to which strain altered the GBCD phenomena in the low strain regime is seen best by comparing EPRDOS values for the unstrained and 16% strained samples heat treated at 625°C for 0 - 100 hrs (Figure 44). The 16% strain material developed GBCD at times less than 2 hrs, and achieved EPRDOS values of 50 C/cm^2 after 20 hours of heat treatment. Both times were shorter than the unstrained specimen where low EPRDOS values were observed even after 20 hrs of heat treatment and values of 5 C/cm^2 and 50 C/cm^2 were measured only after 25 hrs and 100 hrs at 625°C.

Samples with intermediate strain values (2%, 6% and 10%) had sensitization response between those of the two extreme strain specimens (0% and 16%) at 625°C. This is illustrated in Figures 45a and b for short (first 4 to 5 on each data set) and long times (entire data set) by plots of EPRDOS versus time for different strain levels. Both plots show that a systematic increase in EPRDOS occurred with increasing strain levels.

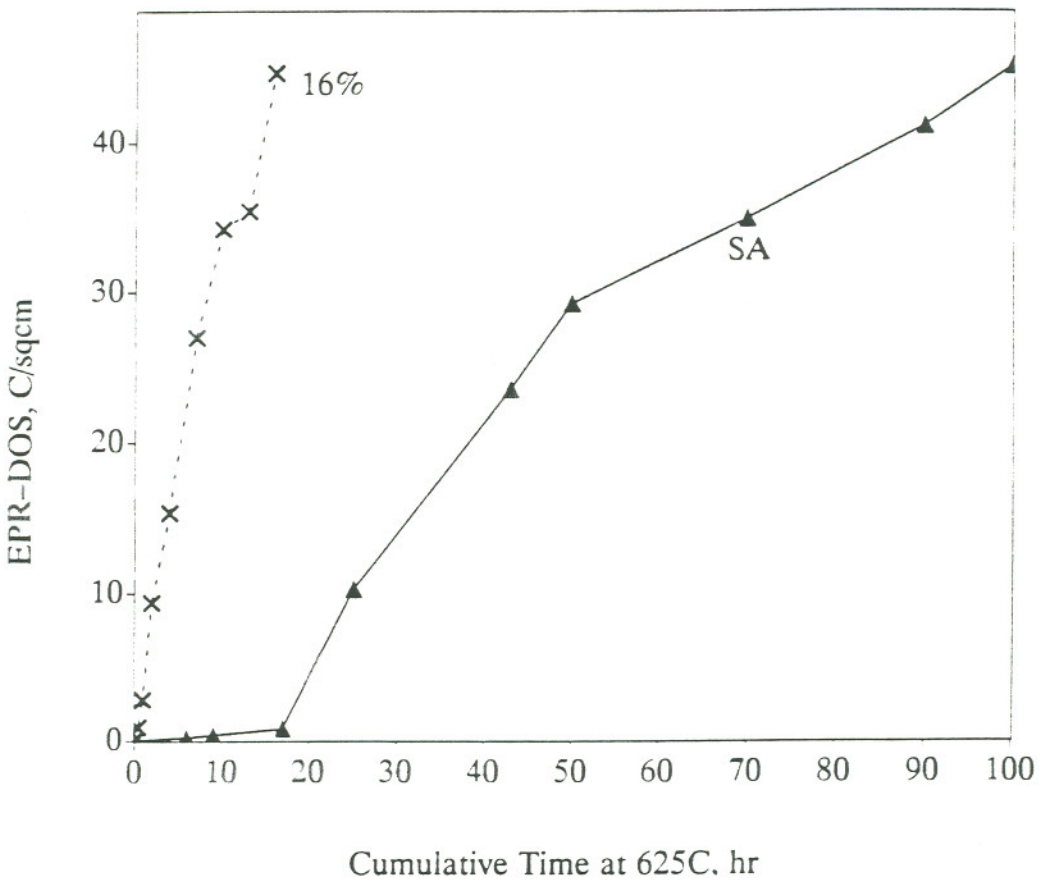

Figure 44. Comparison of sensitization development in unstrained and 16% strained specimens at 625°C documenting the presence of higher sensitization response in strained versus unstrained specimens.

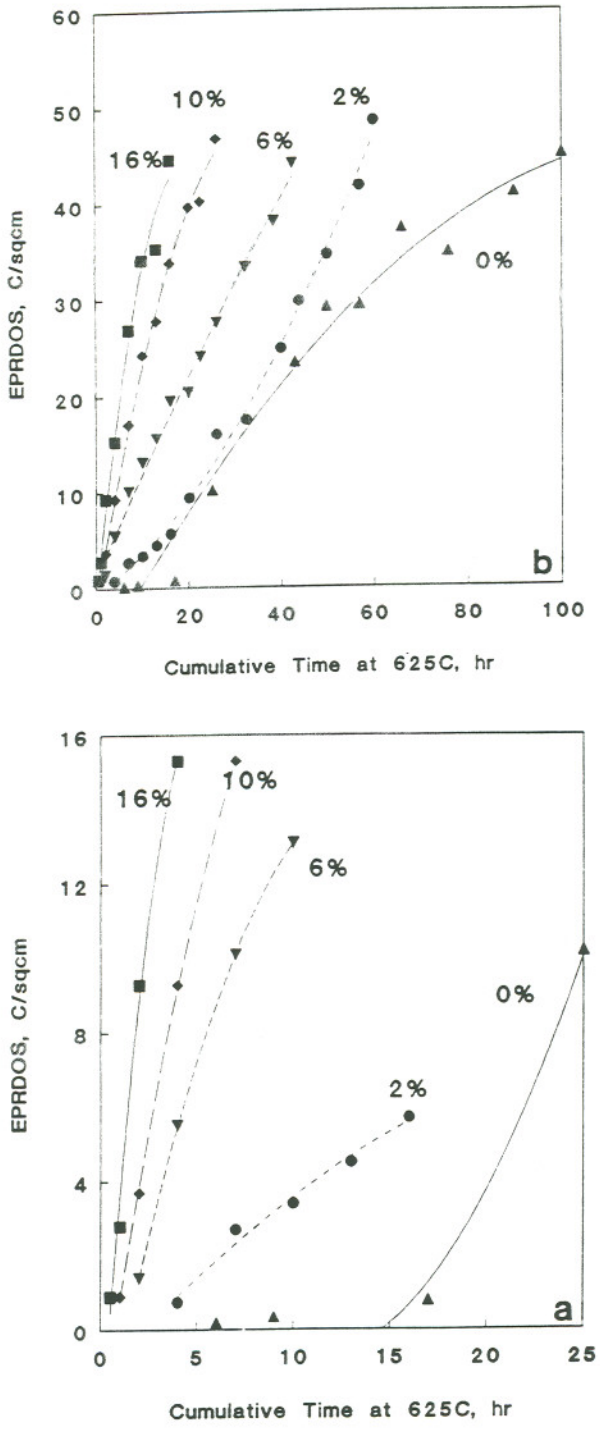

Figure 45. Strain effects on sensitization development at 625°C for short (a) and long (b) heat treatment times at this temperature. Both plots clearly illustrate a continuous increase in EPRDOS values with systematic increase in strain.

The EPRDOS-strain relationship was sometimes nearly linear for certain aging conditions. An example of this linearity is shown in the EPR test data taken after 10 hrs at 625°C (Figure 46). The illustration of a linear relation between EPRDOS and strain parameter was not, however, a general observation and occurred only for specific aging schedules.

The EPR test measurements of increased DOS with increased strain were supported by optical microscope observations as illustrated by micrographs of EPR attack surfaces after 7 hrs at 625C. Continuous grain boundary attack was observed within the 12% - 625°C - 7 hr sample, corroborating the high EPRDOS values measured for this condition (Figure 47a). Semi-continuous IG attack was observed on the 6% strain specimen (Figure 47b) which had an EPRDOS value of between 5 and 10 C/cm^2. Only isolated grain boundary attack was observed on the 0% - 625°C - 7 hr material after a similar aging treatment due to the unsensitized nature of this sample (Figure 47c).

The EPR test indications of higher DOS on strained materials were also supported by comparing carbide density on strained versus unstrained specimens. Continuous grain boundary carbide

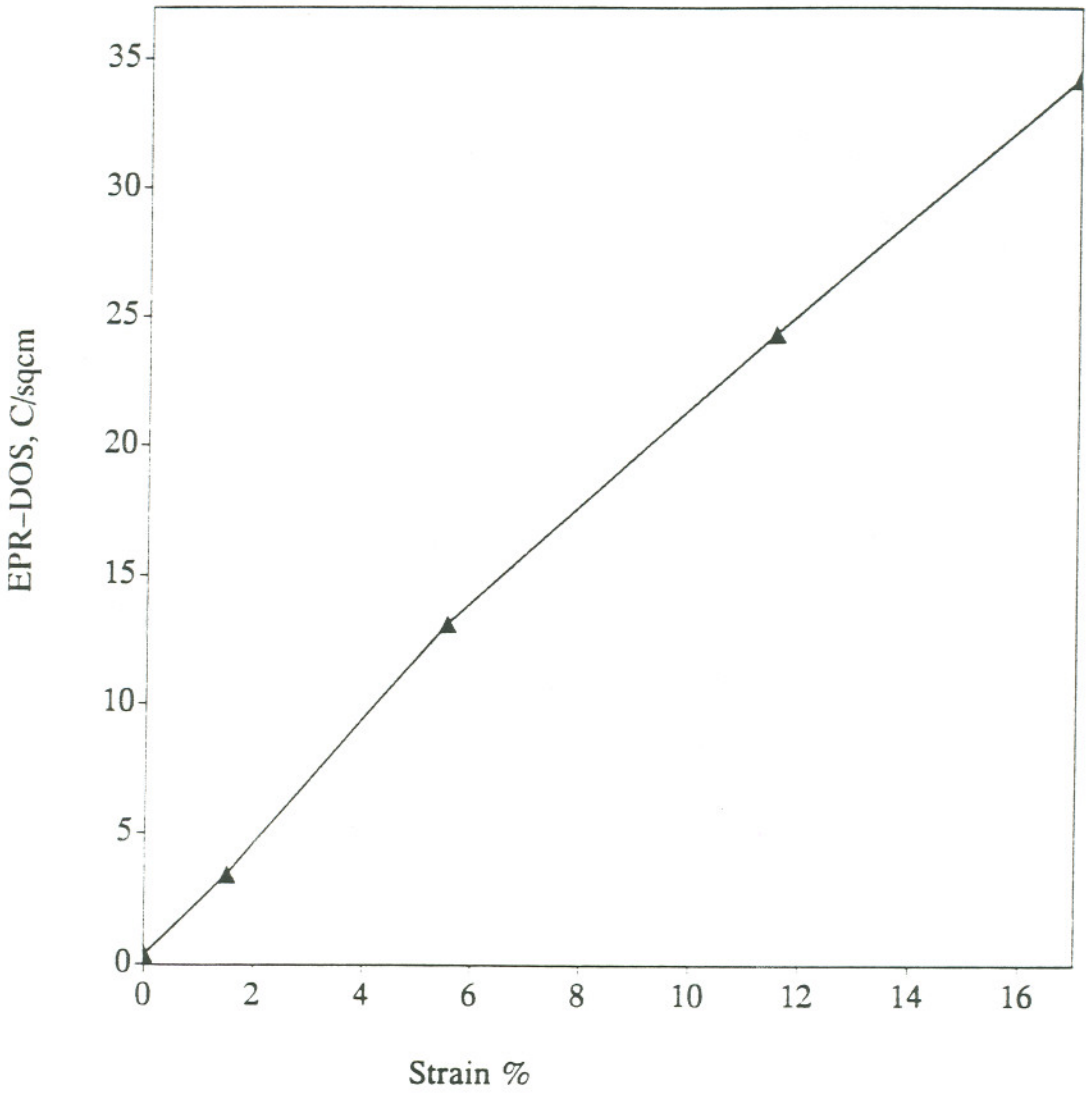

Figure 46. Variation of EPRDOS with strain for 625°C - 10 hr heat treatment demonstrating near-linear relationship between EPRDOS and strain for this particular treatment schedule.

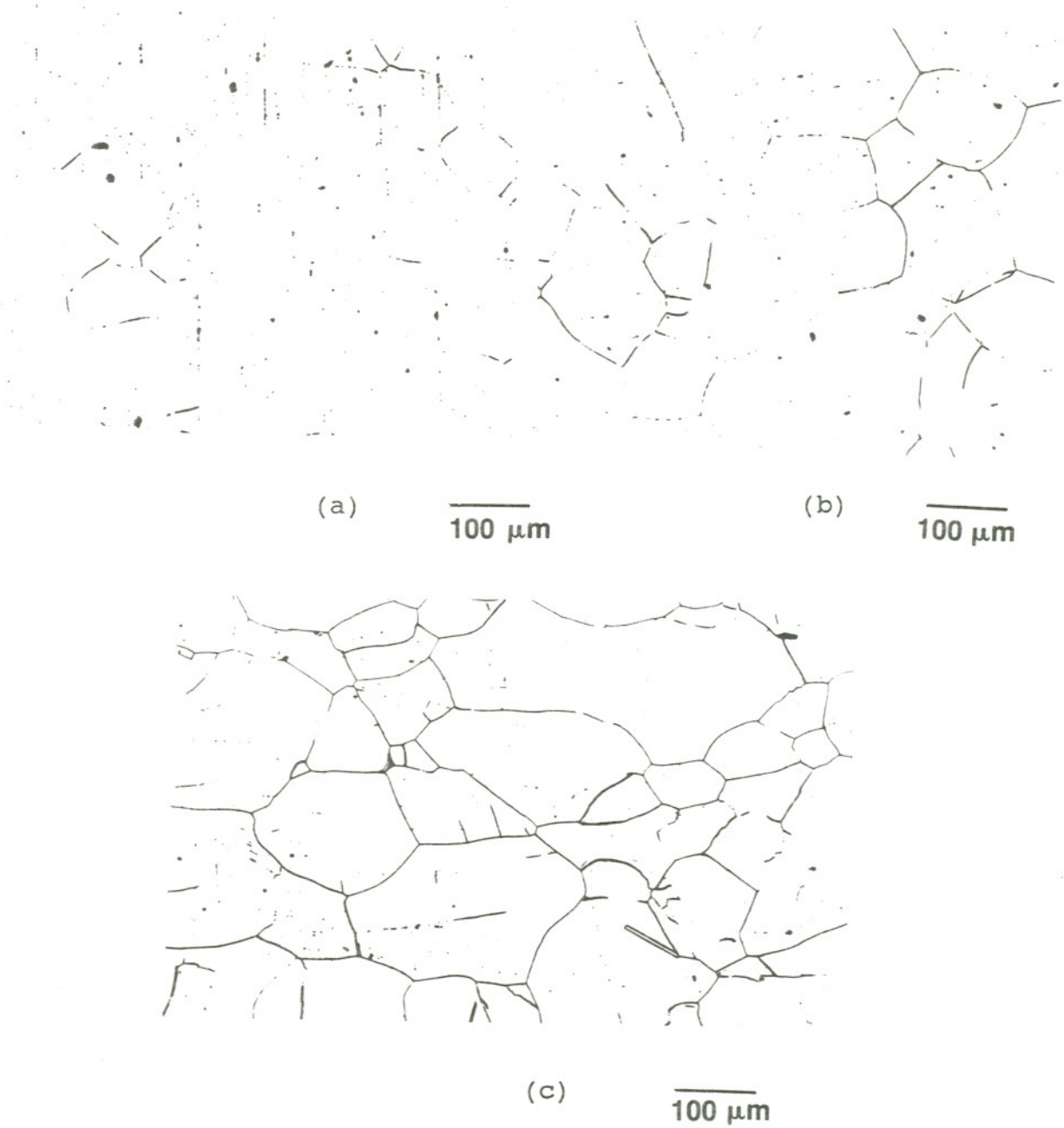

Figure 47. Optical micrographs of EPR test attack surfaces illustrating increase in extent of intergranular attack with strain for 0% (a), 6% (b) and 12% (c) strain levels after a 625°C-7hr heat treatment.

precipitation was seen in the bright-field (BF) and dark-field (DF) micrographs for the 16% - 625°C - 20hr strain material (Figures 48a,b). Carbides in this strain specimen were small, about 0.1 μm in length and formed a continuous film on almost every grain boundary. Unstrained samples, in contrast, exhibited relatively unprecipitated grain boundaries after similar aging conditions and isolated to semi-continuous carbide precipitates were seen only after 26 hrs of heat treatment at 625°C (Figure 36e,f).

Comparisons of 12% strained and unstrained EPR attack microstructures after long term treatments at 625°C did not show any difference in the extent of grain boundary attack despite the differences in EPRDOS values for these materials. This is because for EPR values above 10 to 15 C/cm^2 continuous grain boundary attack is seen on all specimens. There were still, however, microstructural differences between strained and unstrained materials. The difference was seen in terms of the number of annealing twin boundaries attacked during the test and was higher in the 12% strain sample. Attack on annealing twin boundaries was, in fact, observed to be higher on strained versus unstrained samples even at equivalent EPRDOS values of 50 C/cm^2, as illustrated by the micrographs of Figure 49.

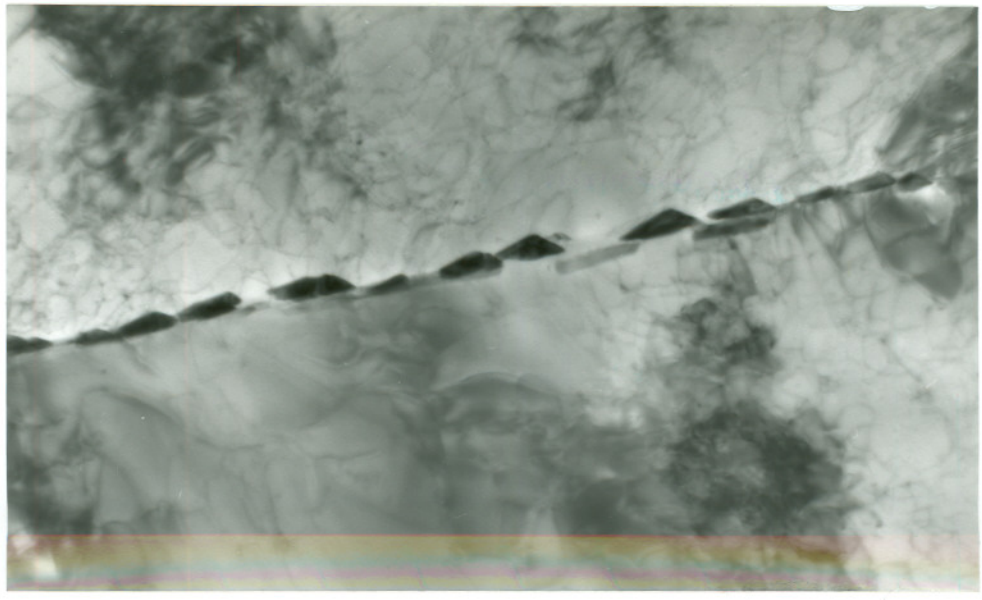

(a) 0.25 μm

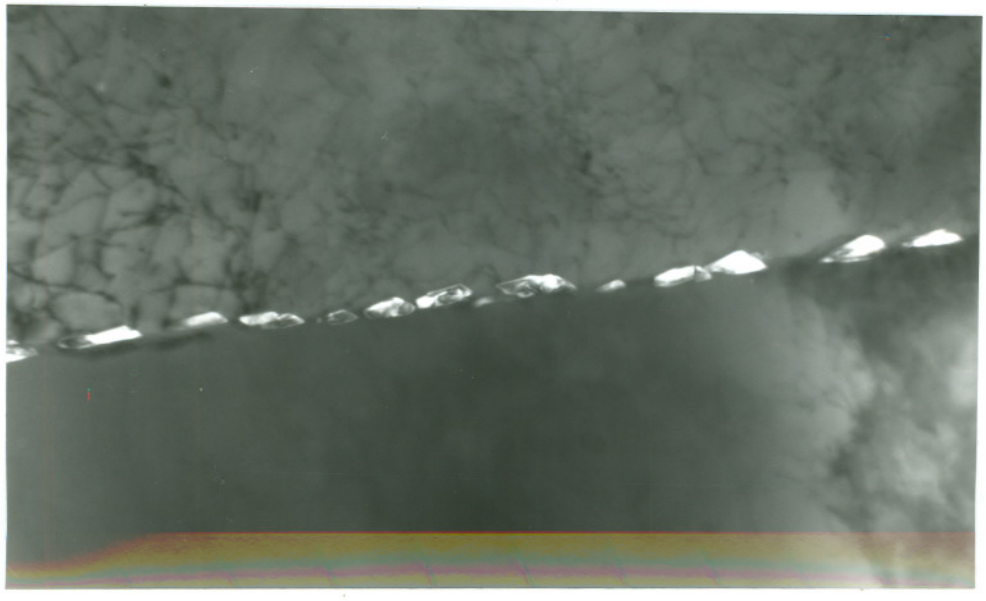

(b) 0.25 μm

Figure 48. Bright field (a) and dark field (b) transmission electron micrographs illustrating carbide precipitation in 16% strained specimens after 20 hrs at 625°C.

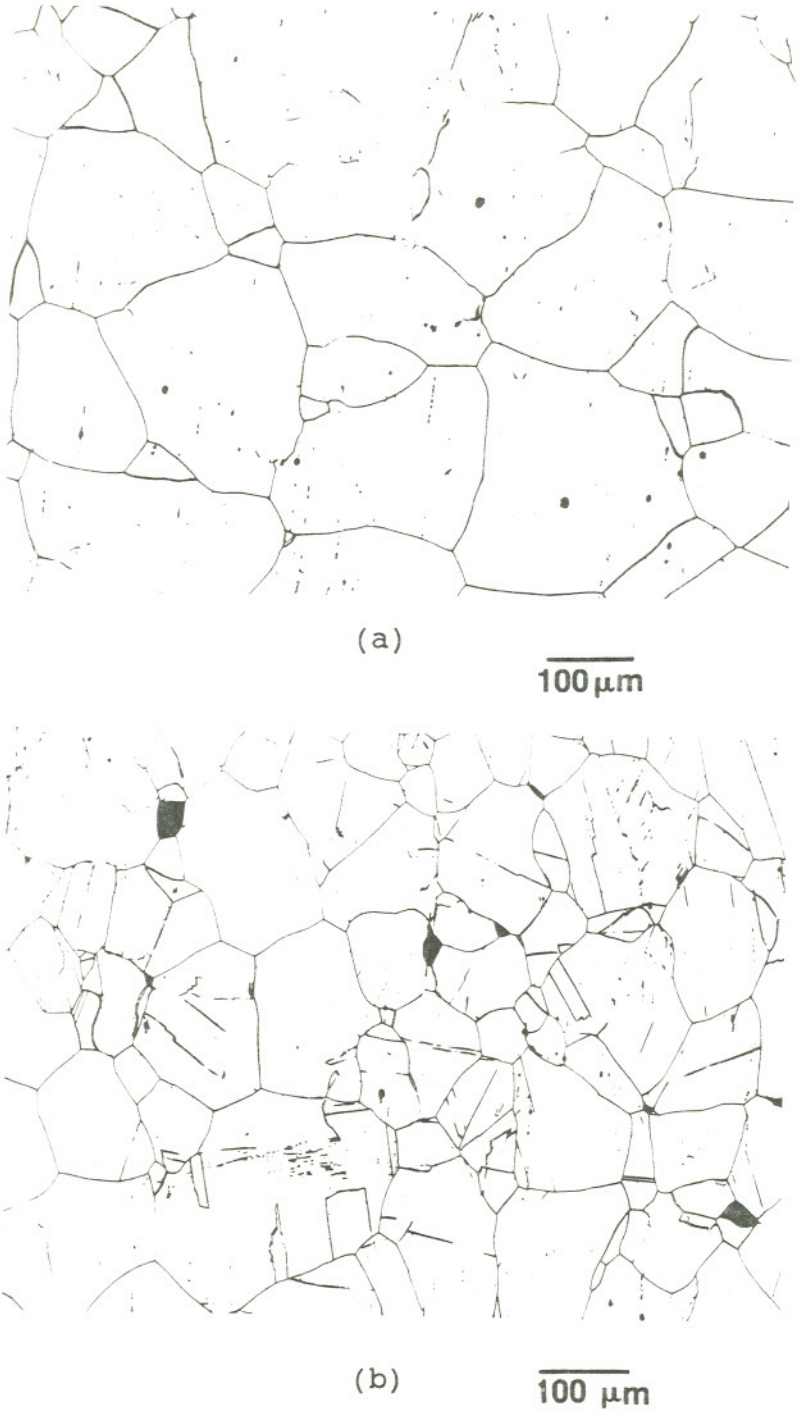

Figure 49. Optical micrographs of EPR test attack surfaces comparing strain effects on extent of intergranular attack for unstrained (a) and 12% strained (b) samples with identical EPRDOS values of 50 C/cm^2.

An important observation made on the EPR microstructure of the 16% strain material at longer heat treatment times was the presence of transgranular (TG) attack (Figure 50). Transgranular attack was defined to be present in materials where etching on the EPR test surface occurred in a linear manner, seemingly along certain favored crystallographic orientations within grains. This attack was first observed in the 16%-625°C-10 hr specimen and increased with increasing heat treatment.

Attack within grains is considered important as it affects the quantification of EPRDOS, which normalizes the attack to grain boundary area. The TG attack on the 16% strain specimen was not, however, significant and neglected in the computation of EPRDOS for this sample.

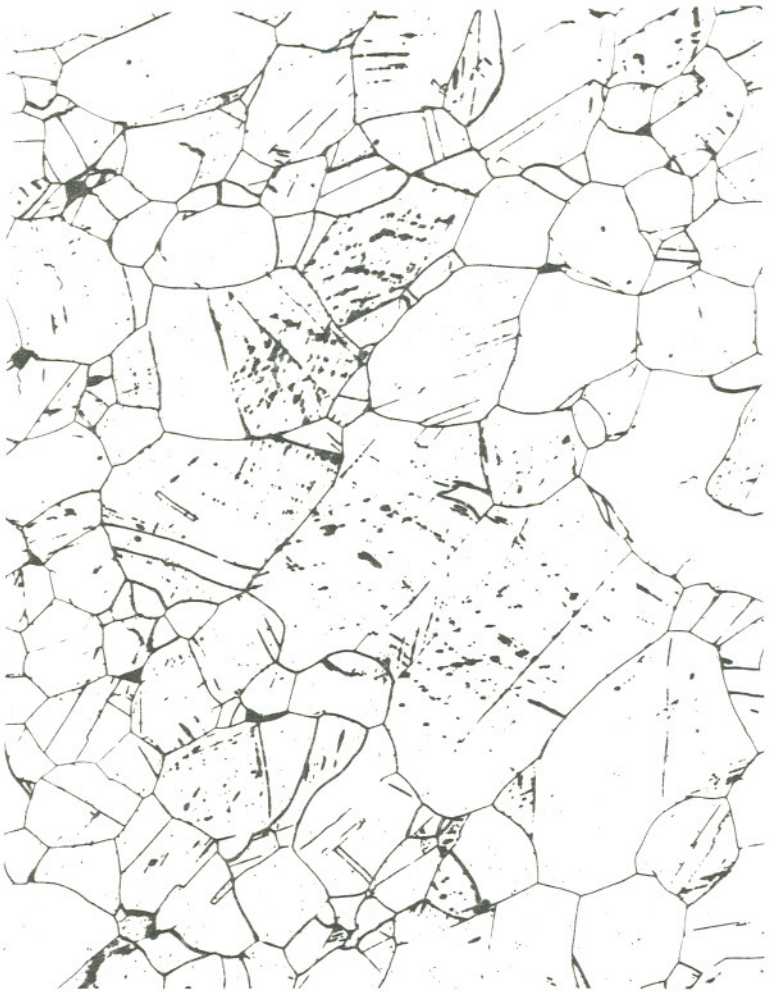

Figure 50. Optical micrograph of EPR attack surface illustrating the presence of transgranular etching in the 16% strain specimen after 20 hrs of heat treatment at 625°C.

HIGH STRAIN EFFECTS ON SENSITIZATION AT 625°C

Samples with strain above 20% were also examined after heat treatment at 625°C in order to develop an understanding of GBCD in comparison with low strain specimens. Earlier work[50] reported that straining above 20% produces alterations in sensitization and SCC behavior by inducing significant levels of TG attack. Knowledge of this phenomena is important as it represents a change in the IG chromium depletion phenomena in SS. Indications of the presence of this change were already observed in the 16% strain sample.

Effects of high strain on charge Q generated during EPR testing for 0%, 16% and 27% strain materials at 625°C is illustrated in Figure 51. The data demonstrates that higher strain materials result in higher Q values than lower strain materials. This would usually reflect a higher EPRDOS, and GBCD in the higher strain materials. However, in lieu of the fact that TG attack occurs at high strain levels, the microstructure must be critically examined before normalizing the charge value with respect to grain boundary attack (for computing EPRDOS).

Examination of the microstructure for 27% strained samples showed the presence of mixed TG + IG attack (Figure 52). The

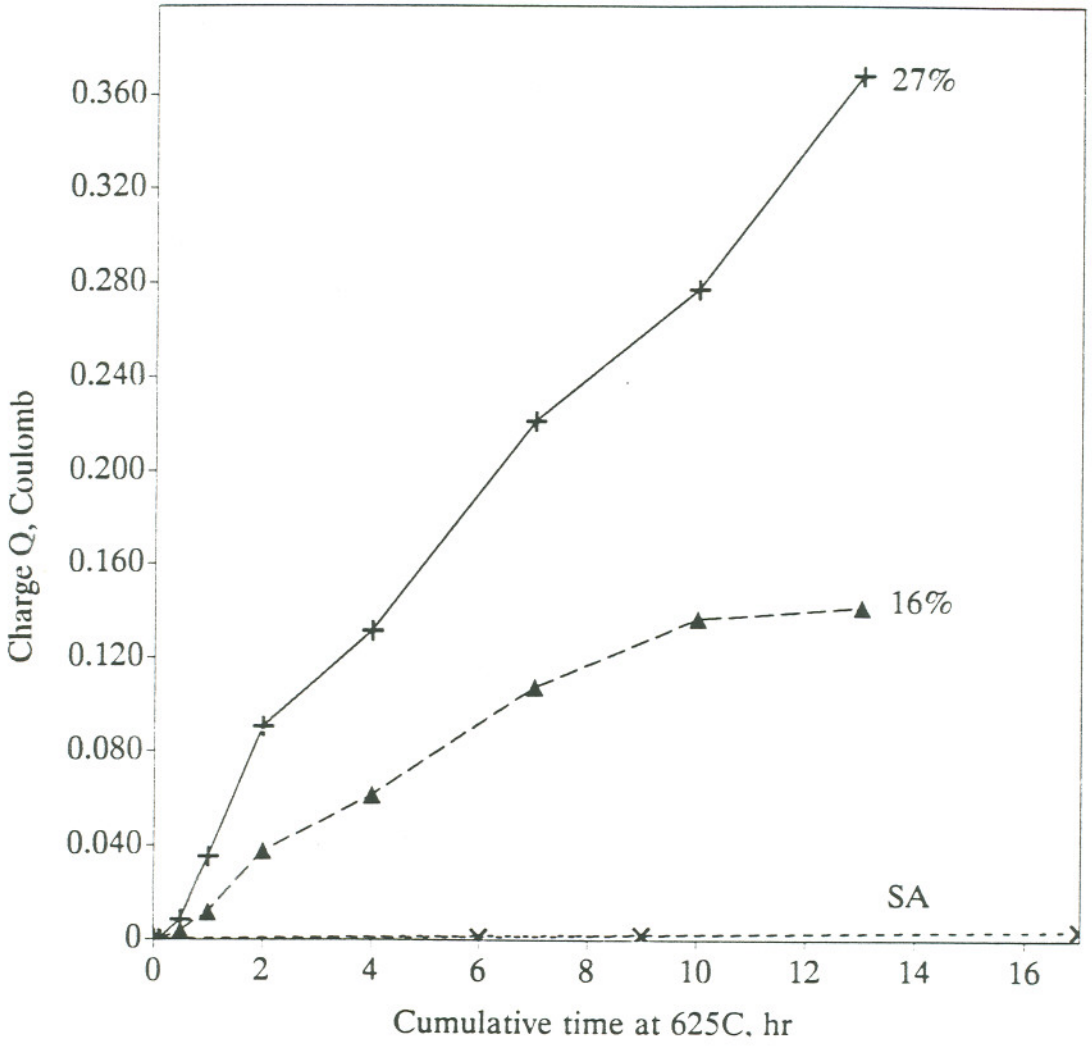

Figure 51. Comparison of charge Q (in coulombs) produced during EPR testing of 0%, 16% and 27% strain samples at 625°C demonstrating increase in Q values with increasing strain.

Figure 52. Optical micrograph of EPR attack surface for 27% strained sample heat treated for 10 hrs at 625°C.

TG attack was low at short times, but subsequently increased to significant amounts at longer times. Delineation of the grains by TG attack along favored orientations similar to the 16% strain sample was also observed.

The presence of TG attack in the 27% strain material was considered significant enough to cause grain partitioning leading to an overestimate in Q and EPRDOS produced by the grain boundaries. This is because while Q values indicate higher EPRDOS values in the 27% strain material than the 16% strain material, the DOS values (on grain boundaries) may actually be lower due to contribution from the TG areas. Estimation of this contribution was difficult and conversions of Q to EPRDOS were not performed.

Carbide precipitates present on the deformation structure of the 27% strain material were considered to be the cause for the intra-granular chromium depletion (and TG attack) in this material (Figure 53). The carbides were clustered around dislocations within the grain, rather than being spread evenly about the entire matrix (Figure 53a,b). An association of carbides with the planar deformation structure was also noted (Figure 53c), while no carbides were seen at a region of deformation banding in the material (Figure 53d).

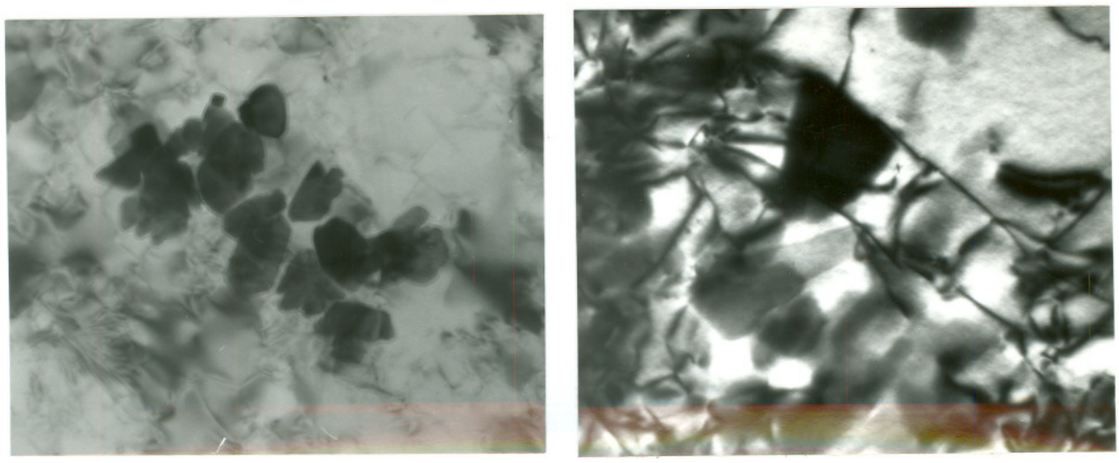

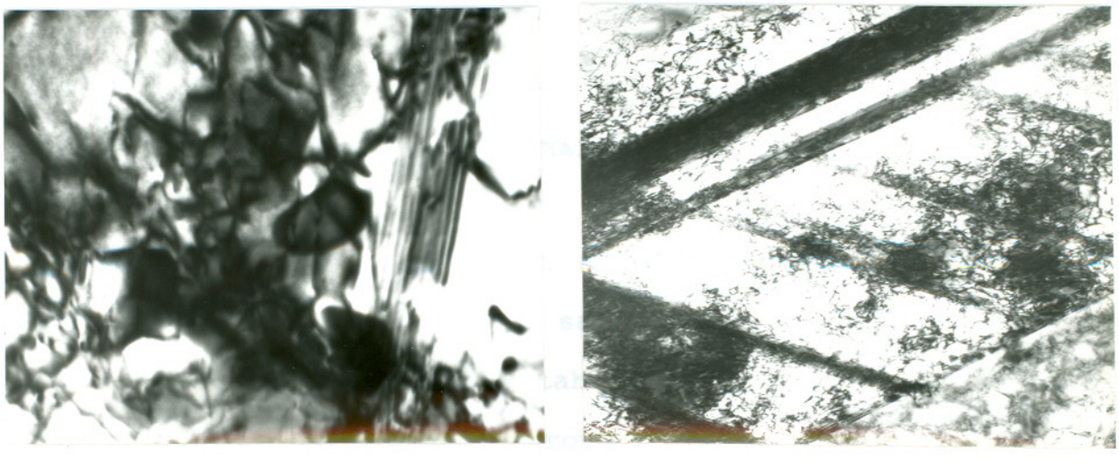

Figure 53. Transmission electron micrographs documenting locations at which intragranular carbide precipitation was observed on the 27% strain sample heat treated for 20 hrs at 625°C. The locations observed to show intragranular precipitation include regions of dislocations

TEMPERATURE EFFECTS ON LOW STRAIN INDUCED SENSITIZATION

The effect of temperature on GBCD was examined at 575°C, 670°C, 725°C and 775°C in the same detail as the 625°C work. This provided a detailed database for deformation induced sensitization development through the sensitization range (575°C- 775°C). The database developed is represented in Figures 54 through 57 for both short and long times of heat treatment at each temperature, as was done for the 625°C data. This separation facilitated comparisons amongst different temperatures in similar frames of reference.

The 575°C data set showed similar EPRDOS values for 6% to 16% strain samples at the start of sensitization development (Figure 54a). These values were higher than the 2% and unstrained SA specimens. At longer times, however, the separation among strain data sets was apparent with increasing strains resulting in continuously increasing EPRDOS values (Figure 54b).

Short times at 670°C indicated that strain samples of 7% have a higher DOS than 0%, 2% and 10% samples (Figure 55a). The 14% strain samples, however, had a higher sensitization response than this specimen. At long times a systematic increase in EPRDOS with increasing strain was again observed (Figure 55b).

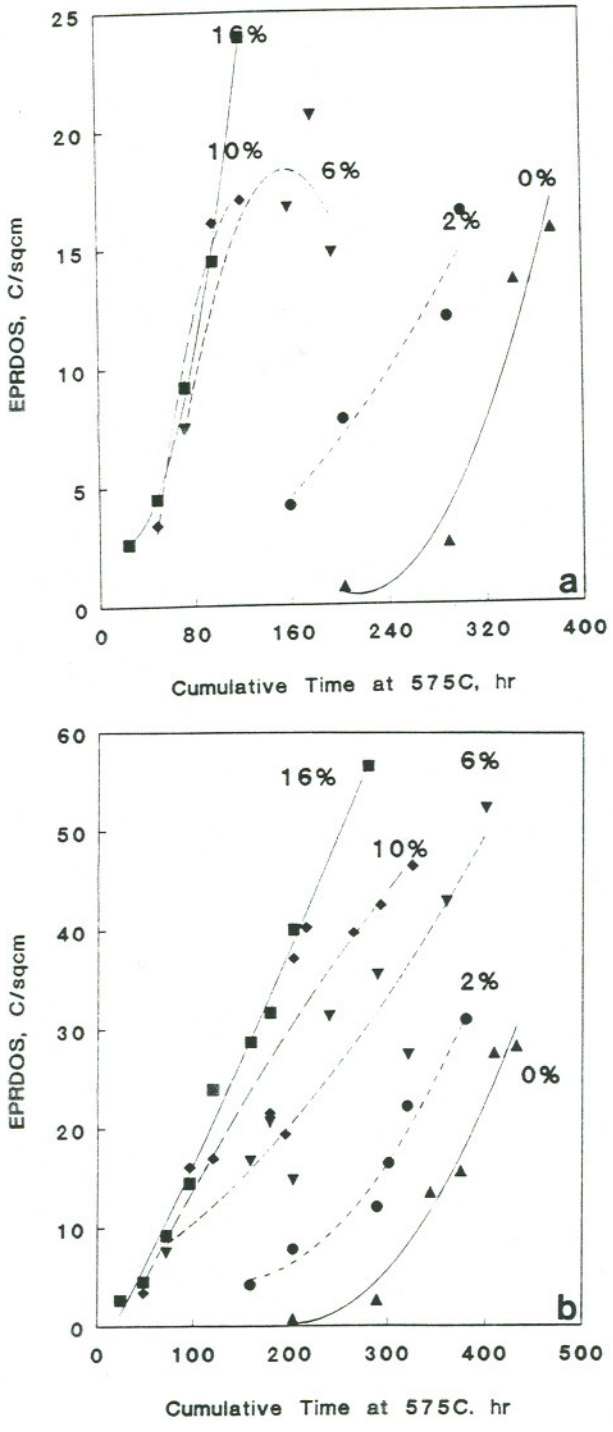

Figure 54. Strain effects on sensitization at 575°C for short (a) and long (b) times of heat treatment.

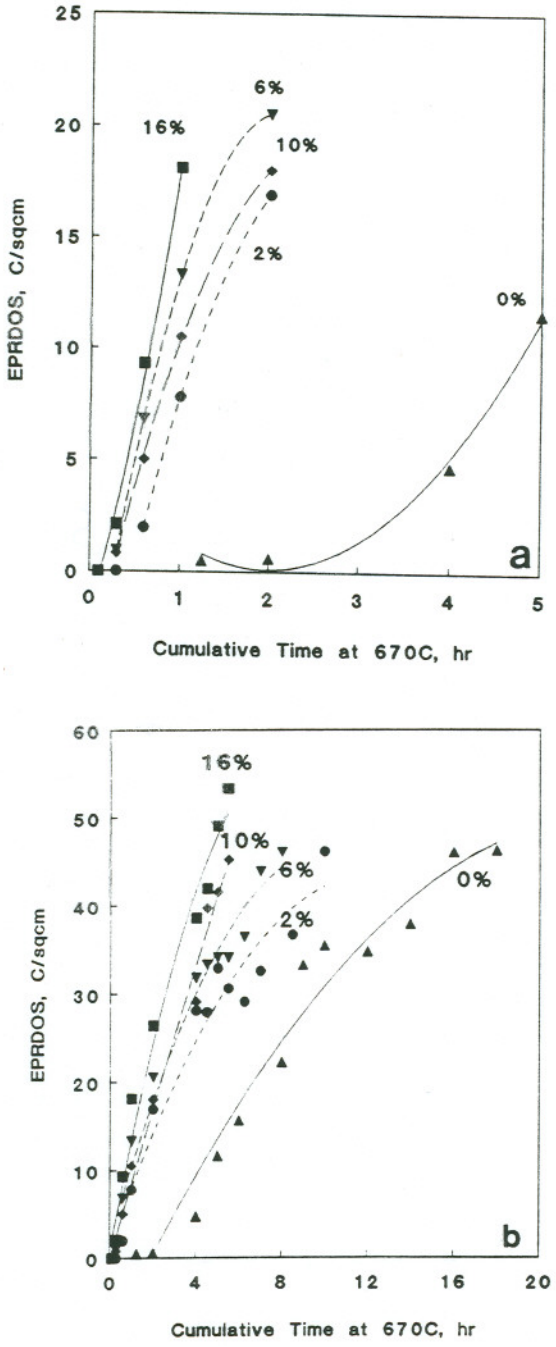

Figure 55. Strain effects on sensitization at 670°C for short (a) and long (b) durations of heat treatment.

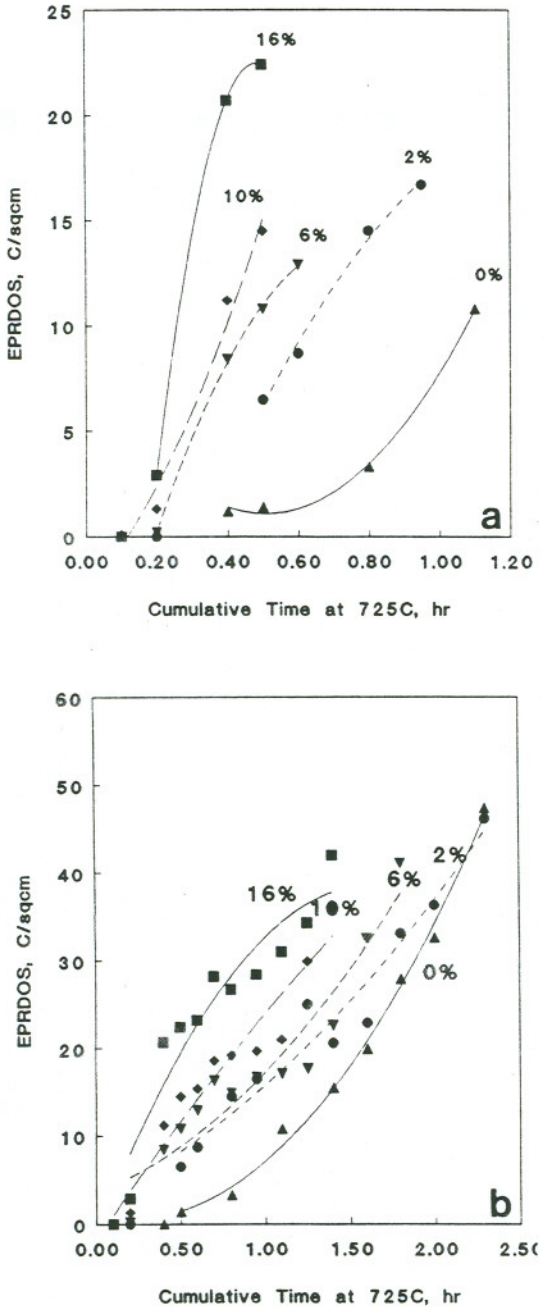

Figure 56. Strain effects on sensitization at 725°C for short (a) and long (b) durations of heat treatment.

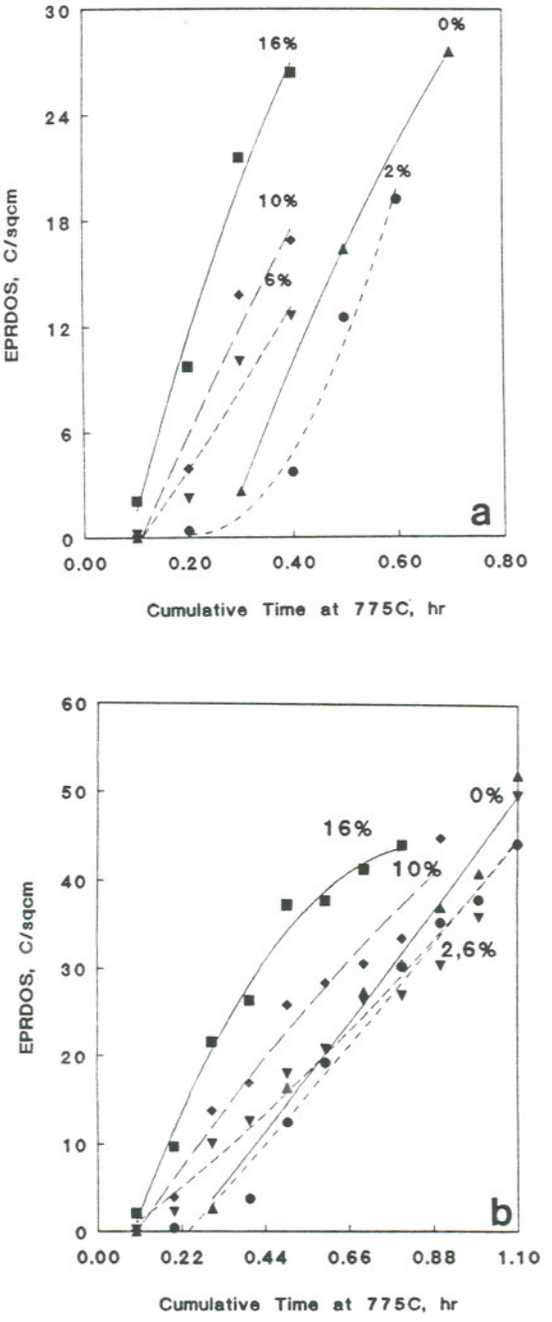

Figure 57. Strain effects on sensitization at 775°C for short (a) and long (b) durations of heat treatment.

The trends observed at 575°C and 670°C are in general agreement with those noted at 625°C. Generally, increased GBCD was observed through higher EPRDOS values with increasing strain above 2%. Specific treatment times which yielded these trends were, however, different at 575°C, 625°C and 670°C. The 575°C, unstrained material, for example, requires over 450 hrs to achieve an EPRDOS value of 30 C/cm^2 whereas a 575°C-16% strain material required only 150 hrs to produce the same EPRDOS. The same values were produced at lower times at 625°C and 670°C. At 625°C comparable EPRDOS values for the 0% and 16% strain specimens were developed after 5 hrs and 60 hrs respectively. This dropped to 2 hrs and 10hrs at 670°C.

At higher temperatures, the strain and temperature effects produced differences in GBCD development. At 725°C, there was a systematic increase in EPRDOS with strain at short times even at 2% strain, but at longer times the unstrained and 2% strain samples yielded similar values (Figure 56a,b). Acceleration in DOS with strain at long times was seen to be systematic only above the 6% deformation level at 725°C. At 775°C, no increase in DOS was seen up to 6% at short heat treatment times (figure 57a). For longer times, a strain of 10% had higher EPRDOS values than samples with strain of 0 - 6% which were similar (figure 57b). Above these strain

levels, continuous increases in DOS with strain similar to the short term data was still observed. These observations imply that strain-induced increases in sensitization is primarily at the short times, while longer treatments produce no effect for most samples and even show a decreasing effect of strain.

The fact that the short term effect is predominant at 725°C and 775°C is also reflected by microstructural evidence. At 625°C it may be recalled that differences in microstructure between 0% and 6% strain samples were seen at both short and long times of heat treatment. Increased grain boundary attack was seen in the 6% strain sample at short times, while increased twin boundary attack was noted at longer times. At 775°C, on the other hand, this difference was only seen for short times, where higher grain boundary attack was observed (Figure 58a). At longer times, the microstructure of the 0 and 6% material was similar with similar IG attack and no twin boundary attack was observed in either specimen (Figure 58b).

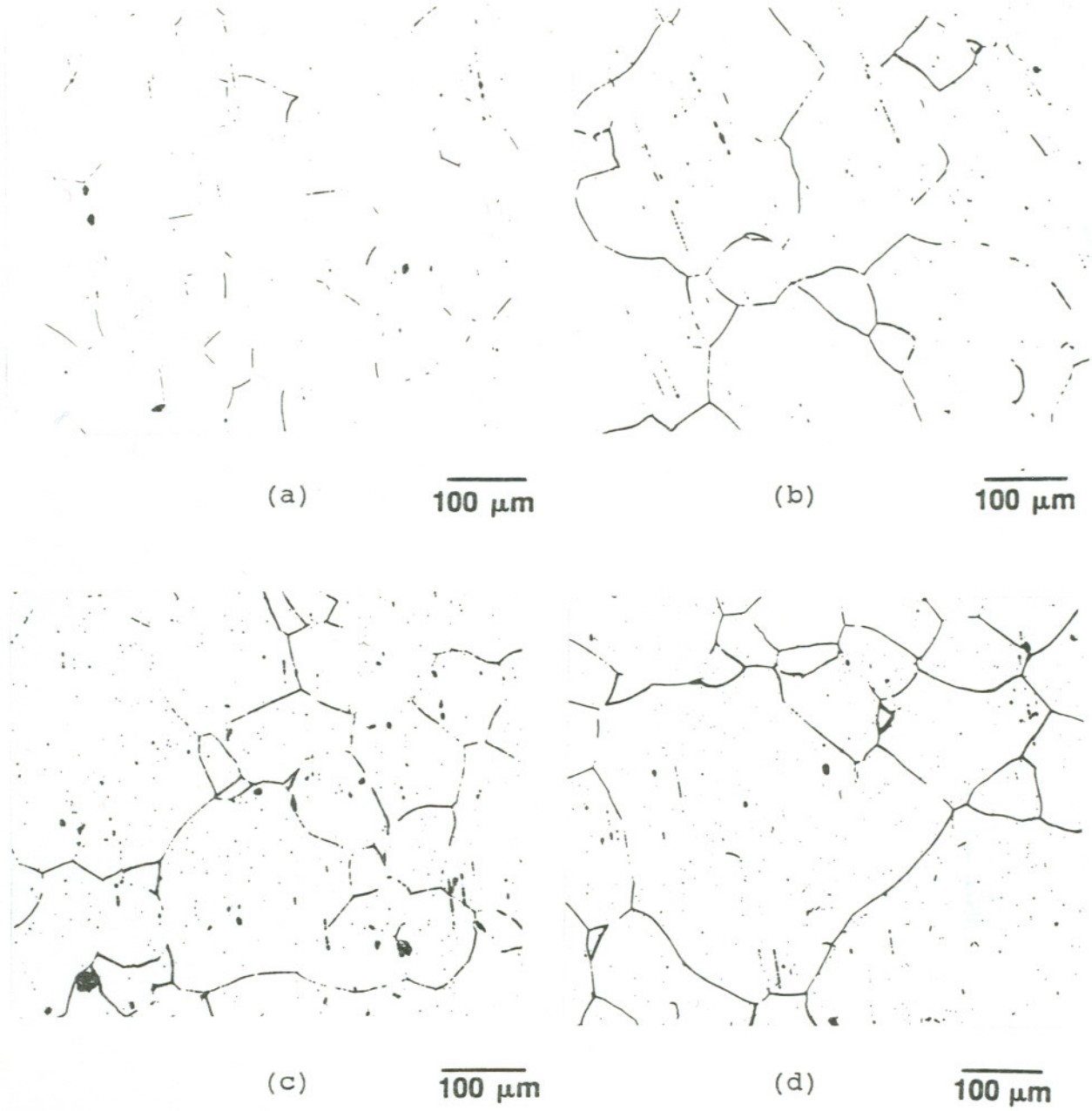

Figure 58. Microstructural comparisons of EPR etched surfaces indicating higher levels of intergranular attack on 6% strained versus unstrained specimens after short times of treatment at 775°C (a,b) and similar levels of grain boundary attack in the same conditions after longer heat treatments at 775°C (c,d).

The influence of temperature on relative importance of short term sensitization development is important. This is because it reflects the critical relationship among GBCD, prior strain and heat treatment. In general a decrease in deformation effects occurs at higher temperatures (above 725°C), although deformation still produces small increases in EPRDOS as evidenced by the unstrained and 10-16% strain data at 775°C.

The small increase in EPRDOS values between unstrained and 10% strained samples at 775°C was supported by optical examination of EPR etched surfaces, a comparison of which is shown at short and long times in Figure 59. The microstructures evidenced the presence of increased grain boundary attack in the 16% strain sample at short times, and similar grain boundary attack but higher twin boundary attack in the 16% strain sample at longer heat treatment times. The differences in microstructures between 0 and 16% strain samples at 775°C were, however, not as severe as at 625°C.

The (small) differences in EPRDOS between 0% and 10 - 16% at 775°C strain samples was not supported in qualitative TEM examination of carbide precipitation for unstrained and 16% strain samples at 775°C after 0.6 hrs of heat treatment (Figure 60). Continuous carbides (0.2 - 0.5 μm) were found

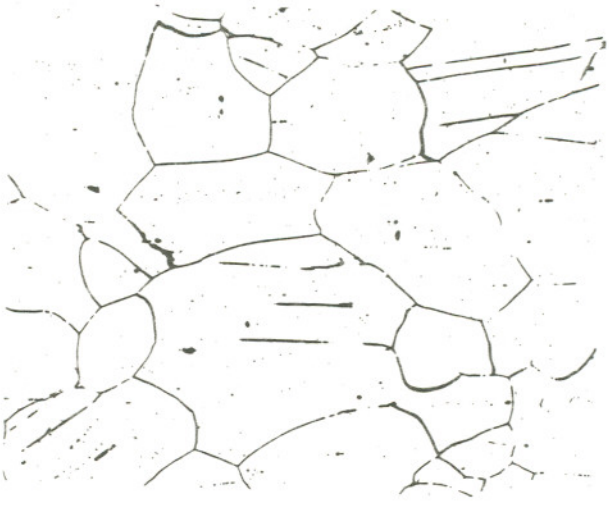

a

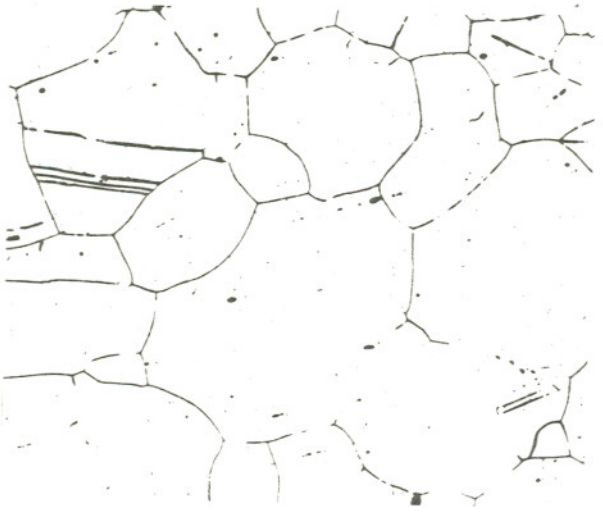

b

Figure 59. Comparisons of EPR test attack in unstrained and 16% strained samples at short and long times at 775°C. The EPR etched surfaces indicate differences in grain boundary attack between samples at short times (a) and similar intergranular attack but higher twin boundary attack in 16% versus unstrained samples at longer times (b).

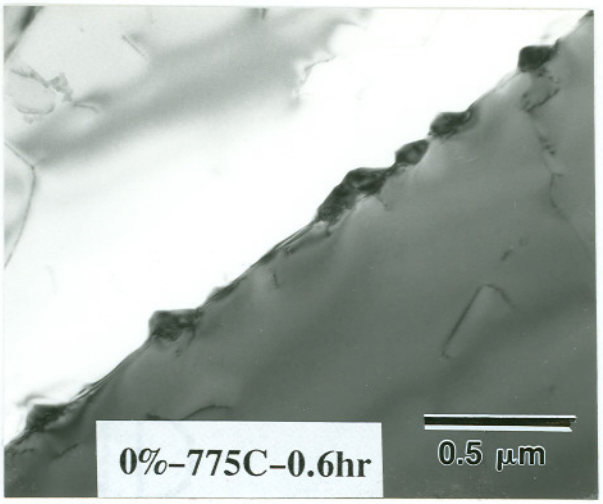

(a)

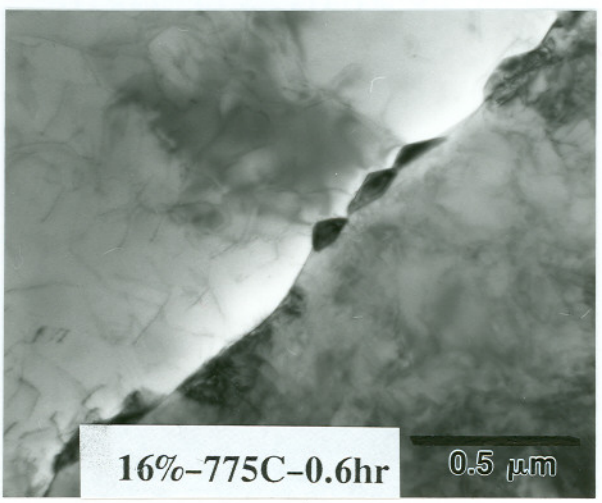

(b)

Figure 60. Transmission electron microscope comparisons of carbide precipitation in unstrained (a) and 16% strained specimens (b) after 0.6 hrs of heat treatment at 775°C.

on some grain boundaries but absent on others in both specimens. There may be quantitative differences in carbide densities for the two materials at this temperature which was masked by a simple qualitative examination. This was in contrast to the 625°C data where qualitative examination of carbide precipitation showed that carbides occurred on every boundary for the 16% strain samples after 20 hrs of treatment, while few carbides were present in the unstrained sample after a similar treatment.

Transgranular carbide precipitation was also noted in the 16% strain sample. This is evidenced in the optical micrograph of Figure 61 and bright field and dark field micrographs shown in Figures 62a and b. The optical micrograph shows that the TG attack partitions the grain along specific crystallographic directions, while bright and dark field TEM micrographs reveal that the TG carbides are confined to deformation bands intersecting one another and deformation bands intersecting annealing twins. The density of carbides at the intersection of annealing twins and deformation bands were observed to be much greater than other locations on the same boundary.

The entire database is represented in a three dimensional time-temperature-strain-sensitization (TTSS) diagram for the material (Figure 63). The plot essentially documents the

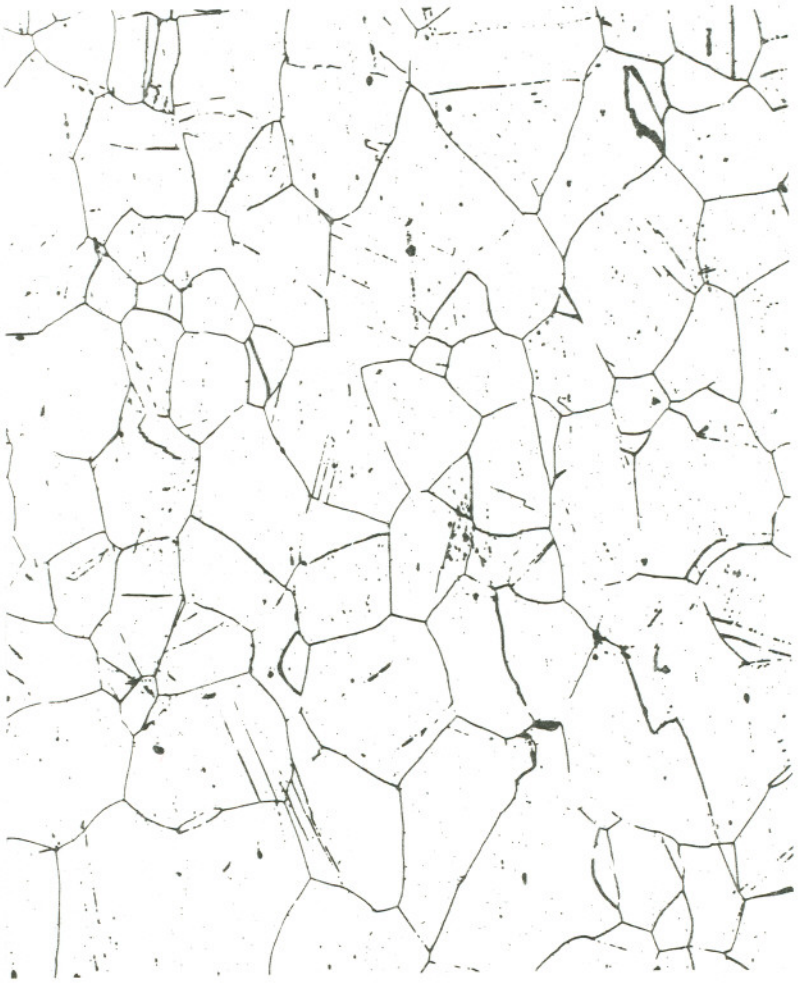

Figure 61. Optical micrograph of EPR etched surface revealing the presence of mixed intergranular and transgranular attack on the 16% strain specimen heat treated at 775°C for 0.6 hrs.

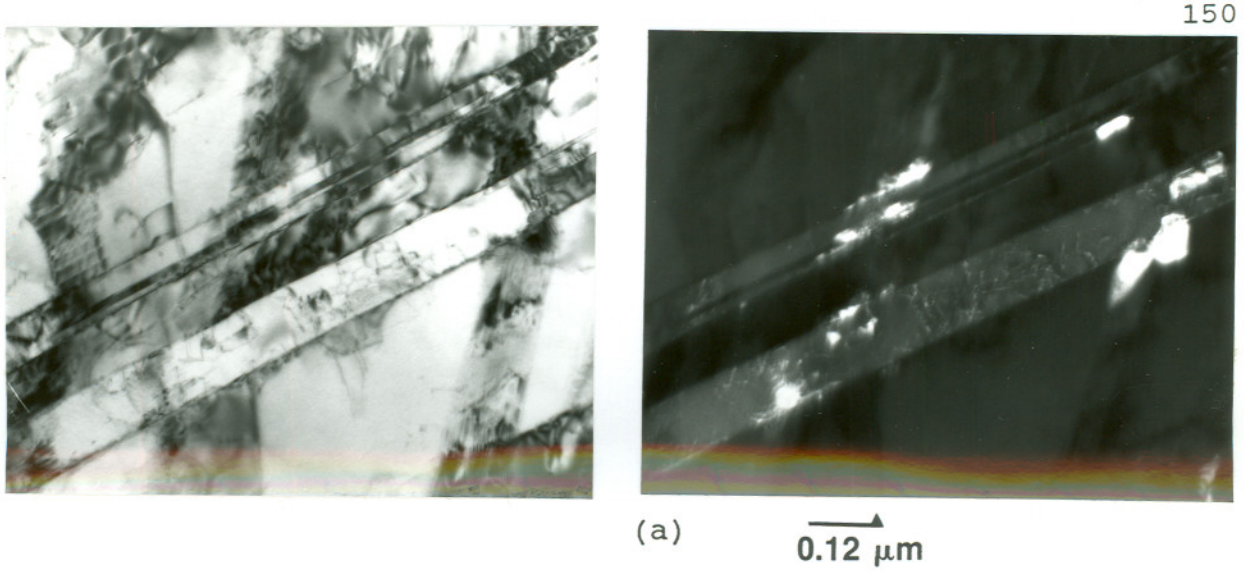

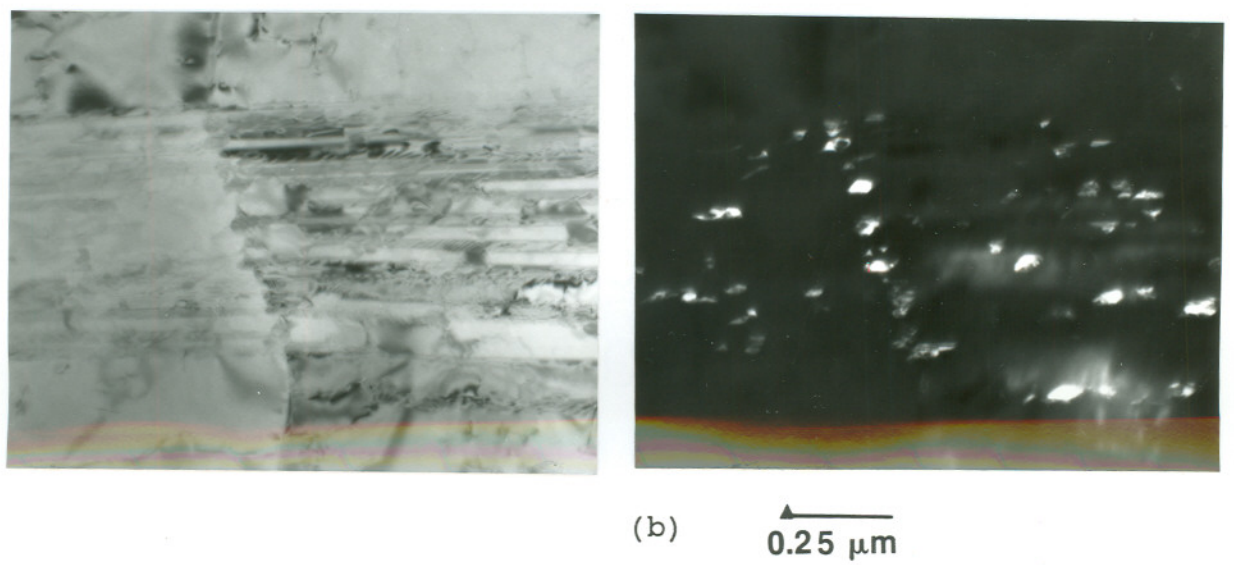

Figure 62. Bright field and dark field transmission electron micrographs documenting the presence of intragranular carbides at the intersection of deformation bands (a) and annealing twins intersecting deformation bands (b) for the 16%-775°C-0.6hr strained sample.

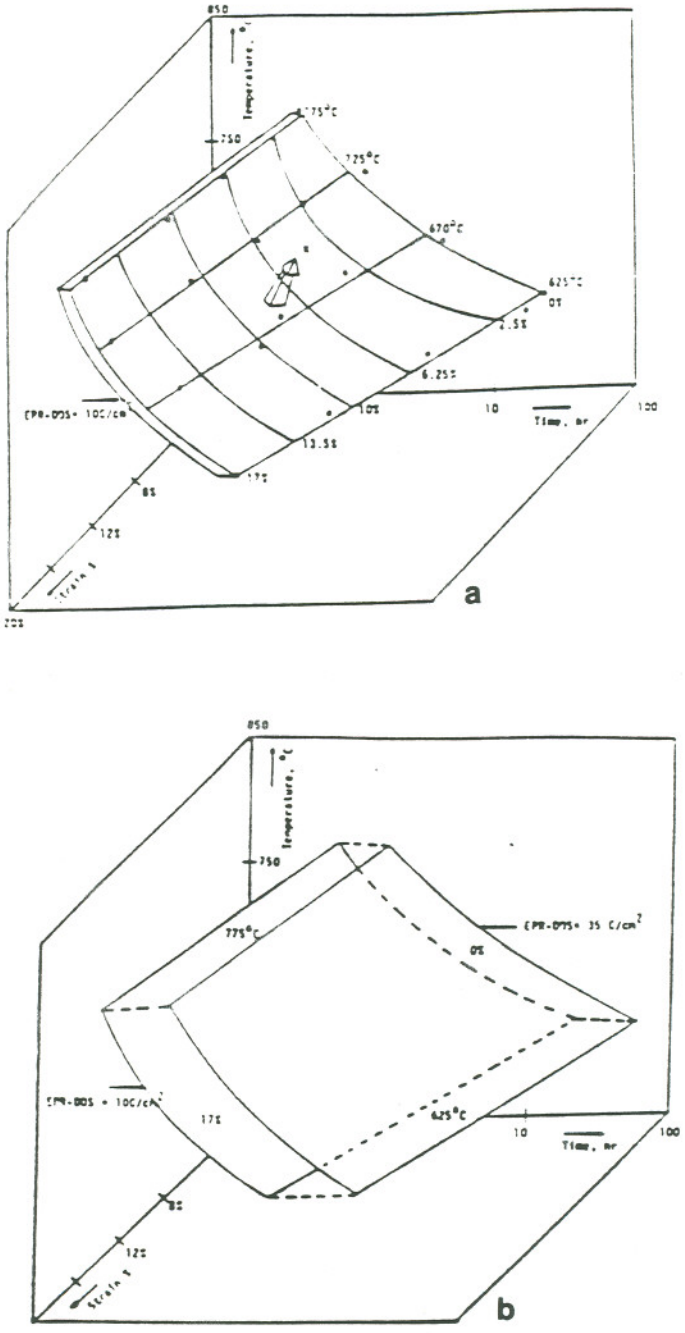

Figure 63. Three-dimensional time-temperature-strain sensitization diagram documenting the time, temperature and strain level required to achieve an EPRDOS value of 10 C/cm^2 (a) and the shift of EPRDOS surface from 10 C/cm^2 to 35 C/cm^2 (b).

time, temperature and strain level required to reach a DOS of 10 C/cm^2, and is an extension of the two dimensional time-temperature-sensitization (TTS) diagram. The TTSS diagram shows that at a given isotherm, the time required to achieve the DOS of 10 C/cm^2 decreases with increasing strain level. It also indicates that this effect is far more prominent at low temperatures, rather than high temperatures. At a constant strain line, the time required to achieve DOS is dependent on temperature and decreases with increasing temperature, as anticipated. Figure 63b also shows the movement of the iso-DOS surface from 10 to 35 C/cm^2 and indicates a shift to longer times to produce higher DOS levels for similar strain levels and temperatures of treatments.

TEMPERATURE EFFECTS ON HIGH STRAIN INDUCED SENSITIZATION

Transgranular attack on EPR tested surfaces was observed to have a time-temperature-strain dependence. Higher temperatures produced TG attack on strain specimens at shorter times of treatment. The attack also occurred primarily at strains above 20%, though 16% strain samples were also documented to show the presence of TG attack at longer times of heat treatment. The time-temperature-strain dependence of TG attack observed in this work is illustrated in Figure 64.

Only one material condition was examined by TEM in order to understand intra-grain carbide precipitation at higher temperatures (35%-670°C-10hrs). This was done because optical studies showed that this sample had extensive TG attack (Figure 65) and would be relatively easy to determine sites of precipitation within the grain. Transgranular attack on this sample was noted to be due to the presence of intra-grain carbides on matrix deformation structures, as documented at 625°C. A difference in the nature of defect preferred for precipitation in the 35%-670°C-10 hr specimen was, however, observed as compared to that at 625°C.

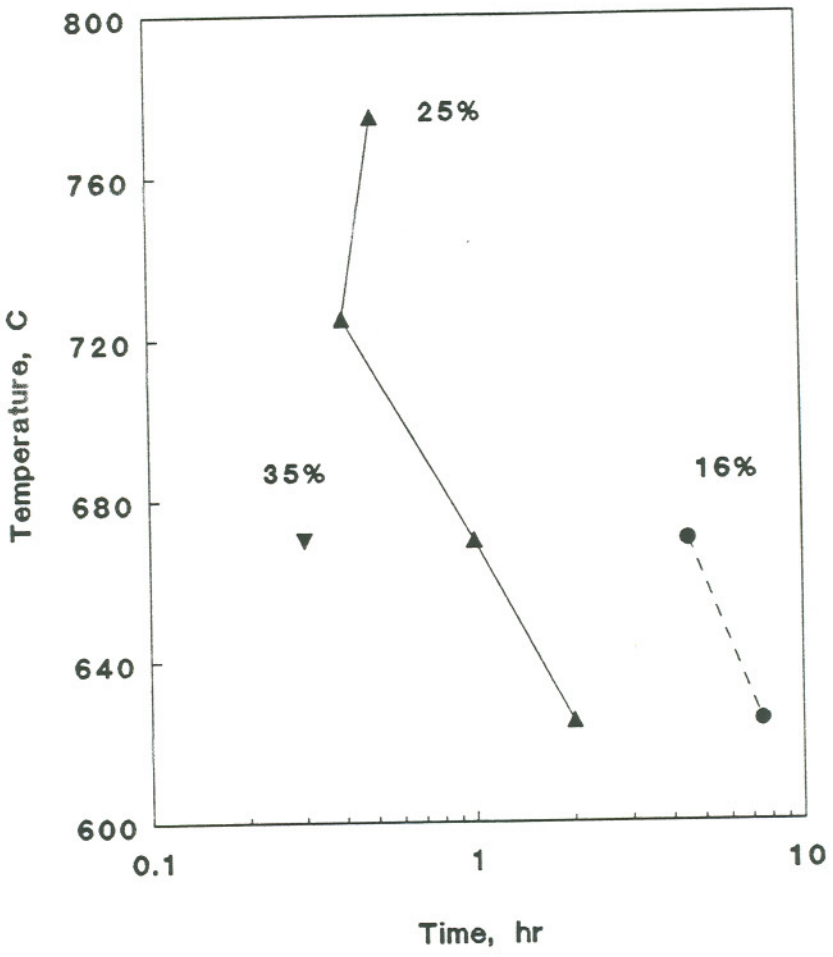

Figure 64. Time-temperature-strain effects on the induction of transgranular attack in Type 316 stainless steels. This diagram was developed by careful examination of optical micrographs for each sample to document the first time at which TG attack occurred on each material.

Figure 65. Optical micrograph documenting extensive transgranular attack seen on the 35% strain sample after 10 hrs of heat treatment at 670°C.

At 625°C intragranular carbides were observed to be present within dislocations and at planar array intersections. In this specimen, however, it was seen that the carbides tended to be confined to the twin-faulted regions and their intersections. A typical example is seen in the TEM micrograph documenting moire fringe patterns due to carbides within a twin-faulted region (Figure 66).

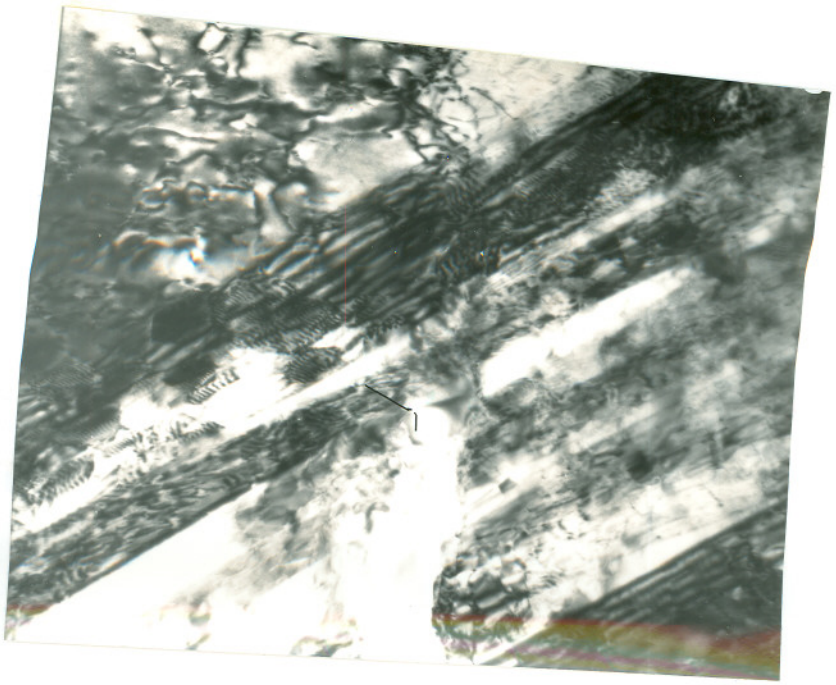

(a) 0.1 μm

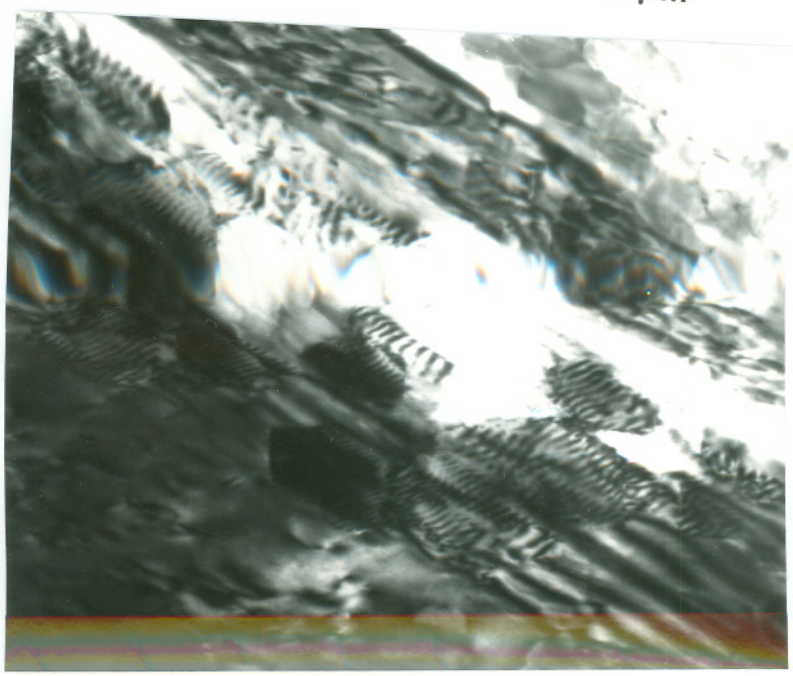

(b) 0.1 μm

Figure 66. Transmission electron micrographs showing low (a) and high (b) magnification views of carbide precipitation within a twin faulted region for the 35% strain specimen after heat treatment for 10 hrs at 670°C.

CHAPTER 5

FUNDAMENTAL EVALUATION AND MODELING OF DEFORMATION EFFECTS ON GRAIN BOUNDARY CHROMIUM DEPLETION

TASK ANALYSIS

Critical experiments performed in the previous section have shown that deformation produces accelerated GBCD development in SS. The acceleration was seen through continuous increases in EPRDOS, IG attack and carbide precipitation with systematic increases in strain. This agrees well with similar observations made by other researchers[44-48,50-55].

Current research has provided a better insight into the effects of strain magnitude and heat treatment temperature and time on GBCD. This is an important step leading towards a fundamental understanding of the strain-induced GBCD development. Observations of increased twin boundary attack on strained samples, intragranular carbide precipitation leading to a time-temperature-strain dependent TG attack and deformation structural changes with strain are other important findings made in this work which need to be tied into the overall understanding of strain effects on the GBCD phenomena.

In this chapter an analytical method was developed to evaluate the thermodynamic and kinetic effects of strain on GBCD. The thermodynamic and kinetic effects have been correlated with the deformation structures on as-strained samples to indicate

mechanisms of strain induced GBCD development. Strain - GBCD theories are also incorporated into a recently developed strain-sensitization model[56] to improve the theoretical basis and predictive capability of the model.

ANALYTICAL METHODS FOR THERMODYNAMICS AND KINETIC EVALUATION OF GRAIN BOUNDARY CHROMIUM DEPLETION

GBCD KINETICS EVALUATION METHOD

Chromium diffusion measurements were made from EPRDOS versus heat treatment time data in the range where the influence of nucleation and desensitization are secondary and EPRDOS is controlled by the $\sqrt{Dt}$ width of chromium depleted zone. Assuming that the influence of nucleation and desensitization are secondary beyond the time to start the EPRDOS curve (t_0) and below 50C/cm^2 for the specimens examined, EPRDOS-time from 0 to 50C/cm^2 was considered diffusion dependent and used to determine chromium diffusivity.

Evaluation of the diffusivity was carried out by comparing experimentally measured and theoretically predicted slopes of the EPRDOS versus $\sqrt{t-t_0}$ data below 50 C/cm^2 using Fortran F-77 software developed for the purpose (Appendix 1A). Normalization versus $\sqrt{t-t_0}$ was necessary to encounter time offsets for strained versus unstrained specimens induced by strain effects on t_0. Slope data was used rather than (raw) EPRDOS data to reduce effects of scatter occurring in EPRDOS values during test measurements.

The algorithm required as input the experimentally obtained EPRDOS versus time data, and the t_0 value. Every EPRDOS value corresponding to times above t_0 was normalized with respect to t_0, and the square root of the $(t - t_0)$ value was then computed. Linear regression of the EPRDOS - $\sqrt{t-t_0}$ values was then carried out, and the slope of the curve was taken as the regression coefficient of the fitted - line. Correlation coefficients computed during regression analysis were determined to be better than 95%, indicating a good fit to the EPRDOS versus $\sqrt{t-t_0}$ data sets.

Theoretical slope determination involved a trial and error method. A diffusivity value was assumed by the algorithm and used to compute widths (W_{atk}) and volume parameter VP of chromium depletion at the chromium attack level (Cr_{atk} = 13.5%[56]). Widths at the attack level were computed as a function of isothermal treatment time (t) at temperature using the Thorvaldasson modified[66] solution to Fick's second law of diffusion

$$(Cr_{atk} - Cr_{min}) = (Cr_{bulk} - Cr_{min})\ erf\ (W_{atk}/2\sqrt{D_{cr}t})$$

Volume parameter (VP) of chromium depletion below 13.5% Cr level was calculated using the normalized equation[56]

$$VP_{13.5} = \frac{(13.5 - Cr_{min}) * W_{atk}}{(2 * 13.5)}$$

The Cr_{min} value used in this computation was taken as a direct output of the sensitization model developed by Bruemmer[56].

EPRDOS values were subsequently computed using the correlation between EPRDOS and VP[56]

$$EPRDOS = 1.1*VP - 6.1E-3*VP^2 + 1.3E-5*VP^3$$

Each calculation was performed for a series of time values at each diffusivity. Slopes of EPRDOS versus $\sqrt{t}$ curves for EPRDOS values below 50 C/cm^2 were compared with those obtained in the experiment, until a diffusivity value that provided identical slopes as the experiment was output by the algorithm.

GBCD THERMODYNAMICS EVALUATION METHOD

Thermodynamic effects of strain were determined using the time to start the EPRDOS curve, t_0, as an indicator of nucleation time t_n. The t_n value was subsequently used to compute strain effects on the thermodynamic barrier to nucleation, ΔG^*, and changes in interfacial energy caused by nucleation, ΔG_{gb}, using Fortran F-77 software provided in Appendix 1B.

The start of sensitization requires nucleation of carbides followed by development of a (minimum) volume of chromium depletion on the grain boundary. Nucleation times were, thus, evaluated as

$$t_0 = t_n + t_{depl}$$

where t_{depl} = time to form a minimum volume of chromium depletion on the grain interface

Correlations developed between STEM-EDS observations of chromium depletion at the grain boundary and EPRDOS have indicated that a minimum chromium level below 13.5% and width of chromium depletion above 25Å[56] are typically required to develop attack in the EPR test. The t_{depl} term was calculated as the time (in hours) required to establish a 25Å depletion width at the 13.5% attack level by first converting it to the

width of depletion at the bulk chromium level (W_{bulk}) using the equation[66]

$$(13.5-Cr_{min}) = (Cr_{bulk}-Cr_{min})\,erf(25x10^{-8}/W_{bulk})$$

Values of Crmin were taken as output from the model of Bruemmer[56]. The W_{bulk} value was used to determine t_{depl} and t_n through

$$t_{depl} = (W_{bulk})^2/(3600 \times 4D_{cr})$$

$$t_n = t_0 - (W_{bulk})^2/(3600 \times 4D_{cr})$$

The nucleation time was related to the thermodynamic barrier to carbide nucleation and activation barrier to chromium diffusion Q_a using the approach of Logan and Grobner (Chapter 1). This yields

$$t_n = k \exp \frac{Q_a}{RT} \exp \frac{\Delta G^*}{RT}$$

and requires knowledge of k and Q_a to determine the ΔG^* value.

The value of k has been determined empirically by Bruemmer[56] as

$$k = 3.1 \times 10^{-17}/CW$$

where CW = modified carbon equivalent for SS

This computes to a value of 5.17×10^{-16} for the 0.058 wt% carbon Type 316 SS used in this work.

Evaluation of the Q_a value for precipitation of carbides on the grain boundary needs consideration of diffusion of chromium via matrix versus the grain boundary to the precipitate. The value for Q_a, therefore, depends on the relative importance of the two parameters and determination of the one which is rate limiting. This point has been debated by numerous researchers who considered the grain, grain boundary and mixed contributions from both regions in models for nucleation of grain boundary precipitates. In this work both grain boundary and matrix diffusion rates were employed to model ΔG^* to compare and possibly establish the relative importance of these two terms.

The alteration in ΔG_{gb} due to grain boundary precipitation was obtained through the ΔG^* value, assuming that the driving force ΔG_v and surface energy barriers for nucleation ΔG_s are unaffected by strain. For the (simplest) grain boundary nucleus shape this is given by[77]

$$\Delta G^* = \frac{16\pi\ \Delta G_s^3}{3\ \Delta G_v^2} \left(\frac{2 - 3\ \mathrm{Cos}\Theta + \mathrm{Cos}^3\Theta}{2}\right)$$

$$\text{where}\quad \mathrm{Cos}\Theta = \frac{\Delta G_{gb}}{2\Delta G_s}$$

and required a trial and error solution to yield the value of ΔG_{gb}. The value of ΔG_s was assumed to be 172 cals/mole[56,63], while ΔG_v was obtained using the empirical equation[56]

$$\Delta G_v = 0.1\ T - (110 + CW * 150 + 4 * Mo)$$

where T = Temperature in degree Kelvin
CW = Adjusted carbon content of SS (weight%)
Mo = Molybdenum content of SS

This yields

$$\Delta G_v = 0.1\ T - 127.7 \quad \text{cals/mole}$$

for the Type 316 SS being examined in this work.

THERMODYNAMIC AND KINETIC EVALUATION OF DEFORMATION EFFECTS ON GRAIN BOUNDARY CHROMIUM DEPLETION

STRAIN EFFECTS ON GBCD KINETICS

The algorithm required EPRDOS versus time and t_0 data as an input to compute diffusivity. The experimental EPRDOS versus time data was obtained directly from Chapter 4. Determination of an accurate t_0 for each data set was, however, difficult as it required a lot of data in the short range of the EPRDOS-time curve. An estimate of t_0 was instead obtained by extrapolating the trends seen in the short-term EPRDOS values to the EPRDOS = 0 axis (Table 5). Although this method does not yield exact t_0 values, changes in this parameter do not significantly affect trends developed for strain effects on the phenomena.

A typical plot of experimentally developed EPRDOS versus $\sqrt{t}$-t_0 curve for an unstrained specimen heat treated at 625°C is illustrated in Figure 67. The graph shows an excellent linear correlation between experimental EPRDOS values and $\sqrt{t}$-t_0, with a correlation coefficient of 0.99 for the regressed line drawn through the data. A small offset from the origin is, however, seen on the root-time axis. This offset is not expected if the

Table 5. Variation of times to start sensitization (t_0), experimental slopes and chromium diffusivities as a function of strain and heat treatment

Temp C	Strain %	t0 hr	Slope C/cm2/√hr	Diffusivity cm^2/sec
575.0	.00	200.000	1.7136	0.23E-17
575.0	2.00	100.000	1.6354	0.21E-17
575.0	6.00	60.000	2.4819	0.50E-17
575.0	6.00	40.000	2.8743	0.68E-17
575.0	16.00	10.000	3.4433	0.99E-17
625.0	.00	15.000	5.2243	0.27E-16
625.0	2.00	3.000	6.2952	0.40E-16
625.0	6.00	1.500	6.7121	0.46E-16
625.0	10.00	0.750	9.7579	0.97E-16
625.0	16.00	0.250	11.7969	0.14E-15
670.0	.00	1.800	13.0800	0.22E-15
670.0	2.00	0.500	14.2349	0.26E-15
670.0	6.00	0.200	16.8727	0.37E-15
670.0	10.00	0.200	20.4060	0.54E-15
670.0	16.00	0.150	23.3673	0.71E-15
725.0	.00	0.350	29.7010	0.18E-14
725.0	2.00	0.300	30.7435	0.19E-14
725.0	6.00	0.199	26.0852	0.14E-14
725.0	10.00	0.150	29.5801	0.18E-14
725.0	16.00	0.100	35.5865	0.26E-14
775.0	.00	0.280	53.4865	0.11E-13
775.0	2.00	0.180	47.6421	0.91E-14
775.0	6.00	0.120	45.8398	0.84E-14
775.0	10.00	0.120	49.3368	0.97E-14
775.0	16.00	0.080	57.6493	0.13E-13

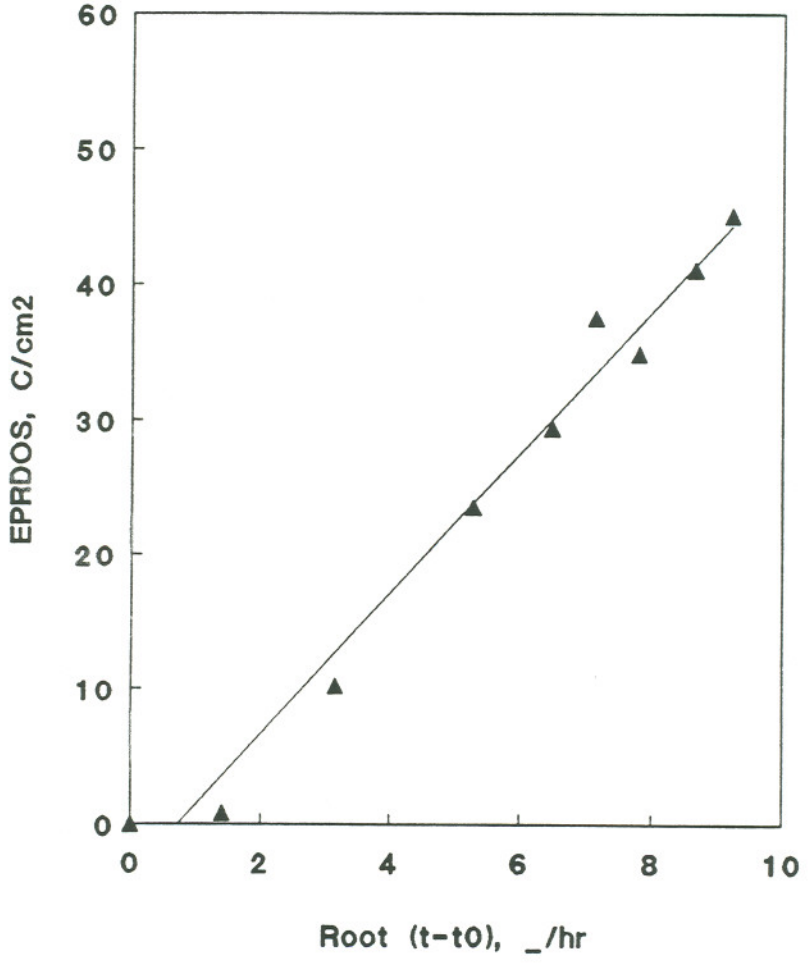

Figure 67. Variation of EPRDOS versus root time at 625°C for unstrained specimens.

correlation between EPRDOS and root time is ideally related to diffusivity. However, in lieu of the fact that the data is experimental and may have contributions from nucleation and healing, the presence of the offset is not surprising. Implications of the offset were neglected in computation of the slope.

Similar computations for other strain and heat treatment conditions yielded experimental slopes and chromium diffusivity values for the entire data set, which are summarized in Table 5, and Figures 68 and 69 respectively.

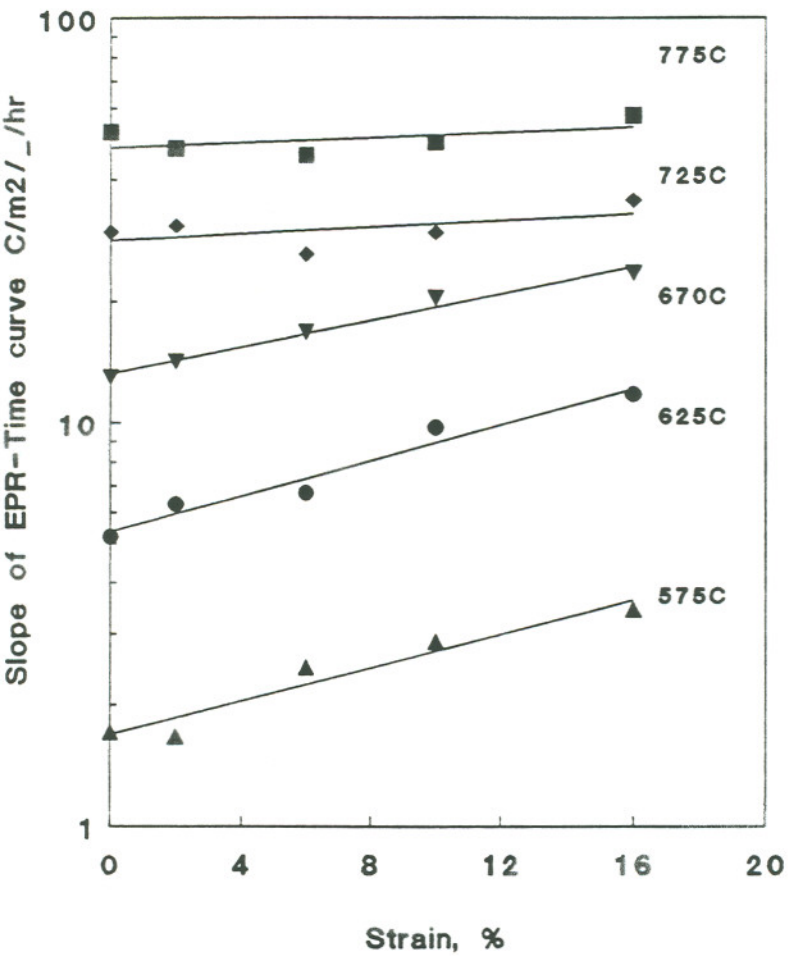

Figure 68. Strain effects on EPR test slope as a function of temperatures from 575°C to 775°C.

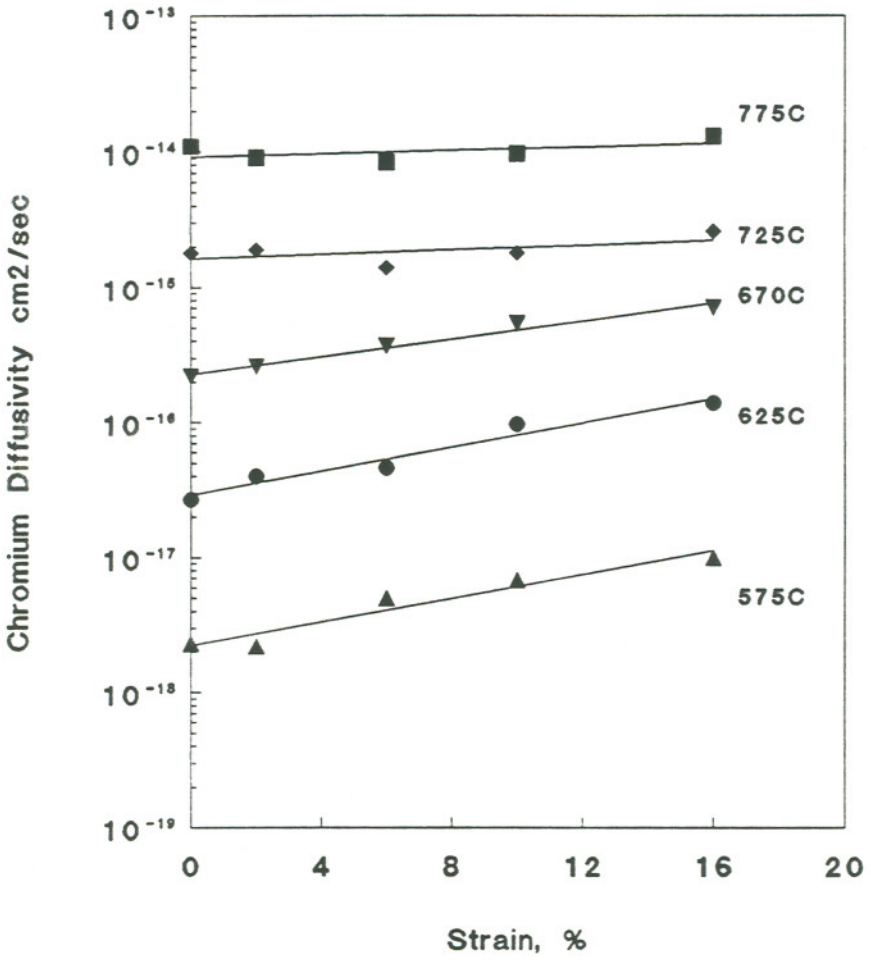

Figure 69. Chromium diffusivity predictions from EPR test slope data for 0 - 16% strain and 575°C -775°C.

The data from table 5 and Figure 68 illustrate that the slope increases systematically from 2 $C/cm^2/\sqrt{hr}$ to 4 $C/cm^2/\sqrt{hr}$ at 575°C for 0% to 16% strain. Similar increases in slope are also obtained at 625°C and 670°C, though the magnitude of increase in slope is higher at these temperatures, as compared to 575°C. The slope data at 725°C and 775°C appear to be scattered around 35 $C/cm^2/\sqrt{hr}$ and 60 $C/cm^2/\sqrt{hr}$, and no systematic correlation between slope and strain is seen at these high temperatures.

Conversion of the slope data to diffusivity yields trends similar to those observed in Figure 69. At 575°C the predicted diffusivity increases by about an order of magnitude from 2 x 10^{-18} to 1 x 10^{-17} cm^2/sec with increase in strain from 0% to 16%. The diffusivity is also similarly seen to increase by an order of magnitude from 0% to 16% strain at 625°C. but reduces to only a factor of 3 at 670°C for the same strain levels. At 725°C and 775°C the predicted diffusivities were relatively constant at 2 x 10^{-15} and 1 x 10^{-14} cm^2/sec respectively for all strain levels.

The increase in diffusivity with increasing strain substantiates the systematic increases in EPRDOS, IG attack and carbide precipitation seen with strain from 575°C to

725°C. The relatively constant diffusivity obtained above 725°C, on the other hand, indicates that the lower levels of acceleration in GBCD development seen at 725°C and 775°C is due to a thermodynamic influence. This agrees well with the fact that the increase in sensitization development observed at these temperatures was apparent in the short term EPR data (which are thermodynamic dependent) while the long term data (which is diffusivity dependent) produced no further acceleration in DOS.

Diffusion equations for each of the strain levels were obtained by developing Arrhenius plots of log diffusivity versus inverse temperature for each material. The activation barrier to diffusion was given by the slope of the Arrhenius plot using Q_a = Slope x R, while log D_o was obtained as the y-intercept of the curve.

The Arrhenius plot for the unstrained specimen is illustrated in Figure 70. This plot shows an excellent linear fit between log diffusivity and inverse temperature, as would be expected. The diffusion equation computed for the annealed material was 50 exp (-76000/RT).

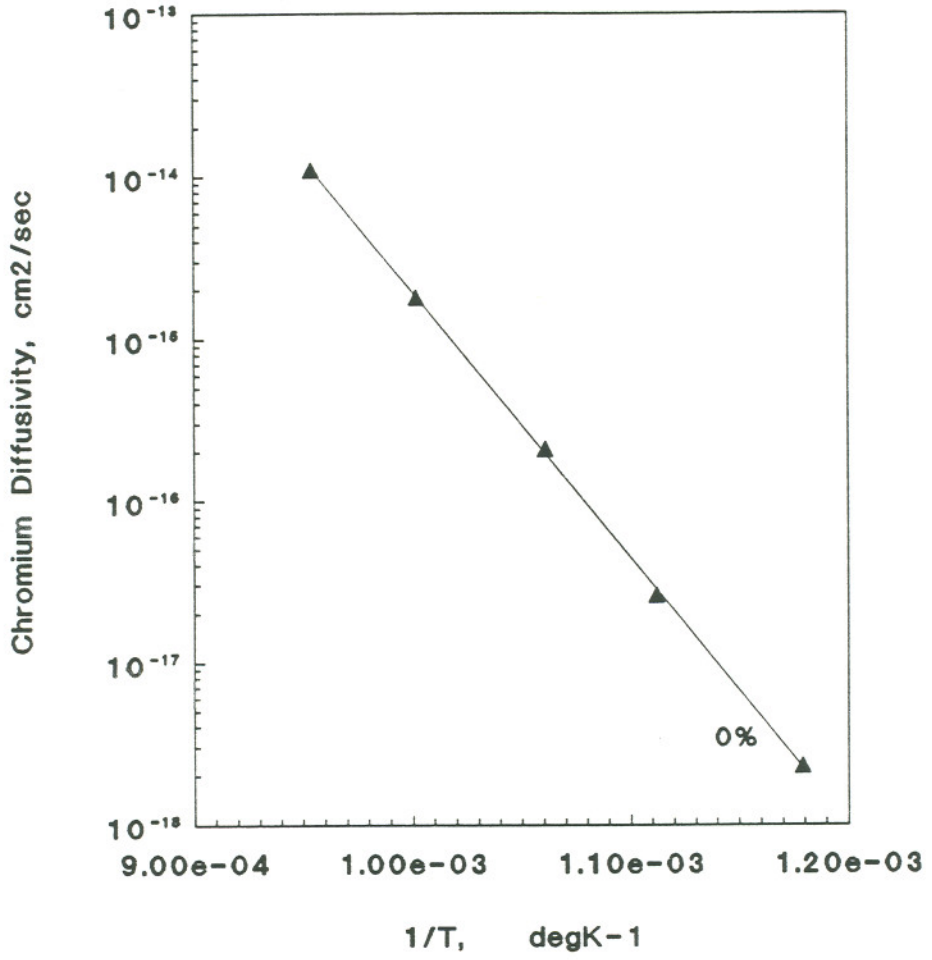

Figure 70. Arrhenius plot of log diffusivity versus strain for the unstrained 1100°C-1hr solution annealed Type 316 SS.

The Arrhenius curves for strained materials are shown in comparison to the unstrained material in Figure 71a-d. The plot for the 2% strain material illustrates the smallest acceleration in kinetics, as compared to the annealed material. The curve is close to, has a lower slope and merges with the curve for the unstrained sample at 670°C. The Q_a was determined to be - 74000 cals/mole/°K, while D_o was measured to be 20 cm^2/sec. Increasing strain to 6% resulted in a further increase in diffusivity, though the unstrained and 6% strained plots merged at approximately 700°C. The diffusion equation of this material was computed to be 0.3 exp (-65000/RT).

Further increases in the strain to 10% and 16% also resulted in lowering the slopes and raising the temperature at which unstrained and strained Arrhenius plots merged (750°C and 775°C respectively). This implies that increasing strain accelerates sensitization development to a larger extent and results in higher temperatures up to which the acceleration is seen. Diffusion equations computed for the 10% and 16% strained samples were determined to be 0.3 exp (-64000/RT) and 0.1 exp (-62000/RT) respectively.

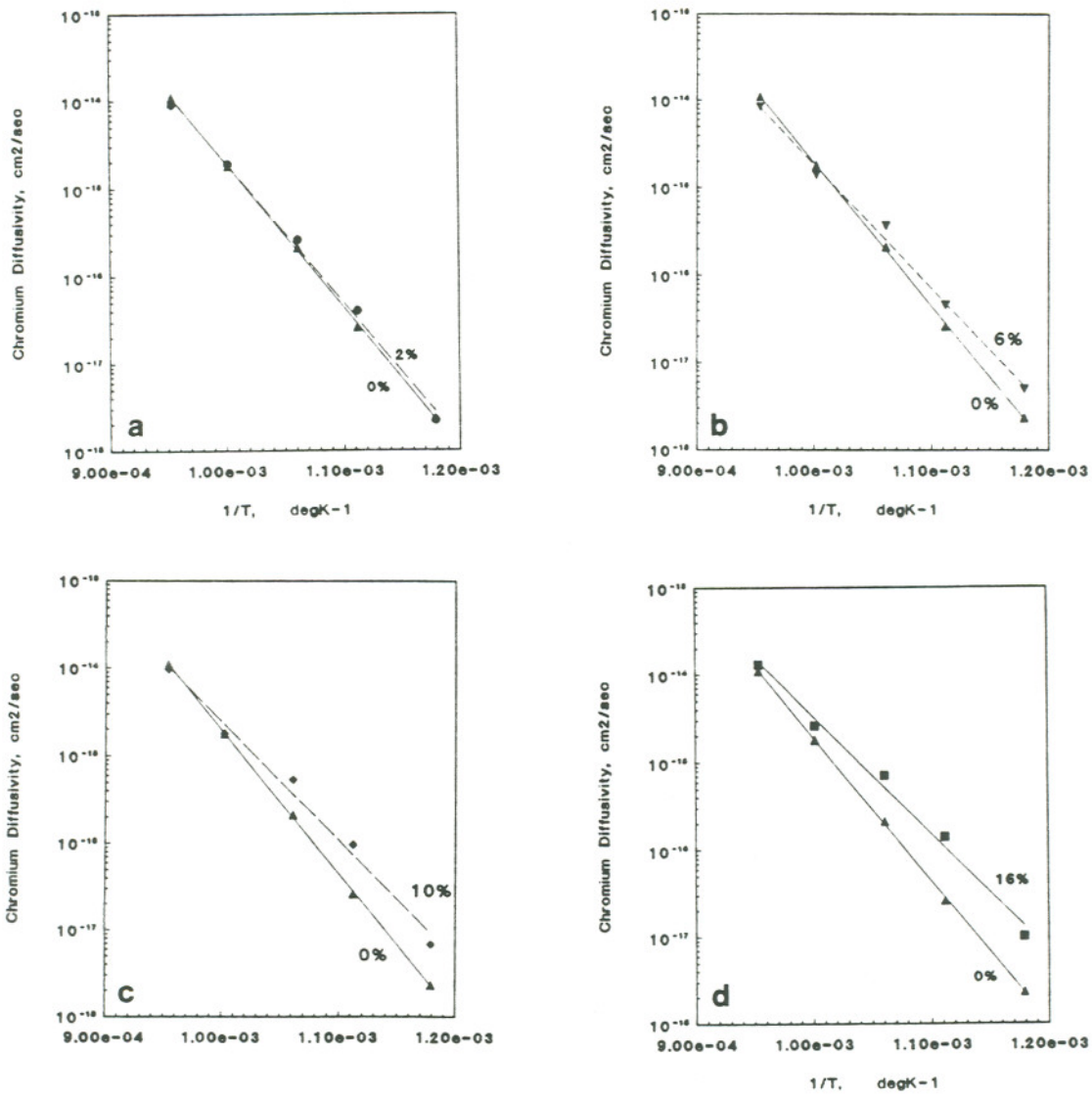

Figure 71. Arrhenius plot of log diffusivity versus inverse temperature (Kelvin) for 2% strain (a), 6% strain (b), 10% strain (c) and 16% strain (d) data sets.

A summary of the entire series of Arrhenius plots and a comparison of diffusion equations for the different strain levels is shown in Figure 72 and Table 6.

Table 6. Comparison of diffusion equations computed for the unstrained and strained materials with available literature

Strain Level %	Diffusion Equations From Arrhenius Plot cm^2/sec	Literature Diffusion Equations cm^2/sec
0%	50 exp(-76000/RT)	Matrix
2%	20 exp(-74000/RT)	1 exp(-67000/RT)[63]
6%	0.3 exp(-65000/RT)	0.3 exp(-63900/RT)[97]
10%	0.3 exp(-64000/RT)	Grain Boundary
16%	0.1 exp(-62000/RT)	1 exp(-44000/RT)

The plot of Figure 72 illustrates the systematic lowering of slopes, and increased temperatures at which the merging of the strained and unstrained Arrhenius curves occur with increasing strain. A comparison of the diffusivity values in the Table 6 also indicates that the Q_a and D_o values are both decreased with increasing strain. The decrease in Q_a values with strain is in qualitative agreement with the theory proposed by Christian[31].

The diffusion equation for chromium diffusivity in austenitic SS taken from averages of experimental works available in the literature[63] is also shown in Table 6. A comparison of the

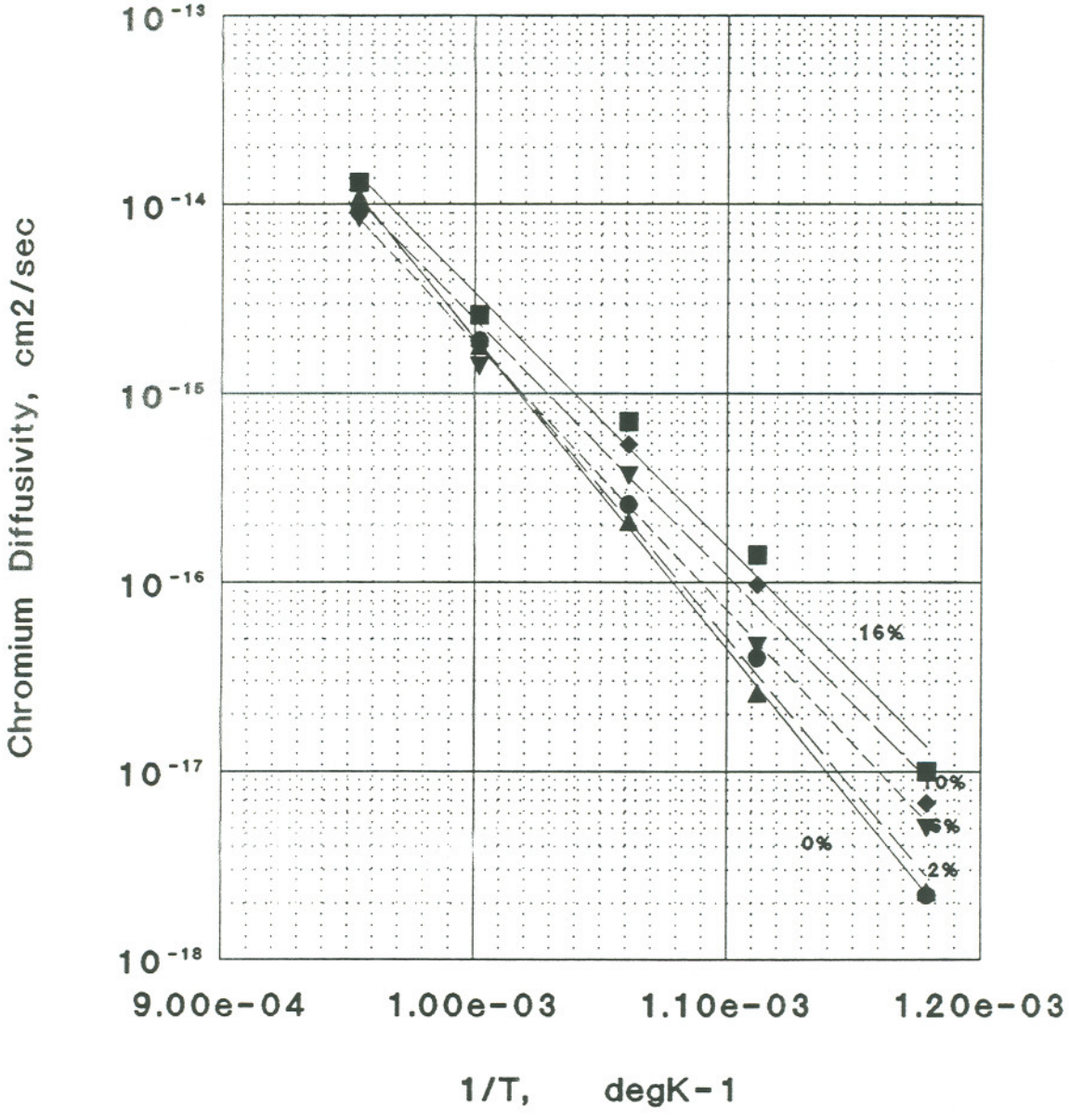

Figure 72. Strain effects on chromium diffusivity as illustrated by comparisons of Arrhenius curves for materials strained to different levels.

diffusion equation obtained in this work versus the average value available in the literature indicates a slightly higher D_o and Q_a value for the equation developed in this work. However, in lieu of the fact that the literature diffusion equation is an average value extrapolated from high temperature work, the diffusion equation computed in this work was considered to have good agreement with that in the literature.

A comparison of the diffusion equation for the 16% strained sample and average grain boundary diffusion coefficient for chromium in austenitic SS[63] (Table 6) indicates that the value of Q_a at 16% strain is higher, while D_o is lower than that for grain boundary diffusion. An important point to noted is that the magnitude of decrease in the Q_a for lattice versus grain boundary diffusion for the average SS is similar to the difference between Q_a for lattice versus 16% strain materials used in this work. This indicates that at about 16% strain, the bulk diffusivity due to dislocation pipe diffusion tends to occur in a manner similar to that for grain boundary diffusion. This is possibly due to overlapping of individual dislocation pipes at high strains leading to formation of continuous paths for enhanced diffusion, similar to that present in the grain boundary.

STRAIN EFFECTS ON GBCD THERMODYNAMICS

The start of sensitization t_0 values documented in Table 5 were plotted in Figures 73a and b to better illustrate the effects of strain and temperature on the t_0 value. The plot of Figure 73a illustrates that strain produces a systematic decrease in t_0 at all temperatures. The decrease is seen to be about an order of magnitude at 575°C and 625°C, while smaller decreases are noted at higher temperatures. A decrease in t_0 is also noted with increasing temperature at each strain level, and the trends in each curve are similar for each strain level. The decrease between the lowest (575°C) and highest temperatures (775°C) for every strain level is between 2 - 3 orders of magnitude, which would be expected considering that the kinetics of reactions, in general, double for every 10°C rise in temperature.

Computations of the t_{depl} values for each temperature indicated that this term was insignificant in comparison to t_0. The conversion of the t_0 values to the t_{nuc} turned out to be, therefore, only of academic interest, as illustrated in Table 7, and t_0 is, therefore, a good approximation of t_n.

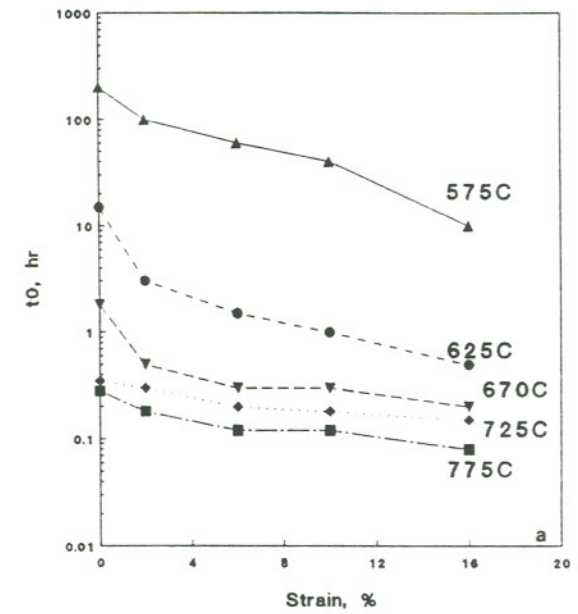

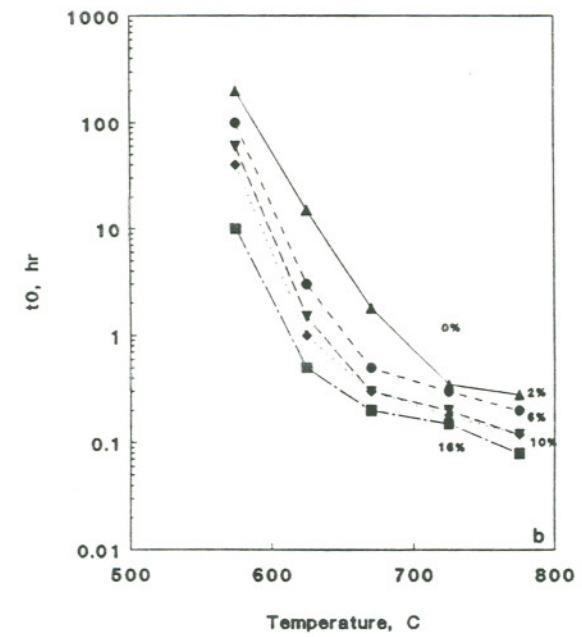

Figure 73. Variation of t_0 versus strain (a) and temperature (b).

Table 7. Conversion of t_0 values to t_n values by subtraction of the effect of t_{depl}.

Temp. C	Strain %	t0 hr	tdepl hr	tn hr
575.0	0.00	200.0000	0.67E+01	193.2820
575.0	2.00	100.0000	0.74E+01	92.6422
575.0	6.00	60.0000	0.31E+01	56.9097
575.0	10.00	40.0000	0.23E+01	37.7277
575.0	16.00	10.0000	0.16E+01	8.4393
625.0	0.00	15.0000	0.61E+00	14.3915
625.0	2.00	3.0000	0.41E+00	2.5893
625.0	6.00	1.5000	0.36E+00	1.1429
625.0	10.00	0.7500	0.17E+00	0.5806
625.0	16.00	0.2500	0.12E+00	0.1327
670.0	0.00	1.8000	0.82E-01	1.7185
670.0	2.00	0.5000	0.69E-01	0.4310
670.0	6.00	0.2000	0.48E-01	0.1515
670.0	10.00	0.2000	0.33E-01	0.1668
670.0	16.00	0.1500	0.25E-01	0.1247
725.0	0.00	0.3500	0.12E-01	0.3382
725.0	2.00	0.3000	0.11E-01	0.2888
725.0	6.00	0.2000	0.15E-01	0.1848
725.0	10.00	0.1500	0.12E-01	0.1382
725.0	16.00	0.1000	0.82E-02	0.0918
775.0	0.00	0.2800	0.25E-02	0.2775
775.0	2.00	0.1800	0.30E-02	0.1770
775.0	6.00	0.1200	0.33E-02	0.1167
775.0	10.00	0.1200	0.29E-02	0.1171
775.0	16.00	0.0800	0.21E-02	0.0779

Computation of the ΔG^* and ΔG_{gb} using matrix Q_a values for each strain level (from Table 6) resulted in numerical values and trends that appeared unlikely (Table 8). The ΔG^* value was computed to be negative for the annealed material at all temperatures. This would imply spontaneous nucleation at every temperature, which does not occur in this system for the temperatures studied. The trends in the negative ΔG^* value also did not increase consistently with increasing temperature, as is expected from classical nucleation theory. No consistent relation between strain and ΔG^* or ΔG_{gb} was also seen and these parameters increased and decreased with strain depending on the specific temperature. These observations indicate that consideration of matrix Q_a results in trends that do not agree with basic nucleation theory, which may imply that this parameter does not have a dominating influence on nucleation phenomena.

Table 8. Thermodynamic barrier to nucleation ΔG^* computed assuming matrix diffusivity of chromium

Temp. °C	Strain %	tn hr	ΔG^* cal/mole	ΔG_{gb} cal/mole
575.0	0.00	193.2820	-7352.2	0.0
575.0	2.00	92.6422	-6599.5	0.0
575.0	6.00	56.9097	1574.1	289.6
575.0	10.00	37.7277	1876.9	284.8
575.0	16.00	8.4393	1337.1	293.8
625.0	0.00	14.3915	-7969.7	0.0
625.0	2.00	2.5893	-9050.3	0.0
625.0	6.00	1.1429	-1519.2	0.0
625.0	10.00	0.5806	-1735.4	0.0
625.0	16.00	0.1327	-2386.9	0.0
670.0	0.00	1.7185	-8568.8	0.0
670.0	2.00	0.4310	-9177.1	0.0
670.0	6.00	0.1515	-2148.6	0.0
670.0	10.00	0.1668	-967.7	0.0
670.0	16.00	0.1247	484.4	319.6
725.0	0.00	0.3382	-7880.5	0.0
725.0	2.00	0.2888	-6195.6	0.0
725.0	6.00	0.1848	1913.5	305.8
725.0	10.00	0.1382	2333.2	301.8
725.0	16.00	0.0918	3517.3	292.4
775.0	0.00	0.2775	-4882.4	0.0
775.0	2.00	0.1770	-3825.3	0.0
775.0	6.00	0.1167	4302.2	297.6
775.0	10.00	0.1171	5310.1	292.4
775.0	16.00	0.0779	6454.1	287.0

The consideration of grain boundary diffusion was carried out by assuming the 16% strain Q_a value to be an approximation of the activation barrier for grain boundary diffusion and resulted in ΔG^* values shown in table 9. A plot of ΔG^* versus temperature shown in Figure 74a indicated that an increase in temperature generally resulted in an increase in ΔG^* between 625°C and 775°C, as would be expected from the classical nucleation theory. Lowering the temperature to 575°C, however, resulted in an increase in ΔG^*, which cannot be explained by nucleation theory, and may indicate a change in mechanism of nucleation at this temperature. Graphing the ΔG^* versus strain illustrated that strain results in a systematic decrease in ΔG^* at all temperatures, as was proposed in the work of Christian[31].

Comparison of strain effects on ΔG_{gb} indicated in Table 9 and Figure 75 shows a clear increase in this parameter with strain at all temperatures. The changes in ΔG_{gb} are, however, more prominent at lower temperatures, and become relatively small, especially at 775°C.

Table 9. Thermodynamic barrier to nucleation predicted from grain boundary diffusion.

Temp °C	Strain %	tn hr	ΔG^* cal/mole	ΔG_{gb} cal/mole
575.0	0.00	193.28	6647.76	231.4
575.0	2.00	92.64	5400.51	243.0
575.0	6.00	56.91	4574.09	251.4
575.0	10.00	37.73	3876.91	258.8
575.0	16.00	8.44	1337.15	293.8
625.0	0.00	14.39	6030.26	250.4
625.0	2.00	2.59	2949.66	279.0
625.0	6.00	1.14	1480.81	297.6
625.0	10.00	0.58	264.61	322.0
625.0	16.00	0.13	-2386.95	0.0
670.0	0.00	1.72	5431.24	266.4
670.0	2.00	0.43	2822.88	288.2
670.0	6.00	0.15	851.35	312.6
670.0	10.00	0.17	1032.26	309.6
670.0	16.00	0.12	484.40	319.6
725.0	0.00	0.34	6119.48	275.8
725.0	2.00	0.29	5804.45	277.6
725.0	6.00	0.18	4913.46	283.0
725.0	10.00	0.14	4333.17	286.6
725.0	16.00	0.09	3517.29	292.4
775.0	0.00	0.28	9117.55	276.0
775.0	2.00	0.18	8174.67	279.6
775.0	6.00	0.12	7302.18	283.2
775.0	10.00	0.12	7310.09	283.2
775.0	16.00	0.08	6454.14	287.0

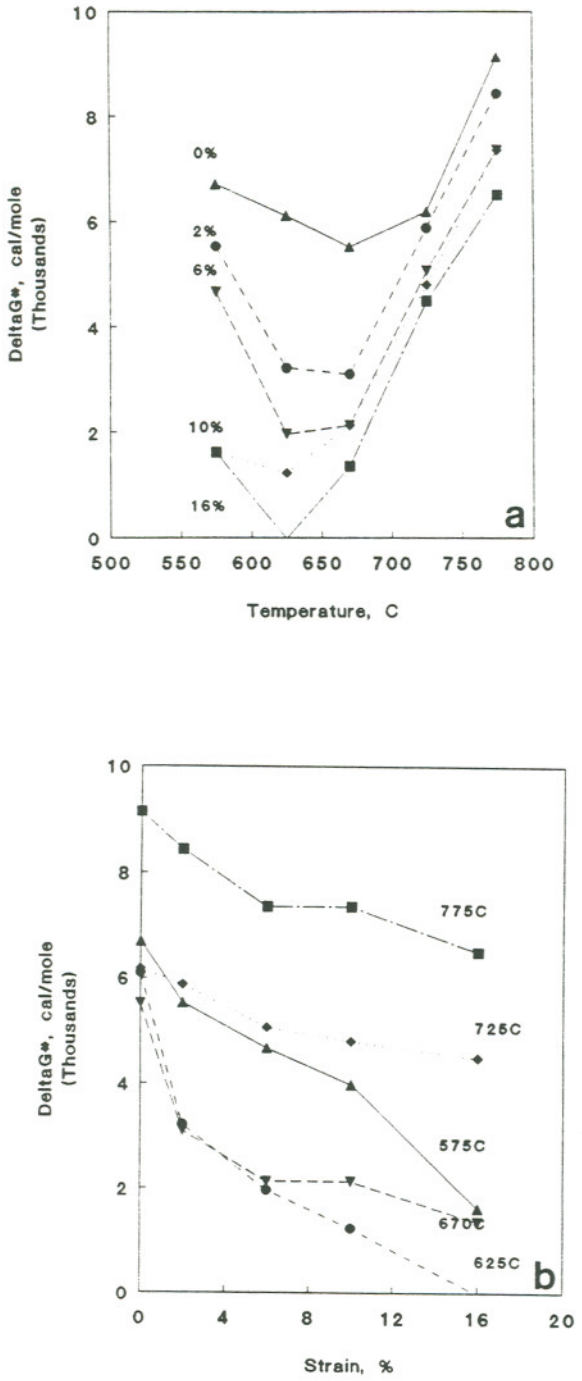

Figure 74. Plot of thermodynamic barrier to nucleation as a function of temperature (a) and strain (b), assuming grain boundary dominated nucleation kinetics.

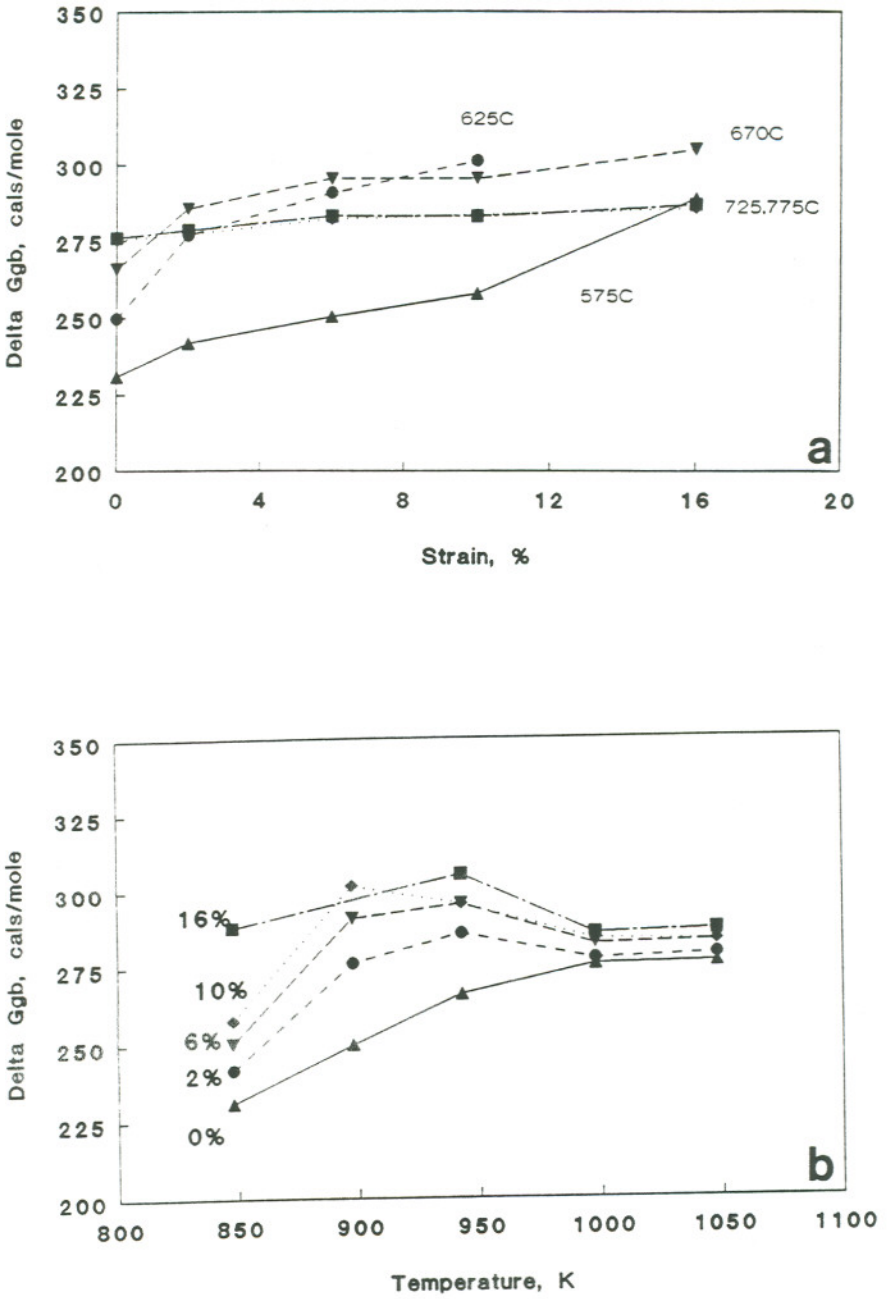

Figure 75. Plot of nucleation related change in grain boundary energy versus strain (a) and temperature (b).

The lowering of ΔG^* computed assuming grain boundary diffusion kinetics agree well with data developed in the EPR test. The acceleration in EPRDOS with strain above 725° could not be explained by kinetic data and appears to be due to a lowering of ΔG^* with strain. At lower temperatures, reductions in ΔG^* and Q_a values both contribute to GBCD development and result in higher levels of acceleration in GBCD, as indicated from the EPRDOS data. The increase in IG attack and twin boundary attack in strained samples also supports the increase in ΔG_{gb} value with strain. These microstructural aspects reflect an increase in nucleation on grain interfaces of strained samples, which result in higher changes in ΔG_{gb}, as noted.

CORRELATION OF THERMODYNAMIC AND KINETIC EFFECTS OF STRAIN WITH AMBIENT DEFORMATION STRUCTURE

Results of microstructural examination in Type 316 SS discussed in Chapter 4 indicated that strain induces

* systematic increases in dislocation density in the matrix and around twin boundaries with increasing strain
* formation of a planar dislocation structure, twin-faulted regions and cell structure at different locations on the materials.

The formation of strain-induced martensite was only noted to be present at isolated locations on strain samples.

The observation of increasing matrix dislocation density with strain agrees well with observations made by Murr et al in Type 304 SS[12,18-20]. The linear relationship developed with strain also shows good agreement with the generic equation

$$d = d_o + A.\ \epsilon$$

for strain effects on dislocation density. Numerical values of dislocation density also match dislocation densities

measured on Type 316 SS after 100 hrs of heat treatment at 625°C[53]. This asserts that no significant change in dislocation density occurs due to recovery processes at 625°C.

The presence of increasing dislocation densities in the vicinity of twin boundaries with strain is an indirect indication that strain-induced structural changes occur on twin (and grain) interfaces. This is because sites for dislocation emission from the interface are usually associated with ledges present on the interface. Although the documentation of increases in ledge densities has not been made in this work, direct observations of changes in this aspect made by Murr et al[13] in Type 304 SS support this result.

The extent of planarity in the dislocation structure development was less apparent in this material as compared to that seen in Type 304 SS. Observation of a dislocation cell structure at certain locations was also noted. These may be due to local changes in stoichiometry of the SS or higher SFE of the Type 316 (70 mJ/m^2 [30,98]) versus Type 304 SS (20 mJ/m^2). The higher SFE reduces the formation of partial dislocations and stacking faults versus tendency of dislocations to cross-slip and reduces the planar deformation pattern of the material.

The absence of martensite noted for Type 316 SS agrees well with observations made by Donadille[30] for Type 316 SS. The possible cause for the absence (versus abundance) of the α'-phase in Type 316 SS versus Type 304 SS may be related to the higher stacking fault energy and stoichiometry, both of which induce changes in the free energy drive for the formation of the phase.

MICROSTRUCTURAL EFFECTS ON GBCD KINETICS

The reduction in the activation barrier to diffusion with strain may be caused by dislocation pipe diffusion, solute segregation to dislocations, sweeping of dislocations to the grain interface and presence of martensite (Chapter 2).

While there is no specific evidence to verify the effect of solute segregation to dislocations on diffusivity, the absence of martensite rules out the effect of this phase on diffusivity. The lowering of strain effects on diffusivity at higher temperatures also does not support the consideration of dislocation sweeping as the key mechanism leading to increased diffusivity. This is because, as temperature increased, the dislocation mobility and extent of dislocation sweeping would be anticipated to increase. This would lead to an increase in the effect of strain at higher temperatures, which is contrary to observations made in this work.

The trends in strain-temperature-diffusion data agree well with trends predicted by dislocation pipe diffusion models

available in the literature. Qualitative predictions of the (simplest) Hart dislocation pipe diffusion equation

$$D_{tot} = D_o \exp(-Q_a/RT) + n A D_{o,p} \exp(-Q_{a,p}/RT)$$

indicate that the total diffusivity (D_{tot}) in (strained) materials increases with increasing dislocation density (n). This yields higher diffusivities in samples strained to higher levels, as observed. The model also indicates that at temperatures typically above half the melting temperature of alloys (about 700°C for Type 316 SS), dislocation density effects on diffusivity are swamped by high lattice diffusivities and/or recovery processes. Lowering of strain effects on diffusivity at temperatures above 700°C have also been observed in diffusion data obtained in this work.

Quantitative comparisons of the chromium diffusivity values with predictions of the Hart model required knowledge of $AD_{o,p}$, $Q_{a,p}$, D_o and Q_a values. Values of D_o and Q_a were calculated to be 50 cm^2/sec and -76000 cals/mole from the diffusion equation for the unstrained material, while $Q_{a,p}$ was assumed to be -62000 cals/mole from the diffusion equation for the 16% strained condition. Determination of the value for the $A D_{o,p}$ term was only possible by dividing the pre-exponent term

(n A $D_{o,p}$ = 0.1 cm^2/sec) from the diffusion equation 16% strain material by its experimentally measured dislocation density (n = 3 x 10^{10} /cm^2). This yielded a value of 3.33 x 10^{-12} cm^4/sec for the term but has the limitation of using experimental data to predict experimental data.

Predictions of Hart model showed excellent match with the experimentally measured diffusivity values for the 2% and 6% strained materials. This is illustrated in a one-to-one comparison of predicted and experimental values (Figure 76). The agreement is present despite the restrictive conditions for the application of the Hart model to low dislocation density materials (Chapter 1).

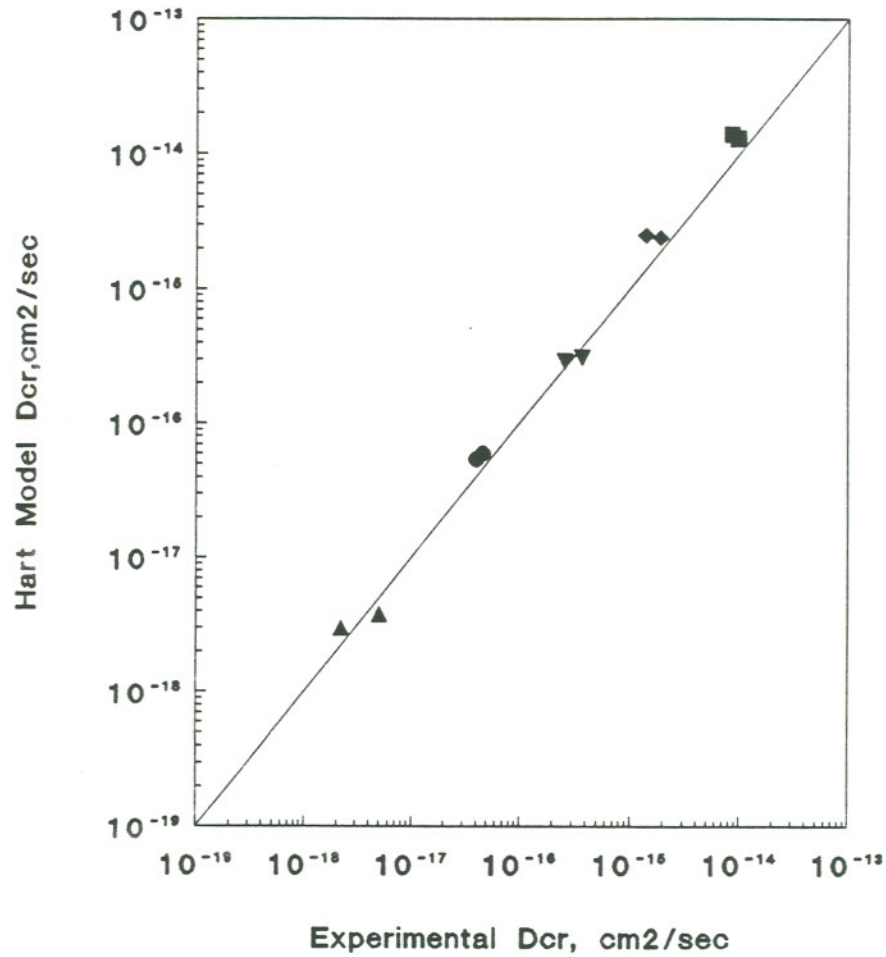

Figure 76. Comparison of chromium diffusivity values predicted by the Hart dislocation pipe diffusion model with experimental diffusivity data obtained in this work.

MICROSTRUCTURAL EFFECTS ON THERMODYNAMICS OF IG CARBIDE PRECIPITATION

Deformation effects on lowering the free energy barrier for nucleation and increasing the free energy change during carbide nucleation at grain boundaries appears to be due to alterations in the grain boundary structure during the straining process. More specifically, strain results in an increase in grain boundary ledge densities, as noted in the work of Murr et al[13]. Since ledges are high energy sites which favor carbide precipitation on grain boundaries, an increase in the ledge density with strain causes an increase in the number of favored nucleation sites on the interface. This results in an increase in ΔG_{gb} (and thereby lower ΔG^*) as has been observed. The lowering of strain effects on ΔG_{gb} and ΔG^* calculated at higher temperatures may, in addition, be due to a decrease in the effectiveness of ledge sites for precipitation. This has been observed by Varin et al[99] during carbide precipitation in a Type 316 SS.

The effect of strain on ledge densities and IG precipitation can also be considered by examining strain effects on specific grain boundary energies, as shown conceptually in Figure 77a,b. A statistical distribution of grain boundary energies

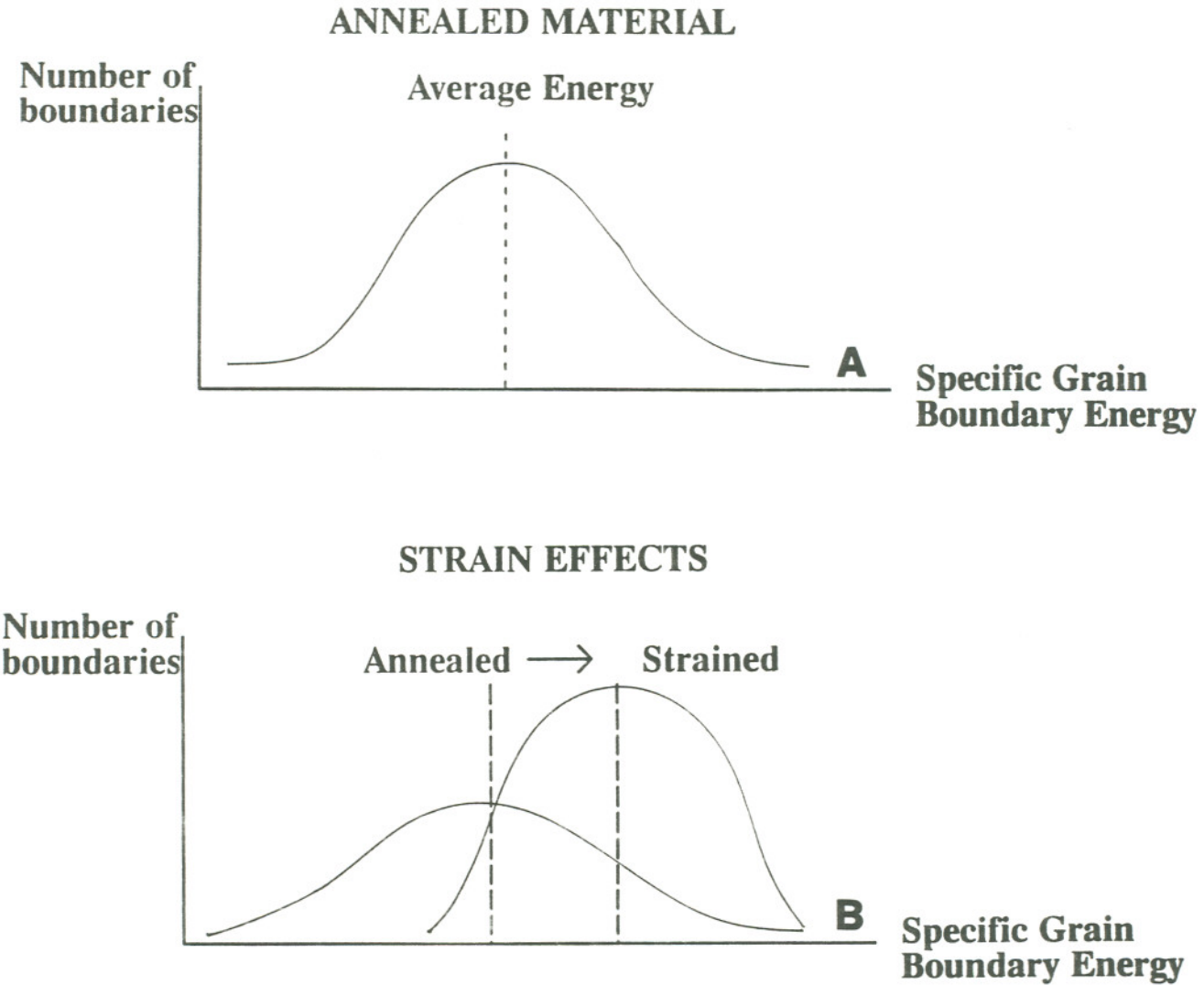

Figure 77. Conceptual view of grain boundary energy distribution in annealed materials (a) and strain effects on grain boundary energy and intergranular carbide precipitation (b).

which spread around the "average" value is typically present on annealed materials (Figure 77a). This distribution of energies results in variations in IG carbide precipitation and GBCD development from boundary to boundary in annealed materials. High energy boundaries contain a larger number of structural defects, i.e. ledges, and develop more rapid precipitation-depletion than low energy boundaries.

Straining of the annealed material causes an increase in the ledge defect structures in all boundaries. This is expected to cause the average energy of the distribution to move to the right, as shown in Figure 77b, due to presence of a larger number of high energy sites on grain boundaries. Another alteration that may be produced by strain is a narrowing of the distribution of energies, with more boundaries being spread close to the average energy. This is expected because strain is more likely to produce dramatic changes in low energy versus high energy boundaries (which already contain a large number of ledges). Evidence for this was also seen when (low energy) annealing twin boundaries were attacked at times comparable to high energy boundaries in strained samples, while the phenomena was not apparent in annealed samples.

MICROSTRUCTURAL EFFECTS ON INTRA-GRAIN CARBIDE PRECIPITATION AND TG EPR TEST ATTACK

Transgranular attack was observed to occur on EPR etched samples strained to levels greater than 16-20%. The attack was identified to be due to precipitation of carbides on regions of high dislocation density and intersections of twin-faulted regions, which agrees well with similar observations made by other researchers in strained Type 316 SS[94]. The absence of bulk martensite, however, rules out the effect of this phase on TG attack as reportedly seen in Type 304 SS[45-48].

Transgranular attack was also noted to be a function of temperature and strain level. Increasing the temperature of heat treatment resulted in the occurrence of TG attack at shorter times, while increasing time and strain level caused increased levels of TG etching. This occurs because deformation sites that are formed within the grain are high energy sites which compete with the grain interface for precipitation. Activation of sites is, therefore, dependent on the specific energetics of the site, as is similar to that on grain boundaries.

The effect of strain on intra-grain carbide precipitation and TG attack can be understood through the concepts developed in Figure 78. The figure illustrates that in annealed materials, the number of favored sites for intra-grain precipitation are low, and the energy of these sites is also significantly lower than that of grain boundaries. This causes precipitation in annealed materials to occur on grain boundaries. Increasing the strain causes an increase in the number and energy of intra-grain precipitation sites and the distribution of energy moves closer to the average grain boundary energy (which is also increasing but a slower rate than that of intra-grain sites). The strain level (in this case 16-20%) at which an overlap of energy distributions for grain boundary and intra-grain sites occurs, will cause formation of intragranular carbide precipitates and TG attack to occur simultaneous with IG precipitation and attack. The presence of a distribution of energies will also cause a time and temperature effect on the phenomena (as was observed).

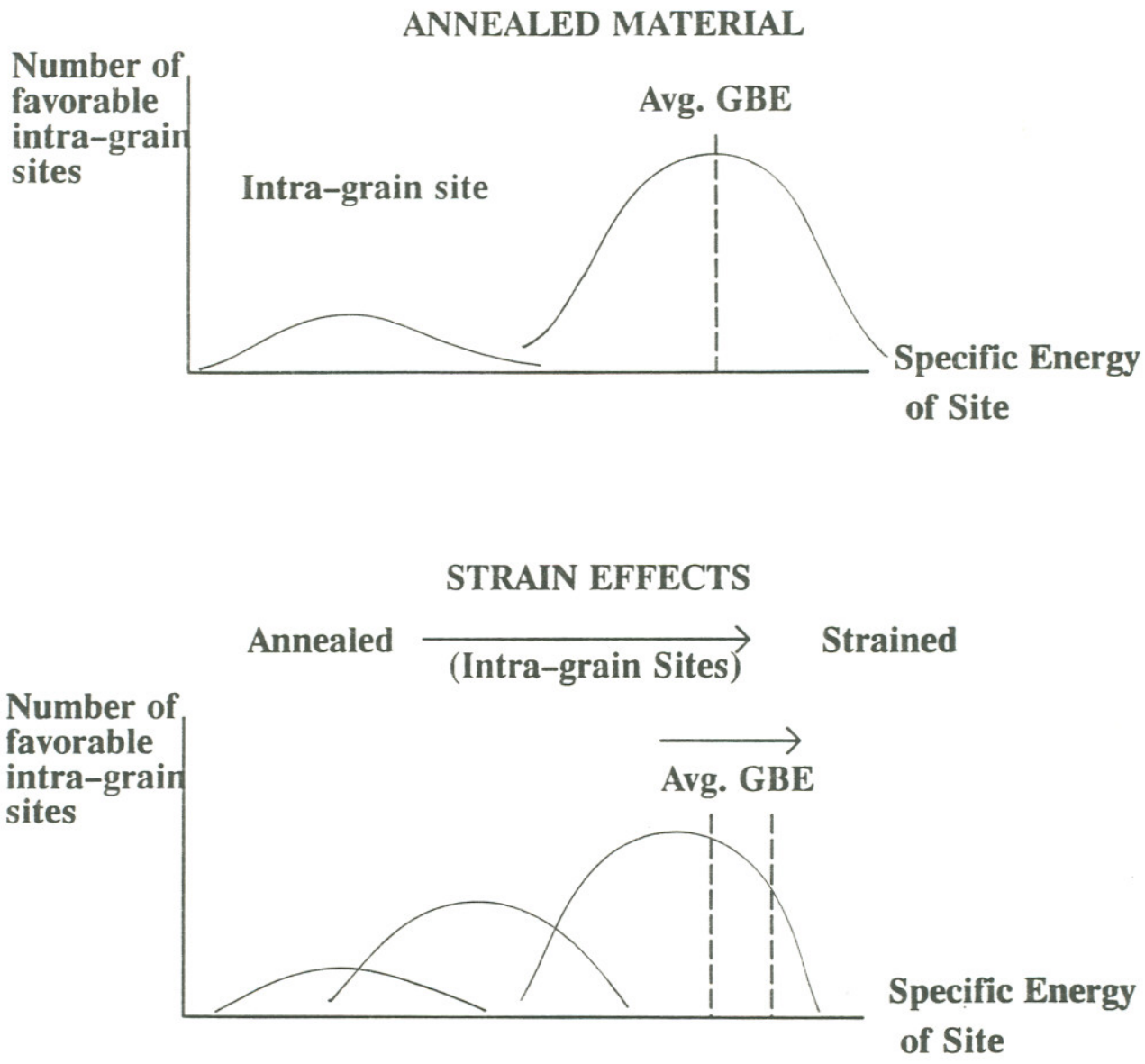

Figure 78. Conceptual view of strain effects on intra-grain versus inter-grain carbide precipitation and GBCD development.

MODELING DEFORMATION EFFECTS ON GRAIN BOUNDARY CHROMIUM DEPLETION

Detailed modeling of deformation effects on GBCD requires consideration of the microstructural changes induced by deformation and their effects on the thermodynamics and kinetics of the process (Figure 79). These models are, however, difficult to evaluate and require numerical methods for their solution. Limited thermodynamic and kinetic data available on the GBCD phenomena also further complicates their development.

The only model that has been developed to evaluate deformation effects on Cr_{min}, W_{cr} and VP of GBCD and EPRDOS was developed by Bruemmer[56]. This model (called SSDOS) empirically modifies diffusivity values as a function of strain using the equation

$$D_{cr} = D_{cr} \ (1 + 0.4 \ \text{Strain\%})$$

to fit a database developed for deformation effects on sensitization. Thermodynamic effects of strain are not accounted for by the SSDOS model.

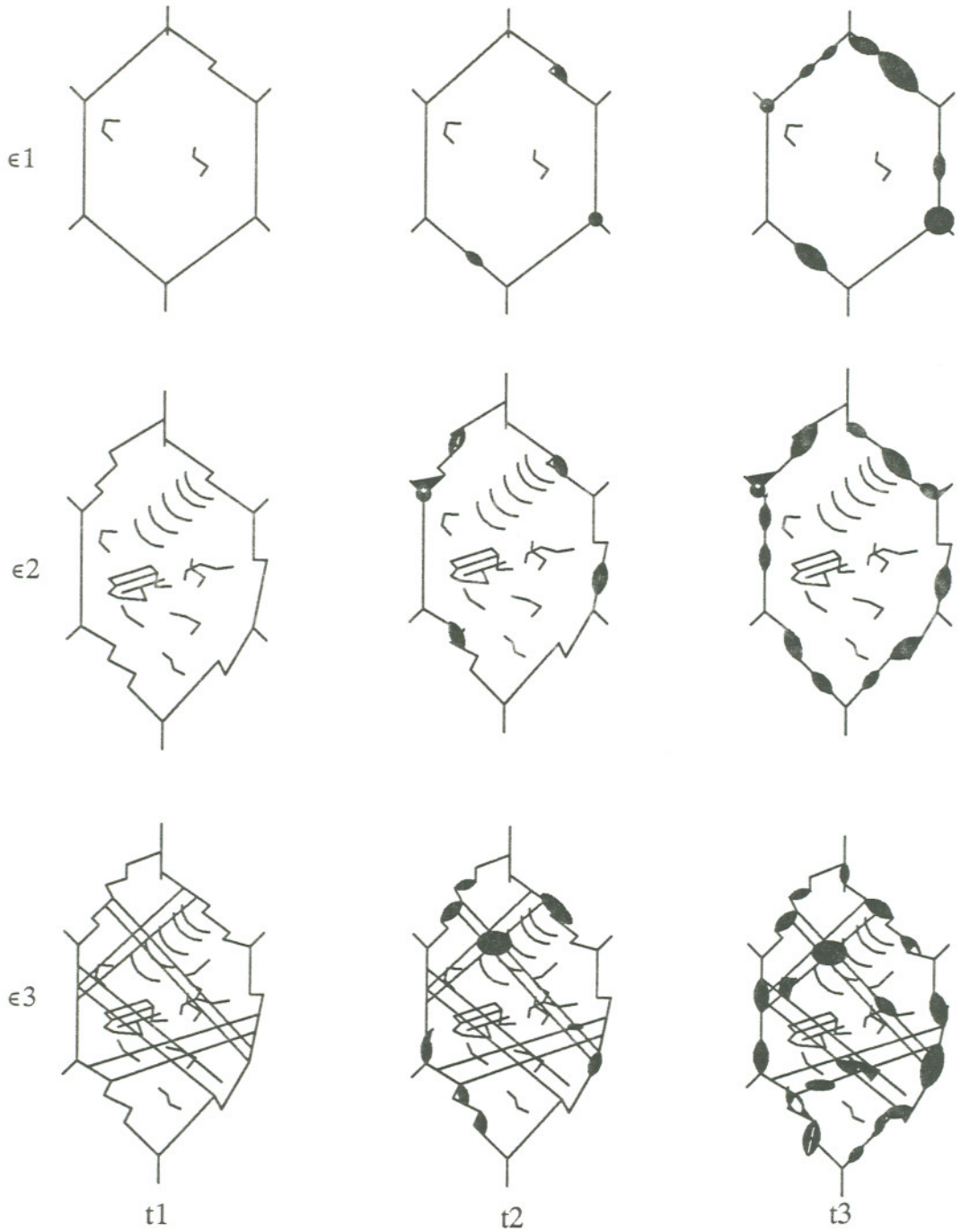

Figure 79. Phenomenological model for deformation effects on grain boundary chromium depletion illustrating effects of increasing strain and heat treatment on microstructural development in the material.

A comparison of the D_{cr} and t_n data predicted by the SSDOS model with experimental data obtained in this work indicates that the model overpredicts D_{cr} and underpredicts t_n for all temperatures and strains examined (Figure 80a,b). Both aspects cause the prediction of higher EPRDOS values than have been measured in the data developed in this research (Figures 81-83).

To improve the modeling capability and theoretical basis of SSDOS, the thermodynamic and kinetic data developed in this work were input as subroutines into the model. The kinetic data was input as diffusion equations for the 0%, 2%, 6%, 10% and 16% strained materials. This allowed prediction of diffusivity data on these strained materials as a function of temperature, which was then linearly interpolated for any strain level between 0 and 16%. No prediction capability was developed for data above 16% strain due to the presence of TG attack. The thermodynamic ΔG_{gb} data was input using two-degree equations used to curve fit the data as a function of temperature for 0, 2, 6, 10 and 16% strained materials. The ΔG_{gb} was then linearly interpolated with strain and used to

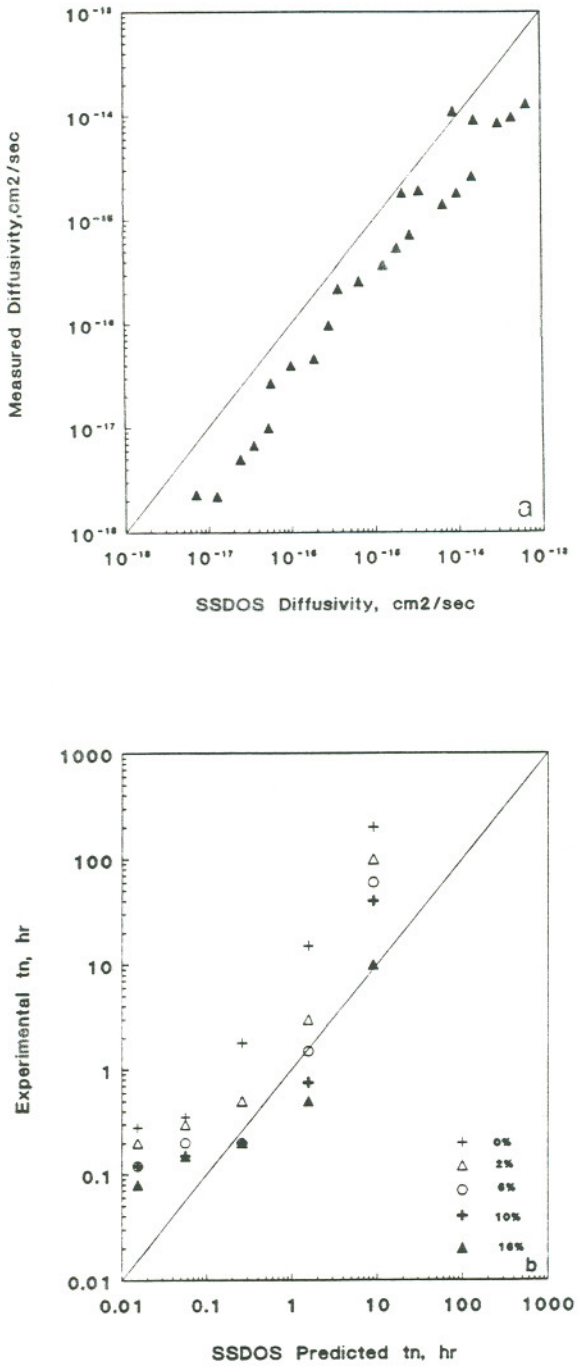

Figure 80. Comparison of SSDOS predicted versus experimental diffusivities (a) and nucleation times (b) for strained austenitic SS.

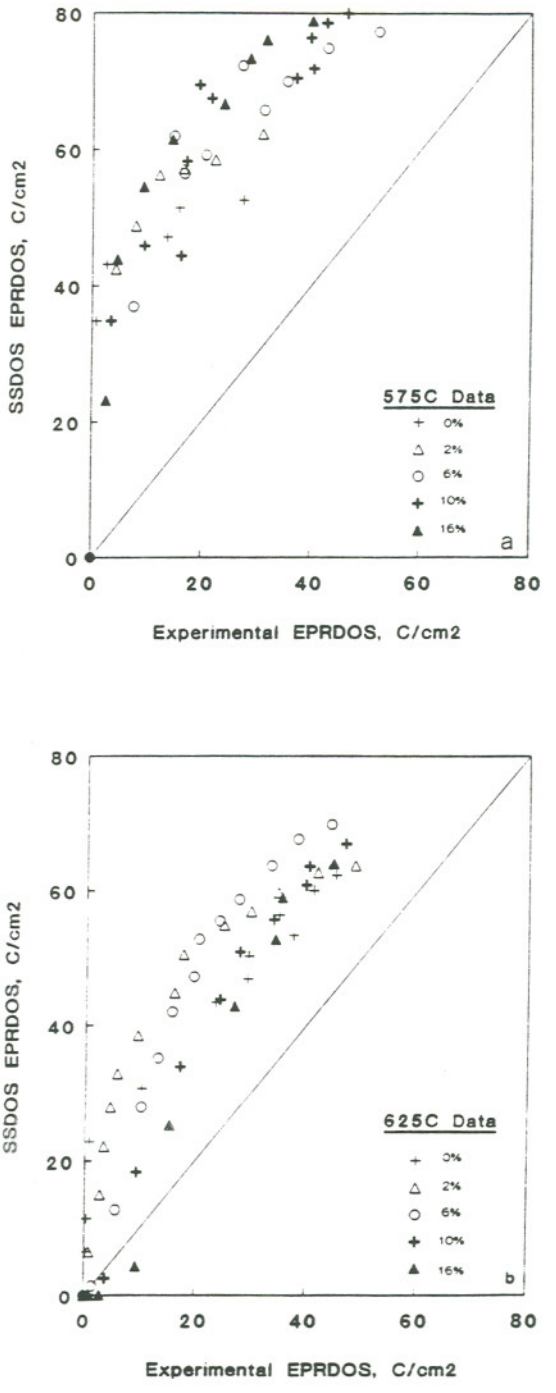

Figure 81. Comparison of SSDOS predicted versus experimental EPRDOS for Type 316 SS at 575°C (a) and 625°C (b).

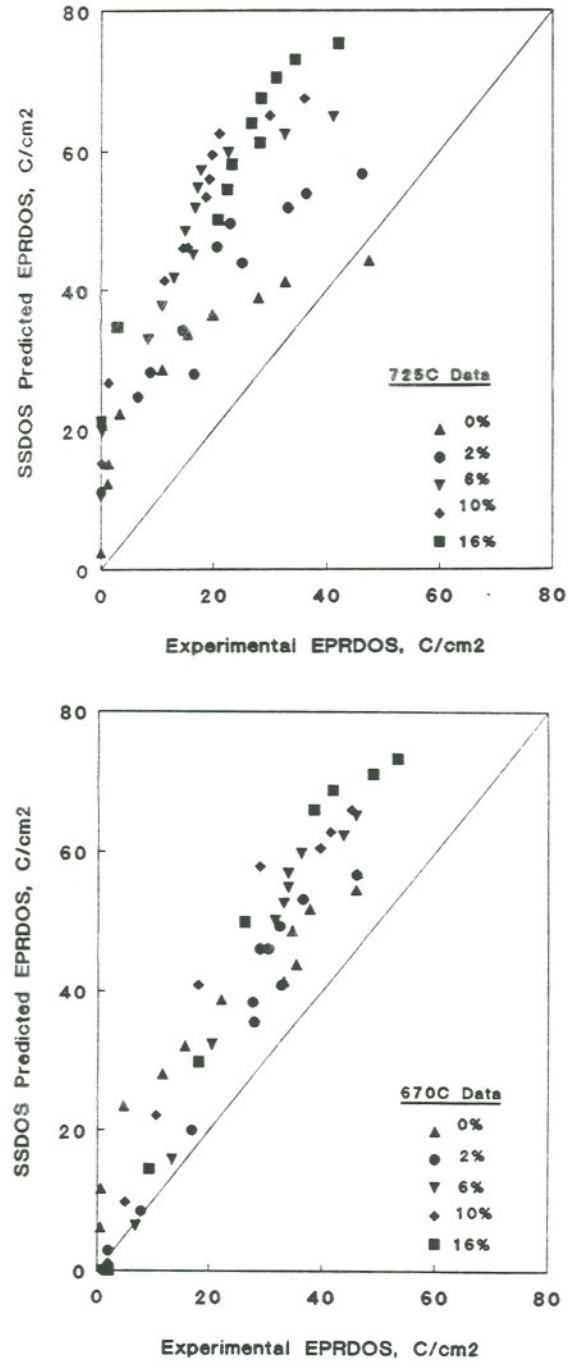

Figure 82. Comparison of SSDOS predicted versus experimental EPRDOS values for strain effects on sensitization at 670°C (a) and 725°C (b).

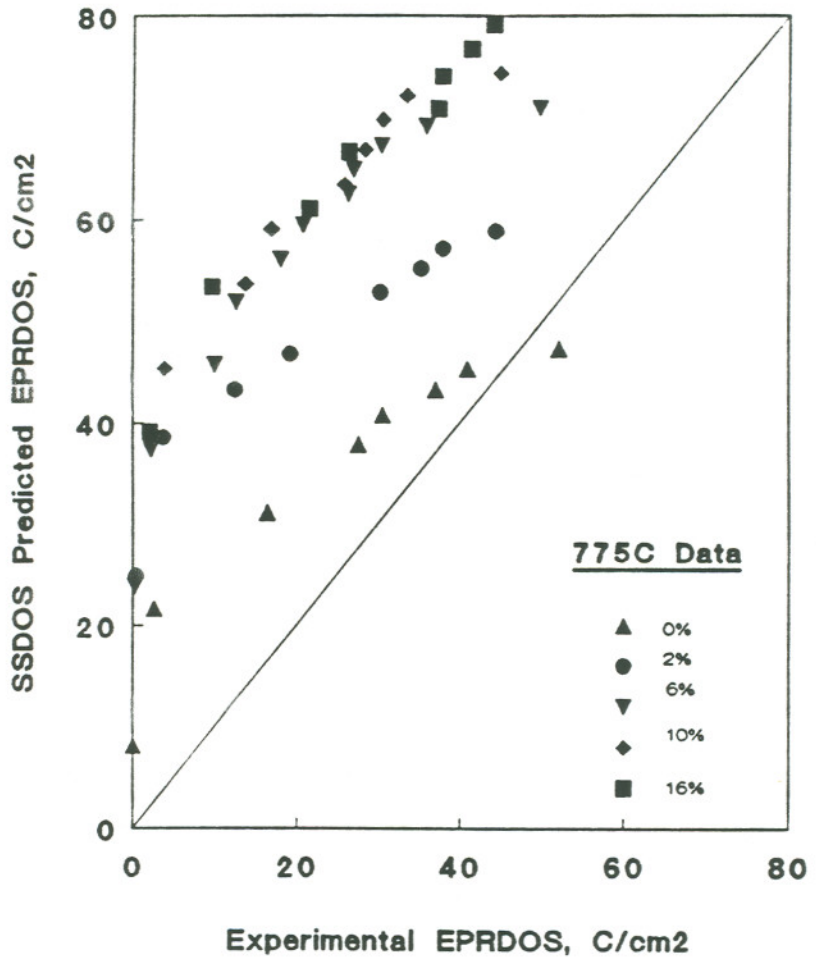

Figure 83. Comparison of SSDOS predicted and experimental EPRDOS values at 775°C.

calculate ΔG^* and t_n using equations discussed above (see Appendix 1C).

A significant improvement in the predictive capability of the EPRDOS data was obtained using the thermodynamic and kinetic data developed in this work. The data points in general, tended to scatter around the one-to-one correspondence line between EPRDOS values predicted by the modified SSDOS software and experimental values measured in this work (Figure 84). The lack of experimental deformation-diffusion data developed by other researchers for comparison with the modified SSDOS program is a limitation of the present model.

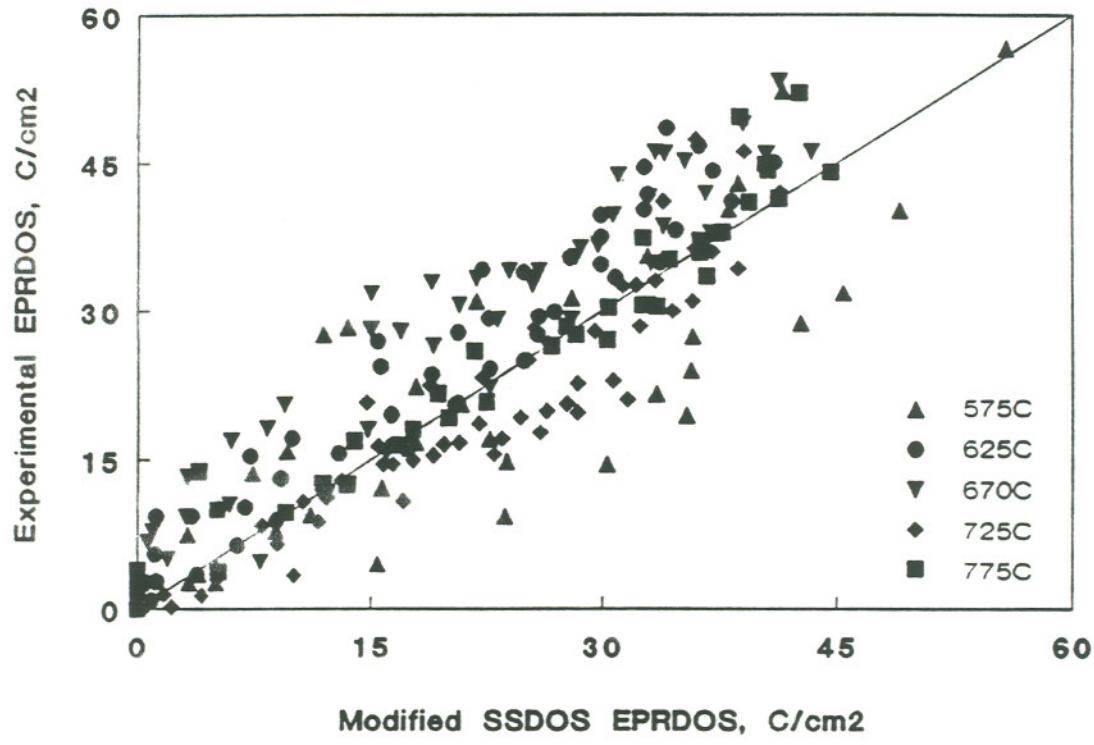

Figure 84. Comparison of (modified) SSDOS predictions versus experimental EPRDOS values in the range of 575°C to 775°C.

CHAPTER 6

SUMMARY AND CONCLUSIONS

QUANTITATIVE ASSESSMENT OF STRAIN EFFECTS ON GBCD

* A database that investigated the effects of strain magnitude (0-40%) and heat treatment (575°C - 775°C, 0.1 - 500 hrs) on grain boundary chromium depletion development was developed using the EPR test and TEM.
* Deformation was observed to be a key variable inducing accelerated sensitization development at 625°C. The increase in DOS was observed to be a systematic function of strain and corroborated by optical and TEM observations of increased carbide precipitation, IG attack and twin boundary attack with increasing strain.
* Temperature was also found to be a critical factor in deformation induced sensitization development. Decreasing the temperature from 625°C to 575°C showed similar levels of acceleration in DOS. Increasing the temperature through 670°C to 775°C was found to systematically decrease the effects of strain on GBCD seen at 625°C.
* Deformation above 16-20% was noted to produce a time-temperature-strain dependent TG attack during EPR testing. This attack was induced by precipitation of carbides in regions of high dislocation density and intersections of twin-faults produced by the straining process.

DEFORMATION EFFECTS ON THERMODYNAMICS AND KINETICS OF GBCD

* An analytical method was developed to evaluate chromium diffusivity (D_{cr}), thermodynamic barrier for nucleation (ΔG^*) and free energy change due to grain boundary nucleation (G_{gb}) from the EPR test data.
* Deformation produced increased chromium diffusivity and, thereby, accelerated the kinetics of sensitization development in the SS. The increase in diffusivity was typically an order of magnitude at 575°C and 625°C, and decreased with increasing temperature until no acceleration in diffusivity was observed at the highest temperatures of 725 and 775°C.
* Slopes of log diffusivity versus inverse temperature Arrhenius plots were used to determine the activation barrier to diffusion Q_a on strained and unstrained materials. The calculated Q_a value decreased with increasing strain.
* A reduction in ΔG^* value occurred with increasing strain. This was related to an increase in the free energy change at grain boundaries ΔG_{gb} value during strain induced nucleation. The effect of strain on lowering ΔG^* and increasing ΔG_{gb} was, however, seen to decrease as the temperature was raised from 575°C to 775°C.

CORRELATION OF AMBIENT TEMPERATURE DEFORMATION MICROSTRUCTURE WITH THERMODYNAMIC AND KINETIC EFFECTS OF STRAIN ON GBCD

* An increase in dislocation density and twin-fault density with strain, presence of dislocation cellular regions and absence of strain-induced martensite were noted in the matrix regions examined using TEM. Increases in dislocation density around twin boundary regions with strain also indicated possible changes in structures of grain boundaries caused by strain.
* The increase in kinetics of GBCD development appears to be due to increased dislocation density and dislocation pipe diffusion of chromium induced by the straining process.
* Alterations in grain boundary ledge densities with strain were considered to be the cause for deformation effects on increasing the free energy change during precipitation on grain boundaries and lowering of the thermodynamic barrier to nucleation.
* Formation of carbides on high energy sites in the deformation structure was attributed to be the cause for intragranular precipitation and TG attack during EPR testing. Activation of these sites for precipitation and development of TG attack was dependent on time, temperature and strain level.

GRAIN BOUNDARY CHROMIUM DEPLETION MODELING

* The difficulty in detailed microstructural modeling of deformation effects on GBCD led to the use of a theoretically based empirically modified (SSDOS) model for comparison with the data developed in this work.
* The SSDOS model used higher diffusivity correlations and underpredicted the time to nucleate carbides on grain interfaces. This yielded higher predictions of EPRDOS than experimentally determined values for all temperatures and strain conditions.
* Modification of the model using D_{cr} and ΔG_{gb} values determined in this work yielded a significant improvement in the capability of the model to predict the current database.

MATERIAL ANNEAL CONDITION EFFECTS ON GRAIN BOUNDARY CHROMIUM DEPLETION

* Annealing treatments used for heat treating SS were found to have a significant effect on the GBCD development of the SS. Mill annealing at 1100°C for 5min and solution annealing (SA) at 1100°C for 1hr resulted in low levels of sensitization in comparison with materials annealed at 1000°C and 1050°C for 0.5 - 1 hr.
* Observations of low levels of deformation and absence of carbide precipitation in the mill processed (MP) and SA1100-1hr materials were attributed to be the cause for the low sensitization response of these conditions.
* Presence of carbide precipitation noted in the TEM microstructures of as-quenched SA1000 and SA1050 materials provided favored sites for development of accelerated sensitization in these conditions.

REFERENCES

1. E.C. Bain, R.H. Aborn and J.J.B. Rutherford, Trans. Amer. Soc. Steel Treating, **21**, 481 (1933).

2. American Society for Metals Handbook, Vol. 2,

3. P. Polukhin, S. Gorelik and V. Vorontsov, "Physical Principles of Plastic Deformation," Mir Publishers (1983).

4. G.E. Dieter, "Mechanical Metallurgy," McGraw Hill Internat. Book Co. (1982).

5. H.O. Martikainen and V.K. Lindroos, Acta Metall., **33**, 1223 (1985).

6. J.C.M. Li, J. Appl. Phys., **32**, 525 (1961).

7. M.F. Ashby, Phil. Mag., **21**, 399 (1970).

8. A.W. Thompson, M.E. Baskes and W.F. Flanagan, Acta Metall., **21**, 1017 (1973).

9. J.P. Hirth, Metall. Trans., **3**, 3047 (1972).

10. S.V. Tsivinskii, Phys. Stat. Sol. (a), **36**, 11 (1976).

11. H. Gleiter, in Chalmers Anniversary Volume - Progress in Materials Science, ed. J. W. Christian, et. al., Pergamon Press, 1981.

12. L.E. Murr and S.H. Wang, Res. Mechanica **4**, 237 (1982).

13. L.E. Murr and S.H. Wang, Res. Mechanica Letters, **1**, 85, (1981).

14. L.E. Murr and S.H. Wang, 38th Ann. Proc. Electron Microscopy Soc. Amer., ed. G. W. Bailey (1980).

15. L.E. Murr and S.S. Hecker, Scripta Metall., **13**, 167 (1981).

16. L.E. Murr, Mat. Sci. and Eng., **51**, 71 (1981).

17. L.E. Murr, Res. Mechanica, **9**, 159 (1983).

18. L.E. Murr, "Materials at High Strain Rates," ed. T. Z. Blazynski, Elsevier Applied Science Publishers (1987).

19. L.E. Murr and K.P. Staudhammer, "Shock Waves for Industrial Applications," ed. L. E. Murr, Noyes Publications, p.1 (1988).

20. L.E. Murr and F.I. Grace, Trans. AIME, **245**, 2225 (1969).

21. G.B. Olson and M. Cohen, J. Less Common Metals, **28**, 107 (1972).

22. G.B. Olson and M. Cohen, Metall. Trans. A, **6A**, 791 (1975).

23. S.S. Hecker, M.G. Stout, K.P. Staudhammer, and J. L. Smith, Metall. Trans. A, **13A**, 619 (1982).

24. L.E. Murr, K.P. Staudhammer and S.S. Hecker, Metall. Trans. A, **13A**, 627 (1982).

25. K.P. Staudhammer, L.E. Murr and S.S. Hecker, Acta Metall., **31**, 267 (1983).

26. L.E. Murr and K.P. Staudhammer, Mat. Sci. and Eng., **20**, 35 (1975).

27. T. Suzuki, H. Kojima, K. Suzuki, T. Hashimoto and M. Ichihara, Acta Metall., **25**, 1151 (1977).

28. J.W. Brooks, M.H. Loretto and R.E. Smallman, Acta Metall., **27**, 1829 (1979).

29. J.W. Brooks, M.H. Loretto and R.E. Smallman, Acta Metall., **27**, 1839 (1979).

30. C. Donadille, R. Valle, P. Dervin and R. Penelle, Acta Metall., **37**, 1547 (1989).

31. J.W. Christian, "The Theory of Transformation Kinetics in Metals and Alloys Part I- Equilibrium and General Kinetic Theory," Pergamon Press Limited., 2nd ed. (1975).

32. R. Barbosa and D.B. Santos, Proc. Conf. on Precipitation Phenomena - Deformation and Aging Symposium, World Materials Congress of Amer. Soc. Metals, 19 (1988).

33. P.G. Shewmon, "Diffusion in Solids," McGraw Hill, 1963.

34. R.E. Reed-Hill, "Physical Metallurgy Principles," Litton Educational Publishing Inc., 388 (1973).

35. A. Seeger, D. Schumacher, W.S. Schilling and J. Diehl, editors Proc. Internat. Conf. on "Vacancies and Interstitials in Metals," Wiley Interscience, John Wiley and Sons, New York (1968).

36. N.A. Gjostein, "Diffusion," Amer. Soc. Metals Seminar, ed. H. I. Aaranson, 241 (1973).

37. R.W. Baluffi, Phys. Stat. Solidi, **42**, 11 (1970).

38. J. Burke, "The Kinetics of Phase Transformations in Metals", Pergamon Press, Oxford (1985).

39. L.E. Murr, A.H. Advani, D.G. Atteridge and S. Shankar, Metallography, in press.

40. E.P. Butler and P.R. Swann, Acta Metall., **24**, 343 (1976).

41. S. Lartigue and L. Priester, Acta Metall., **31**, 1809 (1983).

42. R. Gronsky and P. Furrer, Metall. Trans. A., **12A**, 121 (1981).

43. A.R. Jones, P.R. Howell and B. Ralph, J. Mater. Sci., **11**, 1593 (1976).

44. C.S. Tedmon, D.A. Vermilyea and D.E. Bruecker, Corrosion, **27**, 104 (1971).

45. C.L. Briant and A.M. Ritter, Scripta Metallurgica, **13**, 177 (1979).

46. C.L. Briant and A.M. Ritter, Metall. Trans. A, **11A**, 2009 (1980).

47. C.L. Briant and A.M. Ritter, Metall. Trans. A, **11A**, 910 (1981).

48. C.L. Briant, Corrosion, **38**, 596 (1982).

49. E.P. Butler and M.G. Burke, Acta Metall., **34**, 557 (1986).

50. S. Pednekar and S. Smialowska, Corrosion, **36**, 565 (1980).

51. A. Bose and P.K. De, Corrosion, **43**, 624 (1987).

52. G. Rondelli, B. Mazza, T. Pastore and B. Vicentini, "Electrochemical Methods in Corrosion Research," ed. M. Dupont, Mat. Sci. Forum, **8**, 593 (1986).

53. A.H. Advani, D.G. Atteridge and S.M. Bruemmer, Proc. Conf. on Precipitation Phenomena - Deformation and Aging Symposium, World Materials Congress of Amer. Soc. Metals, 1 (1988).

54. V. Cihal, Corrosion Science, **20**, 737 (1980).

55. V. Cihal, "Intergranular Corrosion of Steels and Alloys," Elsevier Science Publishers B. V., 146 (1984).

56. S.M. Bruemmer, "Quantitative Measurement and Modeling of Sensitization Development in Stainless Steels," PhD. thesis, Oregon Graduate Center, Beaverton, OR 97006, 1988.

57. C.S. Tedmon Jr., D. A. Vermilyea and J. H. Rosolowski, J. Electrochem. Soc., **118**, 192 (1971).

58. R.L. Fullman, Acta Metall., **30**, 1407 (1982).

59. G.S. Was and R. M. Kruger, Acta Metall., **33**, 841 (1985).

60. C. Wagner, "Thermodynamics of Solids," Addison Wesley, Reading, Massachussets, 51 (1952).

61. F. Kohler, Monatsh. Chem., **91**, 738 (1960).

62. R. Becker, Ann. Phys., **32**, 128 (1938).

63. R.W. Logan, "Computer Simulation of Sensitization in Stainless Steels," UCID - 20000, Lawrence Livermore National Laboratory, 1983.

64. P.J. Grobner, Metall. Trans. A, **4A**, 251 (1973).

65. C. Stawstrom and M. Hillert, J. Iron Steel Inst., 77 (1969).

66. T. Thorvaldasson and A. Salwen, Scripta Metall., **18**, 739 (1984).

67. E.W. Hart, Acta Metall., **5**, 597 (1957).

68. G.R. Love, Acta Metall., **12**, 731 (1964).

69. A.L. Ruoff and R.W. Baluffi, J. Appl. Phys., **34**, 1348 (1963).

70. H.M. Morrison, Phil. Mag., **12**, 985 (1965).

71. D. Gupta and K.W. Asai, Phys. Rev. B, **7**, 586 (1973).

72. A.D. Le Claire, "Diffusion in Dilute Substitutional Alloys", paper presented at a seminar of the American Society for Metals, Oct14/15 (1972).

73. D. Turnbull and R.E. Hoffman, Acta Metall., **2**, 419 (1954).

74. A.D. Le Claire and A. Rabinovitch, J. Phys. C: Sol. State Phys., **14**, 3863 (1981).

75. A.D. Le Claire and A. Rabinovitch, J. Phys. C: Sol. State Phys., **15**, 3455 (1982).

76. J. Mimkes and M. Wuttig, Phys. Rev. B, **2**, 1619 (1970).

77. W. C. Johnson, C. L. White, P. E. Marth, P. K. Ruf, S. M. Tuominen, K. D. Wade, K. C. Russell and H. I. Aaronson, Metall. Trans. A, **6A**, 911 (1975).

78. T.A. Mozhi, H.S. Betrabret, V. Jagannathan, B.E. Wilde and W. A. T. Clark, Scripta Metall., **20**, 723 (1986).

79. T.A. Mozhi, M.C. Juhas and B.E. Wilde, Scripta Metall., **21**, 1547 (1987).

80. E.L. Hall and C.L. Briant, Metall. Trans. A, **15A**, 793 (1984).

82. S.M. Bruemmer, L.A. Charlot and D.G. Atteridge, Corrosion, **44**, 427 (1988).

83. H.W. Pickering and R.N. Iyer, Third International Conf. Environmental Degradation of Engg. Mat., Pennsylvania (1987).

84. B.W. Bennett and H.W. Pickering, Acta Metall., **36**, 539 (1988).

85. S.M. Bruemmer, L.A. Charlot, B.W. Arey, Corrosion, **44**, 328 (1988).

86. W.L. Clarke, R.L. Cowan and W.L. Walker, in ASTM STP 656, 99 (1978).

87. W.L. Clarke, General Electric Report GEAP-21382, U. S Nuclear Regulatory Commission NUREG-0251-1 (1976).

88. P.B. Hirsch, A.W. Howie, R.B. Nicholson, D.W. Pashley and M.J. Whelan,"Electron Microscopy of Thin Crystals",

Robert E. Krieger Publishing Co., Huntington, New York, p. 422.

89. L.E. Murr, "Electron and Ion Microscopy and Microanalysis: Principles and Applications", Marcel Dekker, New York, 1982.

90. Standard Test Method for Determining Average Grain Size, Annual Book of Stds., **3**.01 (E112-88), American Soc. for Testing of Metals (1988).

91. American Society for Metals Handbook, 9th ed., **9**, 307 (1985).

82. J.W. Simmons, "Prior Deformation Effects on Continuous Cooling Sensitization of Type 316 Austenitic Stainless Steels", M. S. Thesis, Oregon Graduate Center, Beaverton, Oregon 97006 (1989).

93. M. Deighton, J. Iron and Steel Inst., 1012 (1970).

94. B. Weiss and R. Stickler, Metall. Trans. A, **3A**, 851 (1972).

95. J.K. Lai, Mat. Sci. and Engg., **58**, 195 (1983).

96. E.L. Hall and C. L. Briant, Metall. Trans. A, **16A**, 1225 (1985).

97. K. Arioka, M. Hourai, S. Nocuchi and K. Onimura, Corrosion,/83, Paper No. 134, National Association of Corrosion Engineers, 1983.

98. R.E. Schramm and R.P. Reed, Metall. Trans. A, **6A**, 1345 (1975).

99. R.A. Varin and E. Romanowska-Haftek, Metall. Trans. A, **17A**, 1967 (1986).

APPENDIX 1A

SOFTWARE FOR DETERMINING CHROMIUM DIFFUSIVITY

```
c     ------------------------------------------------------------
c
c       Algorithm diffcalc
c
c
        program diffcalc
c
c       ------------------------------------------------------
c
c
c       definition of terms used in program
c
c
        real annlt,annltm,c,crbulk,ni,mo
        real strain,t,time0
        real check,cratk,crmin,ddiff,diff,erfinv,error,
     2  eslope, pslope,ratio,strain,diff, crdiff
        integer i,n,l,k,nsmple, id
        real exepr(50),extime(50),vp(50),wid(50),prootm(50),prepr(50),
     2  erootm(50),mtime(50)
c
c
c       ------------------------------------------------------------------
c
c
c       initialization of minimum chromium level for epr test attack
c       and gas constant
c
c
        cratk = 13.5
        r = 2.0
c
c
c       ----------------------------------------------------------
c
c
c       inputing solution anneal conditions and bulk composition of
c       sample
c
        open(5,file ='diff.dat',status='old')
        read(5,*) annlt,annltm
        read(5,*) c,crbulk,ni,mo
c
c
c       ----------------------------------------------------------
c
c
c       setting up of output files
c
c
        open(10, file = 'diff.op1')
        write(10,2000)
        open(15, file = 'diff.op2')
c
c
c       ----------------------------------------------------------
c
c
c       setting up the loop to perform the diffusivity calculations
c       for the n samples, one at a time
```

```
c
c
      read(5,*) nsmple
      do 500 k = 1,nsmple,1
c
c
      write(*,*) '-------------------------------------------'
      write(*,*)
      write(*,*) '      calculations for material ',k
      write(*,*)
      write(*,*) '-------------------------------------------'
c
c
c     ------------------------------------------------------------
c
c
c     inuputing the experimental temperature and strain level
c     for sample identity id.
c
c
       read(5,*) id,t,strain
c
c
c     ------------------------------------------------------------
c
c           experimental calculation of epr-root time slope
c
c     ------------------------------------------------------------
c
c
      write(*,*)
      write(*,*)
      write(*,*) 'experimental slope calculations in progress'
      write(*,*)
c
c
c     ------------------------------------------------------------
c
c
      write(*,*)
      write(*,*) '     experimental data reading'
      write(*,*)
c
c
c     ------------------------------------------------------------
c
c
c     reading experimental time and experimental epr values for
c     sample for n values between 0 and 55c/sqcm
c
c
      read(5,*) n
      do 10 j = 1,n,1
      read (5,*) extime(j), exepr(j)
 10   continue
c
c
c     ------------------------------------------------------------
c
c
```

```
c       computation of the root (time - time0) values for each exptal
c       time value.
c
c
        read(5,*) time0
        do 20 j = 1,n,1
         mtime(j) = extime(j) - time0
         erootm(j)= mtime(j) ** 0.5
 20     continue
c
c
c
c       ------------------------------------------------------------
c
c
c       calculation of experimental slope of epr versus root-time data
c
c
        eslope = 0
        econst = 0
        ecorr  = 0
        call regres(n,erootm,exepr,eslope,econst,ecorr)
c
c       ------------------------------------------------------------
c
c        output of experimental epr-root time values
c
         write(15,3000)
         write(15,3001) id,t,strain
         write(15,3002)
         write(15,3003)
         do 31 j = 1,n,1
           write(15,3004) erootm(j),exepr(j)
 31      continue
         write(*,*)
         write(*,*) '     experimental slope is ',eslope
         write(15,3005)
         write(15,3006) eslope
         write(*,*)
c
c
c       ------------------------------------------------------------
c
c
c             theoretical calculation of epr-root time slope
c
c
c       ------------------------------------------------------------
c
c
        write(*,*)
        write(*,*) 'theoretical slope calculations in progress'
        write(*,*)
c
c       ------------------------------------------------------------
c
c
        write(*,*)
        write(*,*) '     depletion volume and width computation'
        write(*,*)
```

```
c
c
c
c       ---------------------------------------------------------------
c
c
c       computation of volume parameter corresponding to epr
c       values of 5 to 50 c/sqcm
c
c
        do 700 i = 0,10
         prepr(i) = i*5
         vp(i) = 0
         check = 0
         call volume (prepr(i),check,vp(i))
  700   continue
c
c
c       ---------------------------------------------------------
c
c
c       specification of minimum chromium level for the sample
c
c
        if(t.eq.575) crmin = 8.07
        if(t.eq.625) crmin = 8.37
        if(t.eq.670) crmin = 8.74
        if(t.eq.725) crmin = 9.38
        if(t.eq.775) crmin = 10.17
c
c
c       ---------------------------------------------------------------
c
c
c       calculation of ratio and inverse error function of ratio
c       for ratio between 0 and 1 only
c
c
c
        ratio = (cratk - crmin)/(crbulk - crmin)
        if(ratio.lt.0.0.or.ratio.gt.1.0) then
          write(10,1500)
          goto 500
        endif
        erfinv = 0
        call erfcal (ratio,erfinv)
c
c
c       ---------------------------------------------------------------
c
c
c       computation of width of depletion profile corresponding
c       to epr values of 5 to 50 c/sqcm
c
c
        do 900 i = 0,10
         wid(i) = (vp(i) * 2 * cratk)/(cratk - crmin)
  900   continue
c
c
```

```
c
c       ---------------------------------------------------------------
c
c
c       specification of diffusivity steps for different temp ranges
c       and minimum diffusivity value to start computation
c
c
        if(t.lt.700) ddiff = 1e-19
        if(t.ge.700) ddiff = 1e-17
c
c
c       ---------------------------------------------------------
c
c
c       calculation of theoretical epr-root time slopes for
c       input diffusivity values
c
        do 50 l =1,10000,1
         diff  = l * ddiff
         do 1000 i = 0,10
          prootm(i) = ((((wid(i)*1e-8)/(erfinv*2))**2)/
     #                (diff*3600))**0.5
 1000     continue
          n  = 11
          call regres(n,prootm,prepr,pslope,pconst,pcorr)
c
c
c       -----------------------------------------------------------
c
c
c       comparison of experimental/theoretical slopes to determine
c                       chromium diffusivity
c
c
c       -----------------------------------------------------------
c
c
          error = abs(pslope - eslope)
          if (error.lt.0.1) then
           crdiff = diff
           tslope = pslope
           tconst = pconst
           tcorr  = pcorr
           write(*,*)
           write(*,*) '     theoretical slope is ',tslope
           write(*,*)
           write(10,2001) t,strain,time0,eslope,crdiff
           goto 250
          endif
 50      continue
c
c
c       ---------------------------------------------------
c
c       output of theoretical computations
c
 250     write(15,3010)
         write(15,3011)
         do 55 j = 1,n,1
```

```
         write(15,3012) prootm(j),prepr(j),vp(j),crmin,
     #                  ratio,erfinv,wid(j)
 55     continue
       write(15,3013)
       write(15,3014) tslope
c
c
c       ------------------------------------------------------
c
c
        write(*,*)
        write(*,*)'     diffusivity value is', crdiff, 'cm2/s'
        write(*,*)
        write(*,*)
c
c       ------------------------------------------------------
c
c
c       continuation of loop for next sample
c
c
  500   continue
c
c
c       ------------------------------------------------------
c
c       formated outputs
c
c
 1500   format(1h ,2x, 'ratio value out of range, check input')
 2000   format(1h ,2x,'tempc',2x,'strain%',2x,'time0hr',2x,
     #         'slopeunits',2x,'diffcm2/sec'/)
 2001   format(1h ,2x,f5.1,2x,f6.2,2x,f7.3,2x,f10.4,2x,e9.2)
 3000   format(1h ,15x,'sample#',5x,'temperaturec',5x,'strain%'//)
 3001   format(1h ,17x,i2,11x,f5.1,9x,f7.2//)
 3002   format(1h ,20x,'experimental computations'/)
 3003   format(1h ,20x,'rootime_/hr',5x,'eprc/sqcm'/)
 3004   format(1h ,20x,f10.3,5x,f9.3)
 3005   format(//1h ,25x,'slope c/cm2/_/hr'/)
 3006   format(1h ,30x,f5.2//)
 3010   format(1h ,20x,'theoretical computations'/)
 3011   format(1h ,5x,'rootime_/hr',2x,'eprc/sqcm',2x,'vpa',2x,
     #         'crmin%',2x,'ratio',2x,'erfinv',2x,'widtha'/)
 3012   format(1h ,2x,f10.3,2x,f9.3,1x,f5.1,2x,f5.2,2x,f5.3,2x,
     #         f6.3,2x,f6.2)
 3013   format(//1h ,25x,'slope c/cm2/_/hr'/)
 3014   format(1h ,30x,f5.2//)
c
c
c       ------------------------------------------------------------------
c
c
c       closure of input and output files
c
c
        close (5)
        close (10)
        close (15)
c
c
```

```
c       ------------------------------------------------------------------
c
c
c       end of main program
c
c
 9999   stop
        end
c
c
c       ------------------------------------------------------------------
```

```
c
c       ------------------------------------------------------
c
c
c
        subroutine regres(n,x,y,slope,const,rcoeff)
        integer n
        real x(50),y(50)
        real meanx,meany,slope,const,rcoeff
        real xtotal,ytotal,xytot,xxtot,sum1,sum2,sum3
        slope  = 0
        const  = 0
        rcoeff = 0
        xtotal = 0
        ytotal = 0
        xytot  = 0
        xxtot =  0
        sum1 =   0
        sum2   = 0
        sum3   = 0
        do 100 i = 1,n
        xtotal = xtotal + x(i)
        ytotal = ytotal + y(i)
        xytot  = xytot + x(i)*y(i)
        xxtot  = xxtot + x(i)**2
  100   continue
        meanx  = xtotal/n
        meany  = ytotal/n
        slope  = (xytot - n*meanx*meany)/(xxtot -n*(meanx**2))
        const  = meany - slope*meanx
c
c
c       all calculations based on the formulas given in text
c       gives us the slope and constant of regression line
c
c
c
c       calculation of regression coefficient
c
c
        do 200 i = 1,n
        sum1   = sum1 + (x(i) - meanx)*(y(i) - meany)
        sum2   = sum2 + (x(i) - meanx)**2
        sum3   = sum3 + (y(i) - meany)**2
  200   continue
        rcoeff = sum1/((sum2*sum3)**0.5)
        return
        end
```

```
c
c       ------------------------------------------------------
c
c
        subroutine volume (epr,check,vp)
c
c
c       initializing terms in volume
c
c
        real vp,check,epr,error
        integer count
        vp = 0
        check = 0
        count = 0
c
c
c        calculation of vp
c
c
        if(epr.lt.0.5) goto 500
  100   if (count.le.250) then
        vp = vp + 1
        check = 1.1*vp - 6.1e-3*vp**2 + 1.3e-5* vp**3
        error = abs (check - epr)
        if(error.gt.1)then
        count = count + 1
        goto 100
        endif
        endif
 500    return
        end
```

```
      subroutine erfcal (ratio,erfinv)
      real ratio, sum(100), denom (100), error
      real erf, erfinv,lsterr
      lsterr = 1.0
      do 50 j = 1,500,1
       sum(0) = j*0.002
       denom(0) = 1.0
       do 100 i = 1,10,1
        a    = 2 ** i
        b    = sum(0) ** (2*i +1)
        denom(i) = (2 * i +1) * denom(i-1)
        sum(i) = sum(i-1) + ((a * b)/denom(i))
100    continue
       erf = (2* exp(-(sum(0)**2))* sum(10))/1.7724
       error = abs(erf - ratio)
       if (error.le.lsterr) then
        lsterr = error
        erfinv = sum(0)
      endif
50    continue
      return
      end
```

TYPICAL INPUT FILE

```
1100    1                          ..... Solution Anneal Conditions
0.058   17.11   11.43   2.26      ..... Composition
1                                  ..... Number of Materials
1       575     0                  ..... Identity, TemperatureC, Strain%
        7                          ..... Number of Data Points
        200     0                  ..... EPR-Time Data (t0 is first point)
        203     .758
        289     2.6
        344     13.62
        375     15.75
        409     27.59
        432     28.3
        200                        ..... t0 value
```

APPENDIX 1B

SOFTWARE FOR STRAIN-THERMODYNAMICS COMPUTATIONS

```
c     ------------------------------------------------------------
c
c     algorithm deltagcalc
c
c
      program deltagcalc
c
c
c     calculates delatg* and deltaggb for the material
c     given input t0, and matrix/grain boundary diffusivity
c
c     ------------------------------------------------------------
c
c     definition of terms used in algorithm
c
      real t0,tn,tdepl,fo1,fo2,fgb1,fgb2,qam,qagb,strain,r,
     #     t, dm,k,wbulk,ratio,crmin,erfinv,cratk,crbulk
        integer i
c
c     ------------------------------------------------------------
c
c     initialization of nucleation time equation constant (k) for
c     data in hrs and gas constant r in cals/mole/degk
c
      k = 5.1e-16
      r = 2.0
c
c     ------------------------------------------------------------
c
c     opening output files
c
      open (10,file = 'deltag.op1')
      write (10,100)
  100 format(1h ,10x,'temp.c',5x,'strain%',5x,'t0hr',5x,'tdeplhr'
     #               5x,'tnhr')
c
c
      open (15,file='deltag.op2')
      write(15,200)
  200 format(1h ,10x,'temp.c',5x,'strain%',5x,'tnhr',5x,'deltag*',
     .       2x,'deltaggb')
      open(20,file='deltag.op3')
      write(20,300)
  300 format(1h ,10x,'tempc',5x,'strain%',5x,'tnhr',5x,'deltag*',
     .      2x,'deltaggb')
c
c     ------------------------------------------------------------
c
c     starting of loop for 25 samples
c
      do 500 i = 1,25,1
c
c     ------------------------------------------------------------
c
c     opening input file and reading input temperature in c (t), zero-
c     time (t0,hr), strain level, activation barrier to matrix (qam) and
c     grain boundary (qagb) diffusion, matrix diffusivity of each strain
c     sample at each t value
c
      open(5,file='deltag.dat')
```

```
      read (5,*) t, strain, t0, qam, qagb, dm
c
c     ---------------------------------------------------------------
c
c     conversion of t (in c) to t1 (in a)
c
      t1 = t + 273
c
c     ---------------------------------------------------------------
c
c     calculation and output of width of depletion at bulk chromium
c     level, given width of depletion at 13.5% level is 25a. requires
c     specification of the chromium minimum value, calculation of
c     erfinverse, and calculation of width.
c
c
c       specification of minimum chromium level for the sample
c
c
        cratk = 13.5
        crbulk=18.0
c
        if(t.eq.575) crmin = 8.07
        if(t.eq.625) crmin = 8.37
        if(t.eq.670) crmin = 8.74
        if(t.eq.725) crmin = 9.38
        if(t.eq.775) crmin = 10.17
c
c
c       calculation of ratio and inverse error function of ratio
c       for ratio between 0 and 1 only
c
c
c
        ratio = (cratk - crmin)/(crbulk - crmin)
        erfinv = 0
        call erfcal (ratio,erfinv)
c
c
c       computation of width of depletion profile at bulk level
c
c
        wbulk = 25 * 1e-8/erfinv
        tdepl = (wbulk**2)/(3600*4*dm)
        tn    = t0 - tdepl
        write(10,101) t, strain, t0, tdepl, tn
 101    format(1h ,10x,f5.1,5x,f6.2,2x,f9.4,2x,e9.2,3x,f9.4)
c
c     ---------------------------------------------------------------
c
c     calculation and output of thermodynamic barrier to nucleation (delg1)
c     and grain boundary energy assuming matrix control (in cals/mole)
c
      fo1 = r*t1*log(tn/(k*exp(qam/(r*t1))))
      call gbecal(t1,fo1,fgb1)
      write (15,201) t,strain,tn,fo1,fgb1
 201  format(1h ,10x,f5.1,5x,f6.2,2x,f9.4,2x,f8.1,2x,f8.1)
c
c
c     ---------------------------------------------------------------
```

```
c
c     calculation and output of thermodynamic barrier to nucleation
c     (delg2) and grain boundary energy (delg3) assuming grain boundary
c     control (in cals/mole)
c
      fo2 = r*t1*log(tn/(k*exp(qagb/(r*t1))))
      call gbecal(t1,fo2,fgb2)
      write (20,401) t,strain,tn,fo2,fgb2
 401  format(1h ,10x,f5.1,5x,f6.2,3x,f9.2,5x,f9.2,2x,f8.1)
 500  continue
c
c
c       ---------------------------------------------------------------
c
c
      close(10)
      close(15)
      close(20)
      close(5)
      stop
      end
```

```
c     ------------------------------------------------------------------
c
      subroutine gbecal(t,fo,fgb)
c
c     ------------------------------------------------------------------
c

      real fa,fb,t,b,c,d,cwl,mo,fhom,fgbtry,fgb
      integer j
        cwl = 0.058
        mo =2.16
        fa = 0.1*t - (110+150*cwl+4*mo)
        fb = 172
        fgb = 0
      fhom = (16*3.14*(fb**3))/(3*(fa**2))
      do 600 j = 1,1720,1
        fgbtry = j*0.2
        b    = (fgbtry/(2*fb))
        c = ((2 - 3*b+ b**3)/2)*fhom
        d = abs(c-fo)
        if (c.ge.0.and.d.le.100) then
         fgb = fgbtry
         goto 625
        endif
 600  continue
 625  return
      end
```

```
      subroutine erfcal (ratio,erfinv)
      real ratio, sum(100), denom (100), error
      real erf, erfinv,lsterr
      lsterr = 1.0
      do 50 j = 1,500,1
       sum(0) = j*0.002
       denom(0) = 1.0
       do 100 i = 1,10,1
        a    = 2 ** i
        b    = sum(0) ** (2*i +1)
        denom(i) = (2 * i +1) * denom(i-1)
        sum(i) = sum(i-1) + ((a * b)/denom(i))
100    continue
       erf = (2* exp(-(sum(0)**2))* sum(10))/1.7724
       error = abs(erf - ratio)
       if (error.le.lsterr) then
        lsterr = error
        erfinv = sum(0)
      endif
50    continue
      return
      end
```

TYPICAL INPUT FILE

575	0	200	76000	62000	2.3E-18
575	2	100	74000	62000	2.1E-18
575	6	60	65000	62000	0.50E-17
575	10	40	64000	62000	0.68E-17
575	16	10	62000	62000	0.99e-17
625	0	15	76000	62000	0.27E-16
625	2	3	74000	62000	0.40E-16
625	6	1.5	65000	62000	0.46e-16
625	10	0.75	64000	62000	0.97e-16
625	16	0.25	62000	62000	0.14e-15
670	0	1.8	76000	62000	0.22e-15
670	2	0.5	74000	62000	0.26e-15
670	6	0.2	65000	62000	0.37e-15
670	10	0.2	64000	62000	0.54e-15
670	16	0.15	62000	62000	0.71e-15
725	0	0.35	76000	62000	0.18e-14
725	2	0.3	74000	62000	0.19e-14
725	6	0.2	65000	62000	0.14e-14
725	10	0.15	64000	62000	0.18e-14
725	16	0.1	62000	62000	0.26e-14
775	0	0.28	76000	62000	0.11e-13
775	2	0.18	74000	62000	0.91e-14
775	6	0.12	65000	62000	0.84e-14
775	10	0.12	64000	62000	0.97e-14
775	16	0.08	62000	62000	0.13e-13

APPENDIX 1C

EQUATIONS USED FOR SSDOS MODEL SUBROUTINES

EQUATIONS FOR STRAIN EFFECTS ON SENSITIZATION MODELING

COMPUTATION OF DIFFUSIVITY WITH STRAIN

Strain effects on diffusivity were calculated by

1) Computing Diffusivity at the specified temperature for 0, 2, 6, 10, 16% strain values

0% Strain ..... D = 50 exp (-76000/RT)
2% Strain ..... D = 20 exp (-74000/RT)
6% Strain ..... D = 0.3 exp (-65000/RT)
10% Strain ..... D = 0.3 exp (-64000/RT)
16% Strain ..... D = 0.1 exp (-62000/RT)

(T is in degrees Kelvin)

2) Linear interpolation for strain levels within above ranges

COMPUTATION OF THERMODYNAMIC EFFECTS OF STRAIN

Strain-induced thermodynamic changes were accounted for by

1) Computing Free Energy change at interface (DELTAGgb) values at different temperatures for 0, 2, 6, 10, 16% strains through two-degree fits to the Ggb - Temperature data

0% Strain ... Ggb = -1112.549622 + 2.677884*T - 0.001291*T**2
2% Strain ... Ggb = -2044693677 + 4.764065*T - 0.002434*T**2
6% Strain ... Ggb = -2329.814062 + 5.423945*T - 0.002801*T**2
10% Strain ... Ggb = -2203.98506 + 5.212603*T - 0.002715*T**2
16% Strain ... Ggb = -768.94905 + 2.280788*T - 0.001218*T**2

(T is in degrees Kelvin)

2) Linear interpolation for strain levels within above ranges

APPENDIX 2A

EPRDOS VALUES FOR STRAINED-SENSITIZED SAMPLES

575C DATA

0%		2%		6%		10%		16%	
t hr	EPRDOS C/cm2	t hr	EPRDOS C/cm2	t hr	EPRDOS C/cm2	t hr	EPRDOS C/cm2	t hr	EPRDOS C/cm2
203	0.7	159	4.2	72	7.4	48	3.4	24	2.6
289	2.6	203	7.8	159	16.7	72	9.3	48	4.5
344	13.6	289	12.1	179	20.6	96	16.1	72	9.2
375	15.7	301	16.5	203	14.8	120	17.0	96	14.4
409	27.6	320	22.3	240	31.2	179	21.5	120	23.9
432	28.3	380	31.0	289	35.5	195	19.4	159	28.6
				321	27.3	203	37.1	179	31.7
				360	42.8	216	40.2	203	40.1
				400	52.3	264	39.7	279	56.6
						292	42.6		
						325	46.5		

625C DATA

0%		2%		6%		10%		16%	
t hr	EPRDOS C/cm2	t hr	EPRDOS C/cm2	t hr	EPRDOS C/cm2	t hr	EPRDOS C/cm2	t hr	EPRDOS C/cm2
6	0.2	0.1	0.0	1	0.0	0.5	0.0	0.1	0.0
9	0.3	2	0.0	2	1.4	1	0.9	0.5	0.9
17	0.8	4	0.7	4	5.5	2	3.7	1	2.8
25	10.2	7	2.7	7	10.1	4	9.3	2	9.3
43	23.5	10	3.4	10	13.1	7	17.1	4	15.3
50	29.2	13	4.5	13	15.6	10	24.3	7	26.9
57	29.4	16	5.7	16	19.5	13	27.8	10	34.2
66	37.5	20	9.4	20	20.4	16	33.9	13	35.4
76	34.9	26	16.0	22.5	24.1	20	39.7	16	44.6
90	41.1	32.5	17.6	26	27.6	22.5	40.3		
100	45.1	40	24.9	32.5	33.4	26	46.8		
		44	29.8	38.5	38.2				
		50	34.7	42.5	44.2				
		57	41.8						
		60	48.6						

670C DATA

0%		2%		6%		10%		16%	
t hr	EPRDOS C/cm2	t hr	EPRDOS C/cm2	t hr	EPRDOS C/cm2	t hr	EPRDOS C/cm2	t hr	EPRDOS C/cm2
1.25	0.5	0.1	0.0	0.1	0.0	0.1	0.0	0.1	0.0
2	0.6	0.3	0.0	0.3	0.9	0.3	0.8	0.3	2.1
4	4.7	0.6	1.9	0.6	6.8	0.6	5.0	0.6	9.3
5	11.6	1	7.8	1	13.3	1	10.5	1	18.1
6	15.6	2	16.9	2	20.5	2	18.0	2	26.4
8	22.2	4	28.1	4	31.8	4	29.1	4	38.6
9	33.3	4.5	27.9	4.5	33.3	4.5	39.7	4.5	41.9
10	35.5	5	32.9	5	34.1	5	41.5	5	49.0
12	34.8	5.5	30.6	5.5	34.1	5.5	45.2	5.5	53.3
14	37.9	6.25	29.1	6.25	36.4				
16	46.0	7	32.6	7	43.8				
18	46.2	8.5	36.7	8	46.0				
		10	46.1						

725C DATA

0%		2%		6%		10%		16%	
t hr	EPRDOS C/cm2	t hr	EPRDOS C/cm2	t hr	EPRDOS C/cm2	t hr	EPRDOS C/cm2	t hr	EPRDOS C/cm2
0.1	0.0	0.2	0.0	0.1	0.0	0.1	0.1	0.1	0.0
0.4	1.2	0.5	6.5	0.2	0.2	0.2	1.3	0.2	2.9
0.5	1.4	0.6	8.7	0.4	8.4	0.4	11.2	0.4	20.7
0.8	3.3	0.8	14.5	0.5	10.8	0.5	14.5	0.5	22.4
1.1	10.8	0.95	16.5	0.6	12.9	0.6	15.4	0.6	23.2
1.4	15.5	1.25	25.0	0.7	16.3	0.7	18.6	0.7	28.2
1.6	19.9	1.4	20.6	0.8	14.9	0.8	19.2	0.8	26.7
1.8	27.9	1.6	22.9	0.95	16.7	0.95	19.7	0.95	28.4
2.0	32.6	1.8	33.1	1.1	17.1	1.1	21.0	1.1	31.0
2.3	47.4	2	36.3	1.25	17.7	1.25	29.9	1.25	34.3
		2.3	46.2	1.4	22.6	1.4	36.0	1.4	42.0
				1.6	32.5				
				1.8	41.1				

775C DATA

0%		2%		6%		10%		16%	
t hr	EPRDOS C/cm2	t hr	EPRDOS C/cm2	t hr	EPRDOS C/cm2	t hr	EPRDOS C/cm2	t hr	EPRDOS C/cm2
0.1	0.0	0.2	0.4	0.1	0.2	0.1	0.1	0.1	2.1
0.3	2.6	0.4	3.7	0.2	2.2	0.2	3.9	0.2	9.7
0.5	16.4	0.5	12.5	0.3	10.0	0.3	13.8	0.3	21.6
0.7	27.6	0.6	19.2	0.4	12.6	0.4	16.9	0.4	26.4
0.8	30.6	0.8	30.3	0.5	18.0	0.5	25.9	0.5	37.4
0.9	37.1	0.9	35.3	0.6	20.8	0.6	28.4	0.6	37.9
1	41.0	1	38.0	0.7	26.4	0.7	30.6	0.7	41.4
1.1	52.1	1.1	44.3	0.8	27.0	0.8	33.5	0.8	44.1
				0.9	30.4	0.9	44.9		
				1	35.9				
				1.1	49.7				

APPENDIX 2B

EPRDOS VALUES FOR ANNEALED-SENSITIZED SAMPLES

MILL PROCESSED MATERIAL DATA

560C

t hr	EPRDOS C/cm2
0.1	0.0
1	0.0
10	0.0
100	0.9

625C

t hr	EPRDOS C/cm2
6	0.3
8	0.3
10	0.6
26	5.7
100	47.1

650C

t hr	EPRDOS C/cm2
2	0.2
6	4.2
10	11.4

670C

t hr	EPRDOS C/cm2
0.1	0.0
1	0.4
2	5.8
4	12.8
6	26.2
8	28.9
10	36.7
100	108.2

720C

t hr	EPRDOS C/cm2
0.5	6.0
1	23.6

780C

t hr	EPRDOS C/cm2
0.1	2.4
1	40.3
10	71.0
25	66.4

800C

t hr	EPRDOS C/cm2
0.1	2.1
0.5	25.8
1	31.2
5	39.8
10	24.7
25	6.9

850C

t hr	EPRDOS C/cm2
0.1	1.1
0.3	5.9
0.5	13.5
1	8.4

SOLUTION ANNEALED MATERIAL DATA

SA1000-1hr		SA1050-0.5hr		SA1050-1hr	
t hr	EPRDOS C/cm2	t hr	EPRDOS C/cm2	t hr	EPRDOS C/cm2
3	0.2	26	27.5	6	2.1
6	2.5			8	6.6
8	5.2			10	3.5
10	4.5			26	29.9
26	18.5				

APPENDIX 3

LEGEND

APPENDIX 3

LEGEND

BCC	Body Centered Cubic
BF	Bright Field
BWR	Boiling Water Reactor
CCS	Continuous Cooling Sensitization
CST	Constant Strain Tensile (specimen)
C-TEM.....	Conventional Transmission Electron Microscopy
DF	Dark Field
DOS	Degree of Sensitization
EDS	Electron-Dispersive X-Ray Spectroscopy
EPR	Electrochemical Potentiokinetic Reactivation (test)
EPRDOS.....	EPR - Degree of Sensitization
GBA	Grain Boundary Area
GBCD	Grain Boundary Chromium Depletion
IG	Intergranular
IGSCC.....	Intergranular Stress Corrosion Cracking
isoDOS.....	Line of Constant Degree of Sensitization Value
MP	Mill Processed
OGI	Oregon Graduate Institute
PNL	Pacific Northwest Laboratory
SA	Solution Anneal
SCE	Saturated Calomel Electrode
SCC	Stress Corrosion Cracking
SFE	Stacking Fault Energy
SS	Stainless Steel
TEM	Transmission Electron Microscopy
STEM	Scanning Transmission Electron Microscopy
TM	Thermomechanical
TTS	Time-Temperature-Sensitization
TTSS	Time-Temperature-Strain-Sensitization
VP	Volume Parameter
VST	Variable Strain Tensile (specimen)

VITA

The author was born in Bombay, India on October 5, 1963. He joined the Department of Metallurgical Engineering, Indian Institute of Technology, Bombay in 1981. On completion of his degree, he was admitted for a doctoral program at the Oregon Graduate Institute in September, 1985.